

RESPONSE OF ONE-WAY REINFORCED MASONRY FLEXURAL WALLS  
UNDER BLAST LOADING

RESPONSE OF ONE-WAY REINFORCED MASONRY FLEXURAL WALLS  
UNDER BLAST LOADING

By:

MARK GEOFFREY CHRISTOPHER HAYMAN  
B.Eng. & Mgmt. (McMaster University)

A Thesis Submitted to the School of Graduate Studies in Partial Fulfilment of the  
Requirements for the Degree of Master of Applied Science

McMaster University  
© Copyright Mark Hayman, 2014

MASTER OF APPLIED SCIENCE (2014)  
McMaster University

(CIVIL ENGINEERING)  
Hamilton, Ontario

Title: Response of Two-Way Reinforced Masonry Infill Walls under Blast  
Loading

Author: Mark Hayman, B.Eng. & Mgmt. (McMaster University)

Advisors: Dr. W.W. El-Dakhkhni  
Dr. M.J. Tait

Number of Pages: xx, 102

## **ABSTRACT**

In this thesis, the dynamic structural response of six scaled flexural masonry walls to scaled blast loading is experimentally investigated. These walls have been tested in at an open range with charge masses ranging from 5 kg to 25 kg of Pentex-D explosive material with a TNT equivalency of 1.2, and with a constant stand-off distance of 5 m throughout testing. The field properties of the blast wave, which includes the reflected and free field pressures, were recorded. Additionally, the displacement response histories of the wall over the blast test were recorded and the post-blast damage was documented. This study puts forth several potential models for the analysis of the experimental data. The experimentally obtained blast characteristics were compared to predictions of the Kingery and Bulmash (K-B) model. The strain rates used during the study are equivalent to those developed by a number of studies for the materials used in the construction of the specimens.

The results obtained through the experimental program are compared to those from a variety of single degree of freedom models, ranging from simplified linear relationships to complex stress-strain relations accounting for the effects that arise because of the increased strain rate due to blast testing. The simplified model assumes a constant stiffness, mass, and triangular pressure profile to determine the peak deflection of the specimen during an experimental test. The bilinear and nonlinear models are based on the discretization of the wall sections into a number of layers, and using strain-rate dependent, stress-strain relations of the constituent materials to generate stresses within the layers. These stresses then

form the basis of the resistance function to determine the structural response of the test specimens. In this study, the effect of higher modes of vibration on the test specimens is not included. The bilinear and nonlinear models are then implemented to develop Pressure-Impulse ( $P-I$ ) diagrams, and the effect of the strain rate on  $P-I$  diagrams is investigated. The  $P-I$  are then available to be implemented into the recent blast code for reinforced masonry flexural walls.

The fitted results of the recorded experimental blast pressure parameters are shown to be adequately approximated by the software ConWep in terms of the peak pressure and specific impulse. Comparing the K-B model, which forms the theoretical basis of ConWep, to the raw pressure profile data obtained from the experimental testing, a significant variations is found in the pressure data while significant scatter is found in the impulse. The analytical results show that increasing the nonlinearity of the material accounts for; the response predicted by the single degree of freedom model more closely relates to the response of the specimens. In addition, strain rate effects have a significant impact on the potential level of protection (LOP) provided by masonry flexural walls, as it has a noticeable effect on the curves of the  $P-I$  diagram.

## **ACKNOWLEDGEMENTS**

I would like to extend my gratitude to Dr. Wael El-Dakhakhni for his support through this endeavor, as well as Dr. Michael Tait and Dr. Waleed Mekky for their efforts during the development of this thesis. Special thanks are additionally due to Dr. Manuel Campidelli for his aid through the analysis phase.

Additional thanks go out to Mr. Rick Guilbeault, Mr. Don Wilson and Mr. Bert von Rosen of the Canadian Explosives Research Laboratory (CERL) for their help during the experimental testing. As well, thanks are extended to the Canadian Armed Forces for providing their test range. Thanks also go out to the technicians at the ADL, Mr. Kent Wheeler and Mr. Paul Heerema for their significant assistance during the experimental phase of this project.

This research was facilitated with funding provided by McMaster University Centre for Effective Design of Structures (CEDS), funded through the Ontario Research and Development Challenge Fund (ORDCF), the Natural Sciences and Engineering Research Council of Canada (NSERC), Collaborative Research and Development Project Grant (CRDPG) program, the Canadian Concrete Masonry Producers Association (CCMPA), and the Canada Masonry Design Centre (CMDC). The provision of mason time by Ontario Masonry Contractors Association (OMCA) is gratefully acknowledged.

I would like to thank the patience of my family, those who have passed in my family during the writing of this study, to my friends who have helped me relieve frustrations either through listening or long nights on Skype, and to Laura. This thesis is dedicated to all of them.

## TABLE OF CONTENTS

Abstract .....	iii
Acknowledgements .....	v
Table of Contents .....	vi
List of Figures .....	xi
List of Tables.....	xv
List of Notations .....	16
CHAPTER 1 - Introduction .....	1
1.1 Background .....	1
1.2 Motivation.....	2
1.3 Objectives of the Research.....	2
1.4 Thesis Organization.....	2
1.5 Literature Review .....	3
1.5.1 Blast Loading .....	3
1.5.2 Pressure Profile .....	4
1.5.3 Blast Wave Modeling .....	5
1.5.4 Scaling Laws .....	6
1.5.5 Atmospheric and Ground Effects.....	6
1.5.6 TNT Equivalency .....	8

1.5.7	Blast Load Predictors.....	8
1.5.8	Structural Response to Blast Loading .....	11
1.5.9	Single Degree of Freedom (SDOF) System.....	13
1.5.10	Pressure-Impulse Diagrams .....	18
1.5.11	Design Approaches.....	20
1.5.12	Flexural Panel Testing .....	21
CHAPTER 2 – Blast Response of One-Way Reinforced Concrete Block Flexural		
	Walls .....	27
2.1	Abstract.....	27
2.2	Introduction.....	28
2.3	Experimental Program.....	29
2.3.1	Materials .....	30
2.3.2	Test setup .....	31
2.3.3	Instrumentation .....	32
2.3.4	Test Matrix.....	32
2.3.5	Crack Patterns .....	33
2.4	Analysis of Test Results .....	35
2.4.1	Pressure Profiles.....	35
2.4.2	Displacement Histories.....	36

2.4.3	Simplified Single Degree of Freedom Model .....	37
2.4.4	Single Degree of Freedom Model Displacement Predictions .....	38
2.4.5	Qualitative and Quantitative Damage States .....	40
2.4.6	Wall Damage State Consequence on Overall Building LOP Classification .....	43
2.5	Conclusions .....	44
CHAPTER 3 - Dynamic Analysis of One-Way Reinforced Concrete Block Flexural Walls .....		
3.1	Abstract .....	55
3.2	Introduction .....	55
3.3	Summary of Experimental Program .....	57
3.3.1	Material Models .....	58
3.4	Load-Deformation Analysis .....	60
3.4.1	Moment-Curvature Analysis .....	60
3.4.2	Force-Displacement Analysis .....	62
3.4.3	Deformed Shape .....	64
3.4.4	Experimental Static Testing .....	65
3.5	Dynamic Analysis .....	65
3.5.1	Single Degree of Freedom Model .....	65

3.5.2	Strain Rate Dependant Constitutive Laws for Materials .....	67
3.5.3	Strain Rate Dependent Resistance Functions .....	68
3.5.4	Theoretical Pressure Profile .....	69
3.5.5	Load-Mass Transformation Factors .....	70
3.5.6	Results from Dynamic Analysis.....	71
3.6	Experimental Data versus Theoretical Predictions .....	72
3.6.1	Blast Wavefront Parameters and Pressure Profiles .....	72
3.6.2	Displacement Histories .....	73
3.7	Pressure-Impulse Diagrams .....	74
3.7.1	Development of Pressure-Impulse Diagrams .....	74
3.7.2	Assessment of damage state.....	75
3.8	Conclusions .....	79
CHAPTER 4 - Summary, Conclusions and Future Work .....		91
4.1	Summary .....	91
4.2	Conclusions .....	92
4.3	Recommendations for Future Work .....	94
CHAPTER 5 - References .....		96
Appendix A: P-I Diagrams developed using the bilinear model and ignoring strain rate effects.....		100

Appendix B: P-I Diagrams developed using the bilinear model and Accounting for strain rate effects .....	101
Appendix C: P-I Diagrams developed using the nonlinear model .....	102

## LIST OF FIGURES

Figure 1.1: Typical pressure profile .....	23
Figure 1.2: Conversion of (a) actual system to (b) equivalent SDOF system .....	23
Figure 1.3: Typical Resistance Function for one-way slab.....	24
Figure 1.4: Qualitative representation of pressure-impulse diagram and the associated response regimes.....	24
Figure 1.5: Typical pressure impulse diagram (CSA, 2012) .....	25
Figure 1.6: Superposition of scaled distance curves on P-I diagrams (Smith and Hetherington, 1995).....	25
Figure 2.1: Wall layout; (a) Elevation; (b) Plans .....	46
Figure 2.2: Experimental test setup; (a) Reaction frame pre-setup; (b) Reaction frame post-setup; (c) DP locations; (d) Interior instrumentation .....	46
Figure 2.3: Observed post-blast damage; (a) Rear face of wall WML6; (b) Loaded face of wall WML6; (c) Rear face of wall WML12; (d) Loaded face of wall WML12; (e) Rear face of wall WML30; (f) Loaded face of wall WML30; (g) Rear face of wall WMH6; (h) Loaded face of wall WMH6; (i) Rear face of wall WMH12; (j) Loaded face of wall WMH12; (k) Rear face of wall WMH30; (l) Loaded face of wall WMH30;.....	47
Figure 2.4: Experimental pressure profiles; (a) wall WML6; (b) wall WML12; (c) wall WML30; (d) wall WMH6; (e) wall WMH12; (f) wall WMH30;.....	48
Figure 2.5: Displacement response at the 8th and 11th courses: (a) wall WML6; (b) wall WML12; (c) wall WMH6; (d) wall WMH12; (e) wall WMH30;.....	49

Figure 2.6: Experimental blast pressure; (a) Ideal pressure profile; (b) Triangular pressure profile .....	50
Figure 2.7: Experimental vs. theoretical deflection histories: (a) wall WML6; (b) wall WML12; (c) wall WMH6; (d) wall WMH12; (e) wall WMH30 .....	51
Figure 2.8: Upper segment wall deflection.....	51
Figure 2.9 Effect of test matrix parameters on experimental damage state: a) Combined; b) Level of Protection provided by Group I ( $\rho = 0.68\%$ ); c) Level of Protection provided by Group II; d) Level of Protection at scaled distance = 2.75 m/kg <sup>1/3</sup> ; e) Level of Protection at scaled distance = 2.18 m/kg <sup>1/3</sup> ; f) Level of Protection at scaled distance = 1.61 m/kg <sup>1/3</sup> ; .....	52
Figure 3.1: Typical evolution of the deformed shape (specimen WML12) .....	81
Figure 3.2: Moment-curvature diagram (Group I wall).....	81
Figure 3.3: Comparison between moment-curvature diagrams associated with different wall groups.....	82
Figure 3.4: Bilinear vs. nonlinear resistance function (Group I walls) .....	82
Figure 3.5: Comparison of resistance functions.....	83
Figure 3.6: Pressure histories experienced by specimen WML12 .....	83
Figure 3.7: Effect of strain rate on bilinear resistance function; (a) bilinear model resistance function; (b) nonlinear model resistance function (specimen WML12) .....	84
Figure 3.8: Comparison between different strain rate dependent resistance functions describing the behaviour of specimen WML12; bilinear model,	

nonlinear model, and SBEDS software (DIFs in SBEDS are assumed from USDOD (2008)) .....	85
Figure 3.9: Variation of the load-mass factor (specimen WML12) .....	85
Figure 3.10: Dynamic reaction history calculated for specimen WML12 .....	86
Figure 3.11: Comparison of displacement histories obtained from test data and four different dynamic models; (a) specimen WML6; (b) specimen WML30 .....	86
Figure 3.12: Pressure-impulse diagrams derived from bilinear model without strain rate effects; (a) specimen WML6; (b) specimen WMH6 .....	87
Figure 3.13: Pressure-impulse diagrams derived from bilinear model including strain rate effects; (a) specimen WML6; (b) specimen WMH6 .....	87
Figure 3.14: Pressure-impulse diagrams derived from nonlinear model including strain rate effects; (a) specimen WML6; (b) specimen WMH6 .....	87
Figure 3.15: Iso-damage curves from bilinear neglecting strain rate (BLNSR), bilinear including strain rate (BL), and nonlinear (NL) models; (a) “Heavy” response limit for specimen WML6; (b) “Blowout” response limit for specimen WMH30 .....	88
Figure A.1: Pressure-impulse diagrams derived from bilinear model neglecting strain rate effects; (a) specimen WML6; (b) specimen WML12; (c) specimen WML30; (d) specimen WMH6; (e) specimen WMH12; (f) specimen WMH30; .....	100
Figure B.1: Pressure-impulse diagrams derived from bilinear model including strain rate effects; (a) specimen WML6; (b) specimen WML12; (c) specimen	

WML30; (d) specimen WMH6; (e) specimen WMH12; (f) specimen WMH30;

..... 101

Figure C.1: Pressure-impulse diagrams derived from nonlinear model; (a)

specimen WML6; (b) specimen WML12; (c) specimen WML30; (d) specimen

WMH6; (e) specimen WMH12; (f) specimen WMH30;..... 102

## LIST OF TABLES

Table 1.1: TNT Equivalent for Common Explosives (Baker et al., 1983; Smith and Hetherington, 1994) .....	26
Table 1.2: Transformation Factors for various loading conditions (Biggs, 1964)	26
Table 2.1: Test Matrix .....	53
Table 2.2: Experimental vs. theoretical blast wave properties.....	54
Table 2.3: Comparison of experimental and theoretical peak deflections.....	54
Table 2.4: Level of protection provided by structural walls .....	54
Table 3.1: Comparison of static test results with theoretical predictions .....	89
Table 3.2: Peak dynamic reaction predicted by different models .....	89
Table 3.3: Comparison of peak pressure and specific impulse obtained from test data and the K–B model.....	89
Table 3.4: Comparison of experimental and theoretical peak displacements.....	90
Table 3.5: Summary of Damage States and Level of Protection provided across selected models.....	90

## LIST OF NOTATIONS

$c$	=	Damping coefficient
$c'_o$	=	Equivalent damping coefficient
$DIF$	=	Dynamic increase factor
$E$	=	Elastic modulus of member
$err$	=	Error (1-Test/Model ratio) in percentage points
$f_c$	=	Dynamic compressive strength of concrete
$f_t$	=	Dynamic tensile strength of concrete
$f_{co}$	=	Basic compressive strength of concrete, equal to 10 MPa
$f_{cs}$	=	Static compressive strength of concrete
$f_{ts}$	=	Static tensile strength of concrete
$f(t)$	=	Load with respect to time
$f(x)$	=	Load distribution across member
$F(t)$	=	Forcing function
$F_t$	=	True forcing function on member
$F'_o$	=	Equivalent forcing function on member
$F_0$	=	Force at initial condition
$F_1$	=	Force at current time
$i_r$	=	Reflective positive phase impulse
$i_s$	=	Positive phase relative impulse
$i_s^-$	=	Negative phase relative impulse

$I(x)$	=	Second moment of inertia of member
$I_{av}$	=	Weighted average moment of inertia
$I_{cr}$	=	Cracked moment of inertia
$I_g$	=	Gross moment of inertia
$IF(t)$	=	Inertia force
$k$	=	Stiffness
$k_t$	=	Actual stiffness of wall
$k'_o$	=	Equivalent spring constant
$K'$	=	Empirical constant for curve of specific damage level
$K_L$	=	Load factor
$K_{LM}$	=	Load-Mass transformation factor
$K_M$	=	Mass factor
$K_R$	=	Resistance factor
$L$	=	Length of the span
$m$	=	Mass per unit length
$m'$	=	Mass of specimen
$m'_o$	=	Equivalent mass
$m_t$	=	True mass of system
$M$	=	Moment resistance
$P(t)$	=	Fitted reflected pressure profile
$P_o$	=	Ambient atmospheric pressure

$P_{\max}$	=	Maximum reflected pressure
$P_r$	=	Positive phase relative impulse
$P_s$	=	Positive “side on” incident overpressure
$P_s^-$	=	Negative “Side on” incident pressure
$R_d$	=	Stand-off distance
$R$	=	Resistance of specimen
$R_0$	=	Resistance at initial condition
$R_{\max}$	=	Maximum resistance value
$R'_o$	=	Equivalent resistance of member
$R_m$	=	True resistance of member
$t$	=	Total elapsed time since arrival time
$T$	=	Natural period of member
$t_a$	=	Arrival time
$t_d$	=	Positive phase duration
$t_d^-$	=	Negative phase duration
$t_o$	=	Time of initiation of blast event
$t_0$	=	Time of initial condition
$V_0(t)$	=	Dynamic reaction
$W_c$	=	Charge mass of explosive material
$W_{TNT}$	=	Equivalent mass of TNT
$x$	=	Distance from one support measured along the span

$X$	=	Any parameter used for the calculation of error
$y_e$	=	Elastic limit of the bilinear resistance function
$Z$	=	Scaled distance
$\alpha_{fy}$	=	Parameter used in the modification of yield strength of steel due to strain rate
$\alpha_{fu}$	=	Parameter used in the modification of ultimate strength of steel due to strain rate
$\alpha_s$	=	Parameter used to increase tensile strength of concrete
$\beta$	=	Parameter used to increase tensile strength of concrete
$\delta$	=	Parameter used to increase compressive strength of concrete
$\Delta(t)$	=	Deflection of member at pre-determined node
$\Delta_0$	=	Displacement at mid span at initial condition
$\dot{\Delta}(t)$	=	Velocity of member at pre-determined node
$\ddot{\Delta}(t)$	=	Acceleration of member at pre-determined node
$\Delta H_c$	=	Heat of combustion of explosive material
$\Delta H_{TNT}$	=	Heat of combustion of TNT
$\dot{\epsilon}_{cc}$	=	Dynamic compressive strain rate in concrete
$\dot{\epsilon}_{cs}$	=	Static compressive strain rate in concrete
$\dot{\epsilon}_r$	=	Dynamic tensile strain rate in reinforcing steel
$\dot{\epsilon}_{tc}$	=	Dynamic tensile strain rate in concrete
$\dot{\epsilon}_{ts}$	=	Static tensile strain rate in concrete
$\phi(x)$	=	Assumed deformed shape

$\gamma$	=	Parameter used to increase compressive strength of concrete
$\lambda$	=	Shape function for blast wave parameter
$\varphi$	=	Deformed shape of member
$\gamma$	=	Blast pressure decay coefficient
$\kappa$	=	Member curvature
$\mu_{\phi}$	=	Curvature ductility ratio
$\mu_{\Delta}$	=	Displacement ductility ratio
$\omega$	=	Circular frequency of member
$\sigma_y$	=	Static yield stress of steel

## CHAPTER 1 - INTRODUCTION

### 1.1 BACKGROUND

In recent years a greater emphasis has been placed on the necessity of structural members to resist blast loading. This has become prevalent due to notable disasters such as the Oklahoma City bombing (1995), the London bombing (2005), and the bombing in Oslo, Norway (2011). The potential for terrorist attacks or accidental blast loading warrants further investigation into explosive events and the response of structural members under such loads. Recently constructed masonry structures may be unsafe if involved in explosive events while designed in accordance with current code provisions and practices. For instance, the standard CSA S304.1-04 (CSA, 2004) for the design of masonry structures, in its current form, does not explicitly provide design requirements for masonry structures to resist blast loading.

Blast loading generates significant strain rates several magnitudes higher than those typically present in static loading. The effect of these strain rates on reinforced masonry is characterized by an increase of the yield strength of the assemblage while not affecting its elastic modulus. Because of the composite nature of reinforced concrete block masonry assemblages (i.e. concrete blocks bedded with mortar and cells filled with grout and reinforcement), understanding the behaviour and interaction between these materials under these high strain rates is of primary concern. In addition, the response of the masonry assemblage may change based on the characteristics of the blast load, such as peak pressure, positive phase duration, and specific impulse. Each of the foregoing blast load parameters also have an influence on overall strain rate effects and masonry assemblage response.

## 1.2 MOTIVATION

The complexity of blast loading provides several different variables, which all must be accounted for simultaneously. The coupling of this type of dynamic loading with masonry further complicates matters when modeling both the linear and non-linear response of a structural member. The need to validate analytical models for masonry under blast loading requires experimental data, and although models are readily available, the data from which the models are defined is not in abundance. The experimental data from the blast tests described in Chapter 2 will help further the knowledge base for masonry structures under blast loading.

## 1.3 OBJECTIVES OF THE RESEARCH

There are three objectives, which this research is meant to fulfill:

- a) Experimentally investigate the behavior of masonry flexural walls subjected to blast pressure from live explosive charges detonated on the ground surface.
- b) Analytically develop single degree of freedom models based on the experimental data to aid designers in quantifying potential damage due to blast loads. These models are to include strain-rate effects and the nonlinear response of the masonry assemblage.
- c) Develop pressure-impulse diagrams to aid the assessment of the level of protection provided by masonry walls detailed for out-of-plane blast loading.

## 1.4 THESIS ORGANIZATION

This thesis presents an account of the experimental and analytical results collected for six reinforced masonry walls under a range of blast loads.. Additionally, details concerning the development of dynamic models are discussed.

- Chapter one includes the background, motivation, objectives, as well as the review of the pertinent literature.
- Chapter two contains the information on the field testing, including the experimental data, test setup, test matrix, and the instrumentation.
- Chapter three describes the adopted single degree of freedom models, both linear and non-linear, in addition to the generated pressure-impulse diagrams.
- Chapter four contains a summary of the data, conclusions, and considerations for future research.

## 1.5 LITERATURE REVIEW

### 1.5.1 *BLAST LOADING*

Blast loading occurs when there is a chemical reaction or nuclear reaction causing a rapid release of energy, creating an extreme temperature gradient and wave of pressure (Baker et al., 1983). When the reaction rate of a substance propagating through the explosive material is lower than the speed of sound inside (sub-sonic), the explosion is termed deflagration as no shock wave is formed. Conversely, if the reaction rate greater than the speed of sound (super-sonic), the explosion is known as a detonation (CSA, 2012) as a shock wave is formed.

During a detonation, approximately one third of the chemical energy created by the combustion reaction is released almost instantaneously (USDOD, 2008), while the additional two thirds of the energy generated by the combustion reaction is released over a much longer interval as the detonation material mixes with the surrounding medium (e.g. air). This secondary process, known as afterburning, does not significantly affect the response of structural members (USDOD, 2008).

Explosions can be either accidental or deliberate; Both accidental and deliberate detonations can cause significant damage to structures as well as loss of human life and have recently been addressed in the recent standard CSA S850-12 (CSA, 2012).

### 1.5.2 PRESSURE PROFILE

A typical pressure time profile (pressure history) is shown in Figure 1.1. Generally, a blast wave can be described by the following stages: first a blast wave is generated at time zero ( $t_o$ , in seconds,  $s$ ) and it travels from its source to the target over a period of time described as its arrival time ( $t_a$ , in seconds,  $s$ ); at the time  $t_a$ , the target experiences a net increase in pressure from the ambient value  $P_o$  (in MPa) to the peak “side-on” overpressure ( $P_s^+$ , in MPa). Afterwards, the wavefront pressure decays to  $P_o$  during a time period defined as  $t_d$  followed by further decay to the peak negative peak pressure,  $P_s^-$ , and subsequent return to the ambient pressure after a time  $t_d^-$ , (Baker, 1973). The time between the arrival time and the return to the ambient pressure is known as the *positive phase duration*, since the pressure remains above the ambient pressure. Similarly, from the period between the end of the positive phase and the return to ambient conditions is referred to as the *negative phase duration*, since the pressure is below the atmospheric pressure. Typically, the positive phase duration is much shorter than the negative phase duration, and the peak “side on” pressure is much larger than the peak negative “side on” pressure generated by the explosive event (Baker, 1973). Finally, the specific impulse of the blast,  $i_s$ , (in MPa-s) can be determined for both the positive phase (Eq.(1.1)) and for the negative phase (Eq.(1.2)) of the blast event (Baker, 1973).

$$i_s = \int_{t_a}^{t_a+t_d} P(t) dt \quad (1.1)$$

$$i_s^- = \int_{t_a+t_d}^{t_a+t_d+t_d^-} P(t)dt \quad (1.2)$$

Typically the negative phase is neglected in analysis due to the relatively low pressures and the minimal damage likely to occur as a result of it.

A target positioned at an angle along the path of the shock front through space, does not experience the incident (“side on”) pressure, but rather the reflected (“face on”) pressure,  $P_r$  (in MPa). This causes a reflection of the pressure wave back towards its source. The parameters describing the reflected wavefront, such as the peak pressure and specific impulse, are of the utmost interest for structural designers because they determine the load experienced by the target structure

### 1.5.3 BLAST WAVE MODELING

Baker et al. (1983) proposed a simple linearly decaying relation, given in Eq.(1.3), to describe the experimental pressure profile in terms of the ideal blast wave recalled in Section 1.5.2.

$$P(t) = P_{max} \left( 1 - \frac{t}{t_d} \right) \quad (1.3)$$

where:  $t$  (s) is the elapsed time since the time of arrival of the shock wave,  $t_d$  (s) is the positive phase duration and  $P_{max}$  is the peak reflected overpressure (MPa).

Later, Baker et al. (1983) further refined the pressure-time equation to provide a more accurate representation of the experimental results by defining the modified Friedlander equation, as given in Eq.(1.4).

$$P(t) = P_{max} \left( 1 - \frac{t}{t_d} \right) e^{\left( -\lambda \frac{t}{t_d} \right)} \quad (1.4)$$

The dimensionless parameter  $\lambda$  is called waveform or decay coefficient and determines the shape of the pressure profile.

#### **1.5.4 SCALING LAWS**

The Hopkinson-Cranz scaling method, also known as “cube root” scaling (Smith and Hetherington, 1994), is the predominant form of blast scaling found in the literature reviewed by the author. This law relates different explosions to one another by introducing the so-called scaled distance  $Z$  ( $\text{m/kg}^{1/3}$ ), which is based on the observation that different charge masses,  $W_{TNT}$ , detonated at different standoff distances  $R_d$  from the loaded face of the member, yield the same pressure waves when they stand in relation to one another so as to produce the same  $Z$ , as defined in Eq. (1.5) (Smith and Hetherington, 1994).

$$Z = \frac{R_d}{W_{TNT}^{1/3}} \quad (1.5)$$

#### **1.5.5 ATMOSPHERIC AND GROUND EFFECTS**

An ideal blast wave from surface burst is assumed to occur in standard atmospheric conditions with no variation in time or space and to be unaffected irregularities of the terrain that may generate additional reflections of the shock front (Baker et al., 1983). For design purposes, these assumptions are typically justified.

##### **1.5.5.1 ATMOSPHERIC EFFECTS**

There are several atmospheric conditions which may cause deviations from the ideal pressure profile shown in Figure 1.1. Deviations from the initial ambient pressure and temperature have the potential to change the properties of the shock front depending on the

elevation above sea level of the pressure profiles measured. In addition, changes in the relative humidity and other weather conditions, including fog and rain, can also have an effect on the parameters describing a blast wave (Baker et al., 1983).

For atmospheric conditions to significantly affect the blast wave parameters, they must be relatively extreme. For instance, a strong downward wind can force the shock front back towards the source of the blast, while a significant temperature gradient over a short distance in the atmosphere can cause a layer of warm air on top of a layer of cold air, allowing for the refraction of the shock wave front (Baker et al., 1983).

#### 1.5.5.2 GROUND EFFECTS

An ideal explosion is based on the assumption of an infinitely rigid and smooth ground which would reflect the explosive energy in its entirety; however, in a typical explosive event, the ground dissipates some significant fraction of the energy released by the blast wave (Baker et al., 1983). This dissipation occurs during the formation of a crater following the blast event and involves partial wave reflection as the shock front expands from the source of the blast (Baker et al., 1983). For irregular ground properties, significant variations in the shock front properties can occur: if the ground surface is generally sloped upwards, the blast wave is strengthened as it becomes more focused while proceeding up the slope. If a significant slope is present or if the angle of reflection is less than a specific value, depending on the peak incident pressure, a *Mach wave* can form (Smith and Hetherington, 1994). A *Mach wave* occurs when the incident pressure wave does not fully reflect off the reflecting surface; instead, it skims off the surface, thereby causing the reflected pressure wave to catch up to the incident wave and form a third wave, called the *Mach stem*. This process significantly increases the pressure at wavefront (Smith and Hetherington, 1994). Conversely, in the case of downward slopes, the blast wave is forced to

cover more area, which causes a decrease in the overpressure due to over-expansion of the shock wave.

### **1.5.6 TNT EQUIVALENCY**

With a wide range of explosive materials available, a universal metric must be established in order to properly compare and predict the peak side-on overpressures and scaled distances associated with the material used. In order to do so, the total weight of explosives is converted into an equivalent mass of trinitrotoluene (TNT) required to generate a blast wave causing an equivalent release of energy (Baker et al., 1983). For chemical detonations, the TNT equivalence is determined by calculating the total heat of combustion from the charge weight,  $W_c$ , and solving for the amount of TNT required for producing the same heat. The equation relating the total heat of combustion of the explosive material to the mass of TNT ( $W_{TNT}$ , in kg) required to generate an equivalent amount is given in Eq.(1.6) (Henrych, 1979).

$$W_{TNT} = \frac{\Delta H_c \times W_c}{\Delta H_{TNT}} \quad (1.6)$$

where  $\Delta H_c$  is the heat of combustion for the chemical explosive reactant in J/kg and  $\Delta H_{TNT}$  is the heat of combustion for TNT in J/kg. Typical values for the conversion of a charge weight to an equivalent TNT charge weight are reported in Table 1.1.

### **1.5.7 BLAST LOAD PREDICTORS**

Empirical relationships have been generated in an attempt to estimate the shock front properties, which are presented in the form of charts or equations. Typically, the scaled distance is used to calculate blast wavefront parameters such as the peak reflected and side-on overpressure, reflected and side-on impulse, and the positive phase duration (Baker et al., 1983).

A closed formed solution has been provided to determine the side-on overpressure, in term of the scaled distance  $Z$  in  $\text{m/kg}^{1/3}$ , as shown in Eq.(1.7) (Kinney and Graham, 1985).

$$\frac{P_s}{P_o} = \frac{808[1 + \left(\frac{Z}{4.5}\right)^2]}{\sqrt{1 + \left(\frac{Z}{0.048}\right)^2} \sqrt{1 + \left(\frac{Z}{0.32}\right)^2} \sqrt{1 + \left(\frac{Z}{1.35}\right)^2}} \quad (1.7)$$

As previously noted,  $P_o$  is the atmospheric conditions in kPa at the time of the blast event and  $P_s$  is the peak “side-on” pressure (or incident overpressure) in kPa. A simpler formulation for the peak side-on overpressure (in bar) is given in Smith and Hetherington (1994),

$$P_s = \frac{0.662}{Z} + \frac{4.05}{Z^2} + \frac{3.288}{Z^3} \quad (1.8)$$

Upon determining the side-on overpressure from Eq.(1.7), the peak reflected pressure can then be determined empirically by using Eq.(1.9) (Kinney and Graham, 1985)

$$P_{\max} = 0.20P_s \left( \frac{7P_o + 4P_s}{7P_o + P_s} \right) \quad (1.9)$$

For this equation,  $P_{\max}$  is the peak reflected pressure during a blast event in kPa.

The positive phase duration can be determined via similar empirical formulation such as that given in Eq.(1.10) (Kinney and Graham, 1985)

$$\frac{t_d}{W} = \frac{980[1 + \left(\frac{Z}{0.54}\right)^{10}]}{\sqrt{1 + \left(\frac{Z}{0.02}\right)^3} \sqrt{1 + \left(\frac{Z}{0.74}\right)^6} \sqrt{1 + \left(\frac{Z}{6.9}\right)^2}} \quad (1.10)$$

where  $t_d$  is the duration of the positive phase in milliseconds (ms), and  $W$  is the charge mass, in kg.

After obtaining the positive phase duration, peak reflected pressure and peak side-on overpressure, the reflected impulse can be determined from Eq. (1.11) (Baker et al., 1983)

$$\frac{i_r}{i_s} = \frac{P_{\max}}{P_s} \quad (1.11)$$

where  $i_r$  is the reflected positive impulse and  $i_s$  is the side-on positive impulse, both in kPa-ms. For design purposes, the positive phase duration is often approximated by assuming a linearly decaying profile (Baker et al., 1983) and calculated by inverting Eq.(1.12).

$$i_r = \frac{1}{2} P_{\max} t_d \quad (1.12)$$

Kingery and Bulmash (1984) developed a widely accepted model for the blast wavefront parameters based on the charge mass of equivalent TNT as well as standoff distance. The Kingery and Bulmash (K-B) model uses a number of curve fitting techniques on a large compilation of data, ranging from charge masses of 1 kg to over 400,000 kg, to represent the blast parameters with high degree polynomials and logarithmic relationships. This model is used as the basis of the computer software ConWep (Hyde, 1993).

Lastly, computer software such as A.T.-Blast (Applied Research Associates, 2007) and ConWep (Hyde, 1993) has become available as a means to generate shock front parameters. Although more complex methods have been developed to further refine the analysis for determining blast load variables, due to the simplicity of the geometry of the test setup selected for the research program described in Section 2.3, such methods are not warranted for the purposes of the current investigation. In Section 2.4.1, the blast load parameters derived from the experimental tests are compared to the values generated from the K-B model as well as those generated from the modified Friedlander fit described in Section 1.5.3.

## 1.5.8 STRUCTURAL RESPONSE TO BLAST LOADING

### 1.5.8.1 STRAIN RATE EFFECT

A structural member exposed to a blast load is subjected to rapid loading and thus the effect of strain rate on the overall response of the member becomes increasingly important. This effect alters the mechanical properties, such as the peak stress of the materials subjected to the blast event and potentially the mechanism by which the structural member fails (USDOD, 2008), such as a transition from a flexural failure to a brittle shear failure, as investigated by Takeda and Tachikawa (1971) and Bertero et al. (1973). This effect can potentially lead to a more hazardous failure and provide a lower level of protection for the occupants (Jones, 1988).

From the data reported by Malvar (1998), it can be noted that the peak strain rate found in steel reinforcing bars subjected to blast loading is approximately  $10^2 \text{ s}^{-1}$ , which is several orders of magnitude greater than the strain rate typically found in steel during quasi-static loading, which is within the range of  $10^{-6} \text{ s}^{-1}$  to  $10^{-5} \text{ s}^{-1}$ . To capture the significant increase in steel strength induced by the rate of strain, the dynamic increase factor *DIF* is introduced. The *DIF* is a dimensionless ratio that is used to describe material properties of the constituent material experiencing high strain rate. For the steel reinforcement, the *DIF* can be calculated from Eq.(1.13) (Malvar, 1998)

$$DIF = \left( \frac{\dot{\epsilon}_r}{10^{-4}} \right)^\alpha \quad (1.13)$$

where  $\dot{\epsilon}_r$  is the strain rate of the steel reinforcement in  $\text{s}^{-1}$ , and  $\alpha$  is a dimensionless parameter dependant on the parameter being increased. The value for  $\alpha$  associated with the yield strength of steel is defined in Eq.(1.14), while for the steel ultimate strength  $\alpha$  is defined in Eq.(1.15) (Malvar, 1998).

$$\alpha_{fy} = 0.074 - 0.040 \frac{\sigma_y}{414} \quad (1.14)$$

$$\alpha_{fu} = 0.019 - 0.009 \frac{\sigma_y}{414} \quad (1.15)$$

where  $\sigma_y$  is the yield stress of the steel reinforcing bars, in MPa.

A number of studies have been performed on concrete subjected to peak strain rates as high as  $300 \text{ s}^{-1}$  (USDOD, 2008; Malvar and Ross, 1998). During an explosion, concrete is subject to both tensile and compressive strains and strain rates, and as such *DIFs* must be developed for both conditions to account for the change in material properties. For concrete undergoing to tensile strains rates, Malvar and Ross (1998) proposed the formulation in Eq.(1.16)

$$\frac{f_t}{f_{ts}} = DIF = \begin{cases} \left( \frac{\dot{\epsilon}_{tc}}{\dot{\epsilon}_{ts}} \right)^\delta & \text{for } \dot{\epsilon}_{tc} \leq \dot{\epsilon} \leq 1 \text{ s}^{-1} \\ \beta \left( \frac{\dot{\epsilon}_{tc}}{\dot{\epsilon}_{ts}} \right)^{\frac{1}{3}} & \text{for } \dot{\epsilon}_{tc} > 1 \text{ s}^{-1} \end{cases} \quad (1.16)$$

wherein  $f_t$  is the dynamic tensile strength of the concrete, in MPa;  $f_{ts}$  is the static tensile strength of the concrete, in MPa;  $\dot{\epsilon}_{tc}$  is the tensile strain rate in the concrete due to the dynamic load;  $\dot{\epsilon}_{ts}$  is the static tensile strain rate of concrete, equal to  $10^{-6} \text{ s}^{-1}$ . The values for  $\delta$  and  $\beta$  are defined in Eqs.(1.17) and (1.18) respectively (Malvar and Ross, 1998)

$$\delta = \frac{1}{(1 + 8 f_{cs} / f_{co})} \quad (1.17)$$

$$\log \beta = 6\delta - 2 \quad (1.18)$$

where  $f_{cs}$  is the static compressive strength of the concrete in MPa, and  $f_{co}$  is equal to 10 MPa.

For concrete subjected to compressive strain rates, the compressive strength dynamic increase factor by Malvar and Crawford (1998) is given in Eq.(1.19)

$$f_c / f_{cs} = DIF = \begin{cases} \left( \frac{\dot{\epsilon}_{cc}}{\dot{\epsilon}_{cs}} \right)^{1.026\alpha_s} & \text{for } \dot{\epsilon}_{cc} \leq 30s^{-1} \\ \gamma_s \left( \frac{\dot{\epsilon}_{cc}}{\dot{\epsilon}_{cs}} \right)^{\frac{1}{3}} & \text{for } \dot{\epsilon}_{cc} > 30s^{-1} \end{cases} \quad (1.19)$$

wherein  $f_c$  is the dynamic compressive strength of the concrete in MPa, and  $f_{cs}$  is the static compressive strength of the concrete;  $\dot{\epsilon}_{cc}$  is the compressive strain rate of the concrete due to the dynamic load;  $\dot{\epsilon}_{cs}$  is the static compressive strain rate of concrete, which is equal to  $30 \times 10^{-6} s^{-1}$ ;  $\alpha_s$  and  $\gamma$  are dimensionless parameters defined in Eqs.(1.20) and (1.21), respectively, by Malvar and Crawford (1998).

$$\alpha_s = \frac{1}{5 + 9 f_{cs} / f_{co}} \quad (1.20)$$

$$\log \gamma = 6.156\alpha_s - 2 \quad (1.21)$$

### 1.5.9 SINGLE DEGREE OF FREEDOM (SDOF) SYSTEM

A number of single degree of freedom (SDOF) and multiple degree of freedom (MDOF) models have been developed over the years for analyzing structures subjected to dynamic loading. The aspect common to most of these models is the use of a finite number of lumped masses connected by springs to model the mechanics of actual structural members (Biggs, 1964). The simpler form of these systems is a SDOF model, which utilizes a single lumped mass, a dashpot, and a spring. To obtain the SDOF model, the entire mass of the actual system is assumed to be located at a node which gives a meaningful representation of the overall structural response in terms of displacement, velocity, and acceleration. This technique requires the

calculation of the mass, stiffness and damping coefficient of the equivalent SDOF system by applying to the original member transformation factors, which depend on the selected deformed shape, on the basis of the expected mode of failure. Upon applying these transformation factors, the displacement of the SDOF model is determined. An example of this methodology is depicted in Figure 1.2, where a simply supported beam with uniformly distributed mass per unit length,  $m$ , length  $L$ , and load  $f(t)$ , is transformed in a mass-spring-dashpot SDOF system with a lumped mass equal to  $K_M mL$ , spring constant of  $K_L k_t$ , dashpot with damping coefficient  $c_t$ , and applied loading  $K_L f(t)$ .

The quantities that define any SDOF system include its equivalent mass, stiffness, force, and transformation factors, which are obtained from the assumed deformed shape of the actual structure. These quantities are evaluated by equating the energy of the SDOF model and actual member as the latter deforms. To calculate the equivalent mass,  $m'_o$ , of the SDOF model the total kinetic energy is equated (Biggs, 1964):

$$m'_o = \int_0^L m \phi^2(x) dx \quad (1.22)$$

where  $\phi(x)$  is the assumed deformed shape (natural mode shape) of the structural member based on the boundary and loading conditions, and  $m$  is the linear mass density of the specimen in  $\text{kg/m}^2$ . With increased deformation, the assumed deformed shape of the member changes, transitioning from a shape associated with an elastic section (wherein the onset of permanent deformation has not occurred) to that associated with a plastic section (wherein permanent deformation has occurred).

To calculate the equivalent stiffness,  $k'_o$ , the total strain energy is equated. The equation for the equivalent stiffness of a simply supported structural member is presented by Eq.(1.23) (Biggs, 1964)

$$k'_o = \int_0^L EI(x)\phi^2(x)dx \quad (1.23)$$

where  $E$  is the elastic modulus of the structural member (MPa),  $I(x)$  is the moment of inertia ( $m^4$ ).

Finally, the equivalent force is calculated by equating the external work done by the load. Equation (1.24) provides the equivalent force,  $F'_o$ , given a uniformly distributed load across a simply supported system

$$F'_o = \int_0^L p(x)\phi(x)dx \quad (1.24)$$

where  $p(x)$  represents the actual load distribution along the member span.

These values are then used in the dynamic equation for a SDOF system, as shown in Eq.(1.25) (Biggs, 1964)

$$m'_o \ddot{\Delta}(t) + c'_o \dot{\Delta}(t) + k'_o \Delta(t) = F'_o \quad (1.25)$$

where  $\ddot{\Delta}(t)$ ,  $\dot{\Delta}(t)$ , and  $\Delta(t)$  are, respectively, the acceleration, velocity and displacement of the SDOF model. Owing to the speed at which loading occurs during blast testing, the peak deflection is reached in the first vibration cycle, and therefore the damping term,  $c'_o \dot{\Delta}(t)$ , is neglected because it does not significantly alter the peak deflection (Biggs, 1964). The resulting dynamic equation can thus be simplified from Eq.(1.25) to become Eq.(1.26).

$$m'_o \ddot{\Delta}(t) + k'_o \Delta(t) = F'_o \quad (1.26)$$

To further simplify the dynamic equation of motion, the values of  $m'_o$ ,  $k'_o$ , and  $F'_o$  are replaced with the true values of the corresponding parameters by using the  $K_M$ ,  $K_L$ ,  $K_R$ , and  $K_{LM}$  factors. These factors represent the mass factor, load factor, resistance factor, and the load-mass factor (Biggs, 1964).

The Mass Factor,  $K_M$ , can be determined as the ratio between equivalent lumped mass ( $m'_o$ ), described previously in Eq.(1.22), to the true mass of the system ( $m_t$ ), which is related to the mass density of member ( $m$ ) and its length ( $L$ ) as given in Eq.(1.27) (Biggs, 1964).

$$K_M = \frac{m'_o}{m_t} = \frac{\int_0^L m\phi^2(x) dx}{mL} \quad (1.27)$$

The Load Factor,  $K_L$ , is calculated by determining the ratio between the equivalent load ( $F'_o$ ), defined in Eq.(1.24) (Biggs, 1964), and the true force ( $F_t$ ) in Eq.(1.28) where  $f(x)$  represents the distributed load on the member.

$$K_L = \frac{F'_o}{F_t} = \frac{\int_0^L f(x)\phi(x) dx}{\int_0^L f(x) dx} \quad (1.28)$$

The resistance factor,  $K_R$ , is equal to the load factor (Mays and Smith, 1995) and is taken as the ratio between the equivalent resistance,  $R'_o$  and the actual resistance  $R_m$ , defined in Eq.(1.29) (Biggs, 1964)

$$K_R = \frac{R'_o}{R_m} = \frac{k'_o}{k_t} = K_L \quad (1.29)$$

where the resistance of the structural member is the maximum load that it can be carry it.

By applying the transformation factors in Eqs.(1.27) and (1.28) to Eq.(1.26), the equation of motion can be recast as

$$K_M m_i \ddot{\Delta}(t) + K_L k \Delta(t) = K_L F_i \quad (1.30)$$

to further simplify the equation of motion, the Load-Mass Factor,  $K_{LM}$ , is used, which is simply the ratio between the mass factor and the load factor, given by Eq.(1.31).

$$K_{LM} = \frac{K_M}{K_L} \quad (1.31)$$

Typical load-mass factors given different support conditions and loading configurations are presented in Table 1.2 (Biggs, 1964). Using the value calculated in Eq.(1.31), the equation of motion can be re-written as:

$$K_{LM} m_i \ddot{\Delta}(t) + k_i \Delta(t) = F_i \quad (1.32)$$

Furthermore, the natural period,  $T$  in seconds, of the structure is given in Eq.(1.33) by using the load-mass transformation factor defined in Eq.(1.31) :

$$T = 2\pi \sqrt{\frac{K_{LM} m_i}{k_i}} \quad (1.33)$$

#### 1.5.9.1 RESISTANCE FUNCTION OF STRUCTURAL MEMBERS

A resistance function, or force-deflection relation, compares the total load under static conditions which can be safely opposed by the structural member and the corresponding displacement at a pre-defined point of interest of the member (Smith and Hetherington, 1994). The refinement of the resistance function is necessary to include the effects of the strain rate, mentioned in Section 1.5.8.1 (Smith and Hetherington, 1994).

A typical bilinear resistance function is found in

Figure 1.3 (Smith and Hetherington, 1994). This resistance function shows the typical behavior of a composite structural member, such as a reinforced concrete wall. The member initially acts in an elastic manner, with the resistance provided by the wall increasing as

deflection increases, until a knee point is reached. Following this point, the member acts in a plastic manner, providing a constant resistance as the deflection is increased.

#### **1.5.10 PRESSURE-IMPULSE DIAGRAMS**

A pressure-impulse ( $P-I$ ) diagram (or iso-damage curve) is a tool used by designers to make a preliminary assessment about the combinations of peak pressure and specific impulse which are expected to cause a pre-established level of damage, in accordance with the selected failure criterion. These diagrams were initially developed to help assess and quantify the level of damage that would occur to residential houses during the Second World War due the bombing of cities in the United Kingdom (Mays and Smith, 1995). Early  $P-I$  diagrams were quite elementary because they only rated damage in broad categories, without a precise quantification of the damage: complete destruction, severe damage and minor damage. Since then,  $P-I$  diagrams have been developed to help determine the potential human hazard due to a blast event, providing refined limits for the damage incurred by a structural member or system based on the response of the type of member or system being analyzed for blast loading (Baker et al., 1983; Smith and Hetherington, 1994; USDOD, 2008; CSA, 2011).

The loading regimes associated with  $P-I$  diagrams are depicted in

Figure 1.4 the function plotted in the graph features two asymptotes, referred to as the pressure and impulsive asymptotes. These asymptotes define the minimum pressure or impulse that is required to generate a certain level of damage for a structural member. The vertical dashed line represents the impulsive asymptote, wherein the impulse is the governing value and the peak pressure that the wall is subjected to does not significantly change the response of the member. The horizontal dashed line represents the pressure asymptote, wherein the peak pressure that the wall is subjected to dominates the response of the structural member, while the total specific

impulse of the blast event causes negligible change in the overall structural response (Smith and Hetherington, 1994). Structures subjected to loading with a very short duration compared to their natural period are said to be subject to impulsive loading or to respond in the impulsive regime, as they are very sensitive to the positive phase impulse of the blast (impulse driven). Conversely, when a structural member is subjected to a load of very long duration compared to its fundamental period of vibration, such member is said to experience quasi-static loading, or to respond in the quasi-static regime (pressure driven). For quasi-static loading, the peak pressure is the determining factor for the response, while the specific impulse does not have significant effect (Smith and Hetherington, 1994). For ratios of the positive phase duration to the fundamental period between the impulsive and the quasi-static loading regimes, the structural response is dictated by both the peak pressure and the impulse. This region of the  $P-I$  diagram is known as the dynamic regime (Smith and Hetherington, 1994).

A typical set of  $P-I$  diagrams is presented in Figure 1.5, in which each curve is associated with a different response limit.  $P-I$  combinations which lie to the left of and below a curve represent values which the structural system can safely withstand. Combinations which lie to the right of and above a curve represent combinations which will cause damage in excess of the value associated with said curve and thus failure. This procedure is suitable for an expedient quantification of the structural response of a member based on its loading history and response regime, be it is impulsive (impulse-controlled), dynamic, or quasi-static (pressure-controlled). These curves can be calculated to represent the pressure-impulse combinations associated with the levels of protection specified in CSA S850-12 and ASCE 59-11, as shown for primary structural elements (CSA, 2012; ASCE, 2011).

By superimposing a  $P-I$  diagram and a diagram which determines blast parameters with respect to stand-off distance, a preliminary description of the damage level can be obtained through the development of an empirical equation. An example of one of these empirical equations, from Smith and Hetherington (1994), is presented in Eq.(1.34).

$$R_d = \frac{K'W^{1/3}}{\left[1 + \left(\frac{3175}{W}\right)^2\right]^{1/6}} \quad (1.34)$$

where  $K'$  is an empirical constant developed by calculating the radius of the curve of a specific damage level in the  $P-I$  diagram. These equations allow for a simplified method to assess the level of damage obtained by structural elements based on the blast threat posed. Depicted in Figure 1.6 is a  $P-I$  diagram overlaid on a charge mass-stand-off distance diagram from World War 2. By overlaying the  $P-I$  diagram on this graph, damage based on the weapon type and distance from the epicenter of the blast is easily predicted.

### 1.5.11 DESIGN APPROACHES

The model presented in Biggs (1964) for the SDOF modeling of structural members has been adopted by a number of research studies to help determine the displacement of a structural member due to blast loading. Both the ASCE 59-11 (ASCE, 2011) and CSA S850 (CSA, 2012) apply the Biggs (1964) model to determine the anticipated deformation experienced by structural members subjected to blast loading. The only deviation of the code approaches from the aforementioned model is that a constant is applied to increase the resistance of materials to blast loading due to the significant increase in the strain rate of the constituent materials. Both Canadian and American codes have defined the maximum support-end rotations during the dynamic response of a structural member as being the limiting value to determine the post-blast

condition of the member for the majority of the damage limits. The only response limit which is not limited by the support rotation is the first response limit, which is limited by the deflection ductility ratio. For masonry, the lowest damage limit requires a ductility ratio of 1, while the largest damage limit prior to failure specifies a maximum support end rotation between 1.5 and 15 degrees (CSA, 2012; ASCE 2011).

### ***1.5.12 FLEXURAL PANEL TESTING***

Primarily, research on masonry or concrete structural flexural members has been limited to the panels retrofitted with different layering types of reinforcing polymers and steel beam-column reinforcement to provide additional flexural resistance. Razaqpur et al. (2007) performed a study on concrete flexural panels of size similar to those investigated in this study, and strengthened with GFRP to determine the response change due to the addition of the GFRP. The Urgessa and Maji (2010) test program consisted of full scale reinforced masonry wall strips, 3 m tall x 1 m wide x 200 mm thick, strengthened with FRP. Abou-Zeid et al. (2011) subjected full scale unreinforced masonry walls, 2.2m tall x 990 mm x 200 mm thick, both strengthened and unstrengthened with cold-formed steel sections, to blast loading. Additional research has been performed on unreinforced masonry walls in an attempt to quantify the level of protection generated by masonry walls and the effect of arching mechanisms on the level of protection (Abou Zeid et al., 2011). However, very little research has been undertaken on the performance of reinforced masonry flexural wall panels subjected to blast loading. Only one study was found that determines the viability of single degree of freedom models for predicting the deflection of masonry under blast loading (Browning et al., 2010). Research in the development of *P-I* diagrams has been thoroughly investigated, as several researchers have utilized *P-I* diagrams in forming conclusions regarding blast resistances (Zadeh, 2011; Abedini et al., 2013; Shi et al.,

2007; Nalagotla, 2013). These tests have been undertaken with the intent to determine the response of masonry or concrete retrofitted with various post-construction reinforcing methods in an attempt to quantify the potential increase in level of protection of existing masonry or concrete structures.

Experimental data for modern reinforced masonry flexural panels subjected to blast loading is lacking because historically, researchers have been more concerned with the reaction of retrofitted unreinforced masonry. With reinforced masonry being a widely structural system, additional research should be undertaken in order to fully understand the structural response of masonry subjected to blast loading. A larger pool of experimental data is required to validate the assumptions of SDOF models for masonry. This is necessary because typically designers use SDOF models to determine the response of structural systems, including masonry, under various types of dynamic loading.

The objective of this thesis is to further provide experimental data for reinforced masonry flexural walls in order to capture the dynamic reactions and properties exhibited by masonry. The responses of the flexural walls are compared to the predictions obtained from linear and non-linear SDOF models to validate assumptions, and *P-I* diagrams are developed to further the knowledge base for reinforced masonry flexural walls.

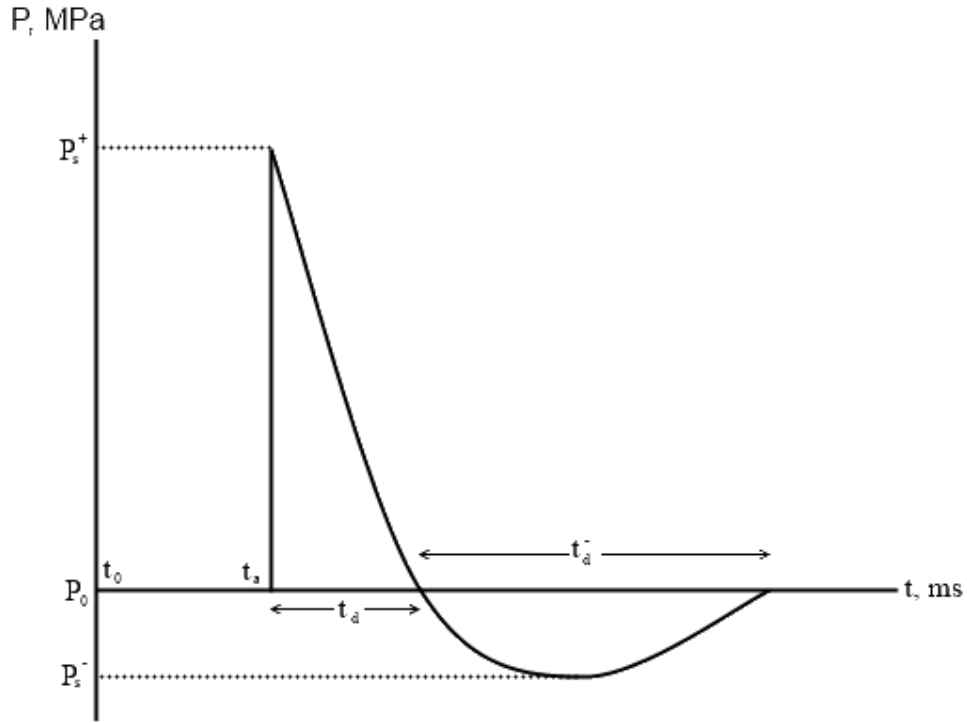


Figure 1.1: Typical pressure profile

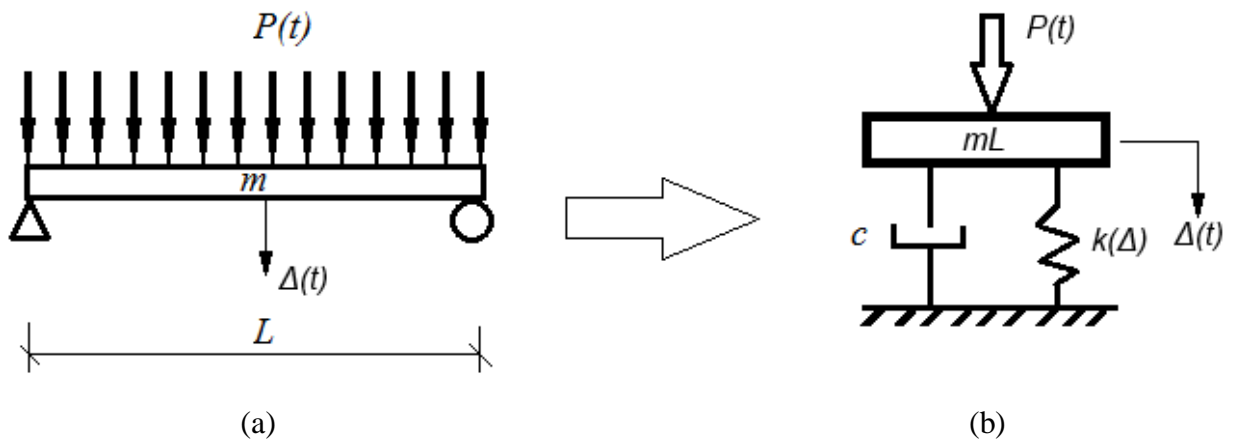


Figure 1.2: Conversion of (a) actual system to (b) equivalent SDOF system

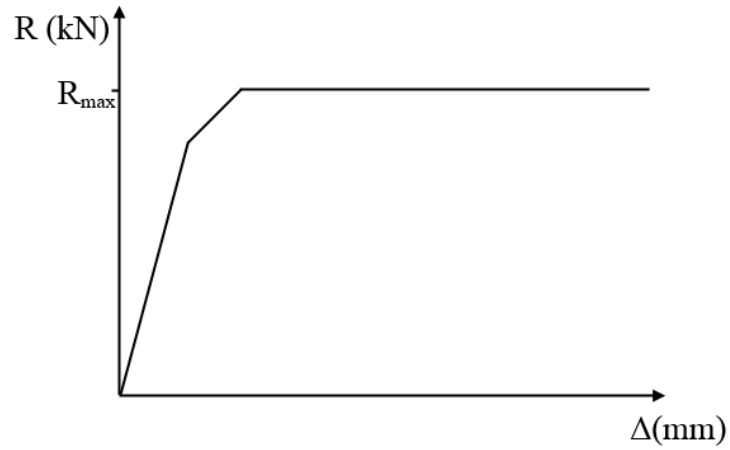


Figure 1.3: Typical Resistance Function for one-way slab

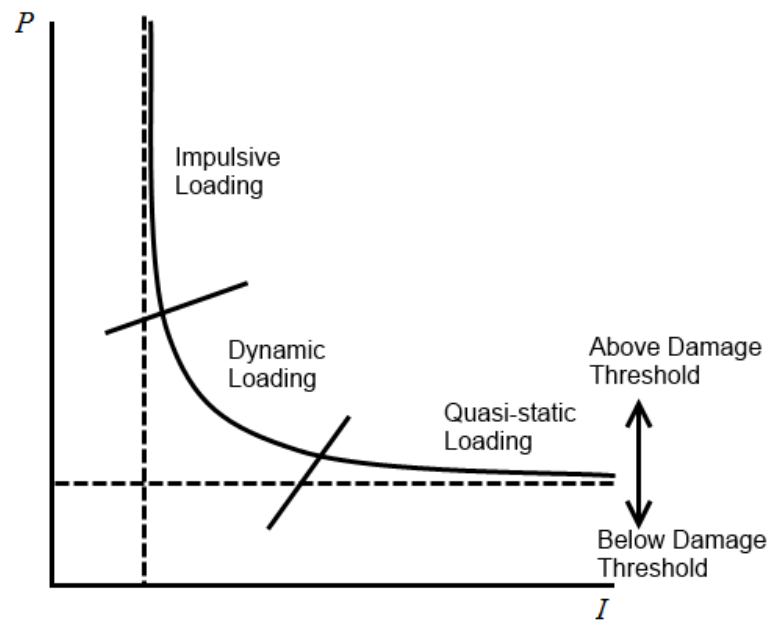


Figure 1.4: Qualitative representation of pressure-impulse diagram and the associated response regimes

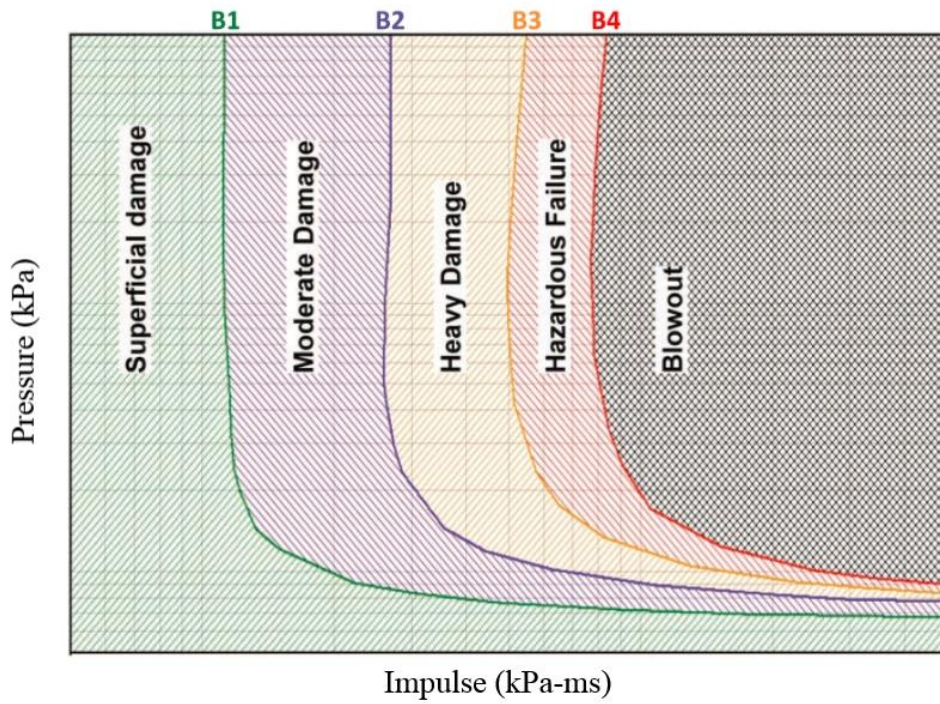


Figure 1.5: Typical pressure impulse diagram (CSA, 2012)

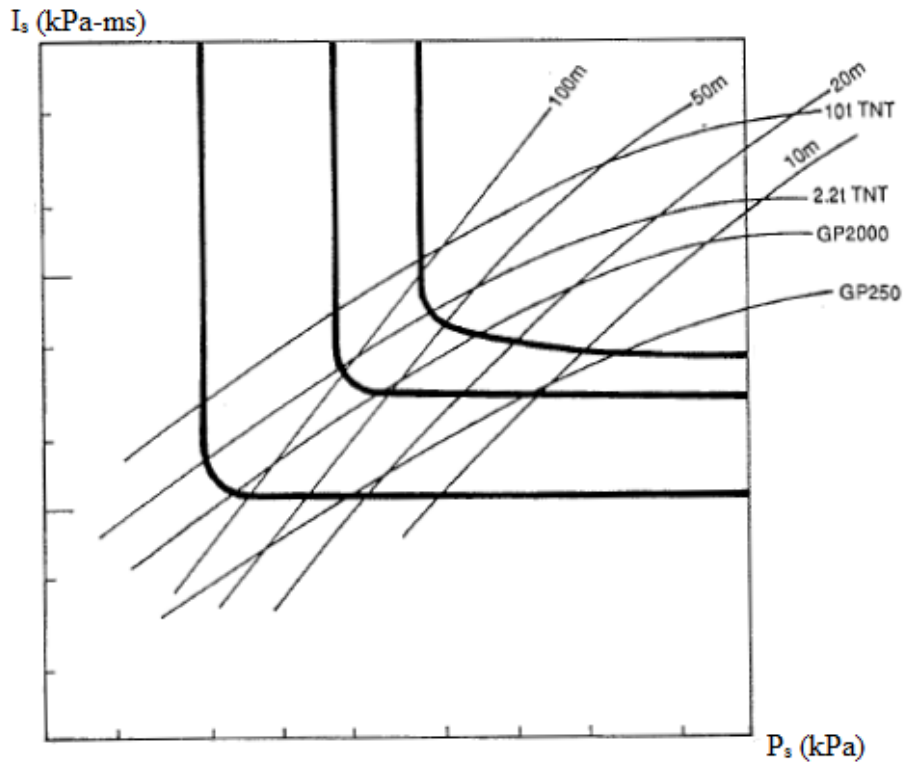


Figure 1.6: Superposition of scaled distance curves on P-I diagrams (Smith and Hetherington, 1995)

Table 1.1: TNT Equivalent for Common Explosives (Baker et al., 1983; Smith and Hetherington, 1994)

Explosive Material	Mass Specific Energy $Q_f$ (kJ/kg)	TNT Equivalency ( $Q_f/Q_{TNT}$ )
ANFO	3028	0.670
Compound B (60% RDX, 40% TNT)	5190	1.148
Cyclotrimethylene Trinitramine (C4) (91% RDX, 9% Plasticizer)	4870	1.078
Nitroglycerin (Liquid)	6700	1.481
Pentolite 50/50 (50% PETN, 50% TNT)	5110	1.2 – 1.5
Semtex	5660	1.250
Trinitrotoluene (TNT)	4520	1.000

Table 1.2: Transformation Factors for various loading conditions (Biggs, 1964)

Loading Condition			Strain Range	Load Factor, $K_L$	Mass Factor, $K_M$		Load-Mass Factor, $K_{LM}$	
Left Support	Loading Distribution	Right Support			Concentrated Mass	Uniform Mass	Concentrated Mass	Uniform Mass
Pin	Uniformly Distributed	Roller	Elastic	0.64		0.50		0.78
			Plastic	0.50		0.30		0.66
Pin	Point Load at Centre	Roller	Elastic	1.0	1.0	0.49	1.0	0.49
			Plastic	1.0	1.0	0.33	1.0	0.33
Pin	Point Load @ $L/3$	Roller	Elastic	0.87	0.76	0.52	0.87	0.60
			Plastic	1.0	1.0	0.56	1.0	0.56
Fixed	Uniformly Distributed	Fixed	Elastic	0.53		0.41		0.77
			Plastic	0.50		0.33		0.66
Fixed	Point Load at Centre	Fixed	Elastic	1.0	1.0	0.37	1.0	0.37
			Plastic	1.0	1.0	0.33	1.0	0.33

## CHAPTER 2 – BLAST RESPONSE OF ONE-WAY REINFORCED CONCRETE BLOCK FLEXURAL WALLS

### 2.1 ABSTRACT

Blast resistant design has only more recently been codified in the USA and Canada through ASCE 59-11 “Blast Protection of Buildings” (ASCE, 2011) and CSA S850-12 “Design and Assessment of Buildings Subject to Blast Loads” (CSA, 2012), respectively. The introduction of these relatively new design standards has demonstrated the lack of blast performance information pertaining to reinforced concrete masonry flexural wall systems designed and detailed essentially for wind and out-of-plane seismic loading. The current study focuses on experimentally assessing the performance of such walls under live explosive charges located at different standoff distances to induce different levels of damage. The effects of the explosion level, corresponding to different design basis threats (DBT), on the wall response were quantified in terms of the wall mid-height deflection and subsequent chord rotation. Based on the observed damage states, the test walls would result in a range of levels of protection (LOP) depending on the DBT. In general, the results show that reinforced masonry flexural wall systems can safely withstand relatively high blast load levels with minor damage. The study is also expected to facilitate a better linkage between quantitative and qualitative damage state indicators in future editions of the ASCE 59 and the CSA S850 codes.

**KEYWORDS:** blast loads, concrete masonry, reinforced masonry blast response, third-scale testing

## 2.2 INTRODUCTION

In recent years there has been an increased emphasis on the design of structures to accommodate the accidental or deliberate effects of blast loading. Due to the threat that such impulsive loading imposes on structures, a number of recent research programs have focused on the performance of unreinforced masonry (Abou-Zeid et al., 2011; Baylot et al., 2004), steel (Lew et al., 2013; Nassr et al., 2012), and reinforced concrete (Razaqpur et al., 2011; Wang et al., 2012) structural elements under blast loads. With the current Canadian and American standards for the design of blast resistant structures (CSA S850-12 “Design and Assessment of Buildings Subject to Blast Loads” (CSA, 2012) and ASCE 59-11 “Blast Protection of Buildings” (ASCE, 2011)) recently introduced, they are still in the early stages of standard development and design provision optimization.

Recent studies on the behavior of masonry walls under blast loading have primarily focused on unreinforced masonry (URM) and its out-of-plane capacity (Abou-Zeid et al., 2011; Baylot et al., 2005; Myers et al., 2004; Wei and Stewart, 2010), including the effect of arching on enhancing the out-of-plane blast response. Other studies include the increased out-of-plane capacity of URM through Fibre Reinforced Polymers (FRP) retrofit (Carney and Myers, 2005; Hrynyk and Myers, 2008; Myers et al., 2004; Urgessa and Maji, 2010). Whereas, studies that focus on quantifying the behavior of reinforced concrete (RC) members under blast loading (Rong and Li, 2008; Silva and Lu, 2009; Williams and Williamson, 2011) have shown the ability of RC components to resist this type of loading. Similar studies focusing on modern masonry construction (reinforced concrete block walls), however, are limited (Mayrhofer, 2002, Browning et al., 2014).

Focusing on increasing the knowledge base pertaining to the out-of-plane performance of reinforced masonry walls under blast, this paper summarizes the test results of six third-scale reinforced concrete block flexural walls tested under different levels of explosions. The first objective of the study is to evaluate the performance of the walls through the analysis of the deflection response histories by linking the wall peak deflection and support (chord) rotation levels to different wall damage states. The second objective is to establish the expected building level of protection (LOP) classifications, as outlined in ASCE 59-11 (ASCE, 2011) and CSA 850-12 (CSA, 2012), under different explosive charge weight and standoff distance combinations representing a range of design basis threat (DBT) levels. Finally, the third objective is to evaluate the capabilities of a simplified Single Degree Of Freedom (SDOF) in predicting the wall peak deflections, and thus their damage states.

### **2.3 EXPERIMENTAL PROGRAM**

Six third-scale reinforced concrete block walls were constructed and tested with mid to far field blast loads, which were produced using various masses of Pentex-D explosives. All walls were constructed in a consistent manner in order to minimize workmanship effects on wall properties, with prior experience in the construction of third-scale masonry walls. The walls were constructed using a true replica of the standard 190 mm stretcher block and each wall measured approximately 7.5 blocks long (1,000 mm) by fifteen courses high (1,000 mm), as shown in Figure 2.1(a). All the walls were constructed with a running bond and built to adhere to common North American construction standards. A steel C127 x 4.8 section was connected to the base and top of each wall, which facilitated the wall transportation as well as providing the necessary wall boundary conditions when placed inside the steel test bunker as will be discussed later. The

following sections present the details of the materials used in wall construction, the experimental test set up, instrumentation used, and the test matrix for the experimental program.

### **2.3.1 MATERIALS**

During construction, weight proportioned Type-S mortar was used with Portland cement:lime:sand proportions of 1:0.2:3.53. Following the CAN/CSA A179-04 (CSA, 2009a), water was gradually added to the mixture in order to achieve acceptable workability as determined by the mason. The compressive strength of each mortar batch was determined through the casting of three 50 mm cubes, and mortar that was not used within one hour after being mixed was discarded. All mortar tests were performed in accordance with CAN/CSA A3004-C2 (CSA, 2008). The average flow of the mortar was approximately 128%, with a coefficient of variance (COV) of 4.7%. In total, 15 mortar cubes were tested with the average compressive strength found to be 30.3MPa, with a COV of 5.2%.

A fine grout, produced according to CAN/CSA A179-04 (CSA, 2009a), was used during construction and was weight proportioned with Portland cement:sand to 1:3.9. Water was added to the mixture to provide adequate slump while maintaining desired strength. The compressive strength of the grout used was determined through the casting of grout cylinders, 100 mm in diameter and 200 mm in height. All grout compressive tests were performed as specified by CAN/CSA A23.2-3C (CSA, 2009b), producing an average grout compressive strength of 23.0MPa, with a COV of 6.9%.

For each mortar batch used in the construction the Group I and II walls, two four-block high prisms were constructed to test the compressive and flexural strength of the masonry prisms normal to the bed joints. The compressive strength and elastic modulus were 20.8 MPa (COV 9.6%) and 11.8 GPa (COV 9.8%) respectively, as tested according to CSA S304.1 (CSA, 2009c).

Three different types of steel reinforcement were used during construction. Deformed D4 (26 mm<sup>2</sup> average area) and D7 (45 mm<sup>2</sup> average area) bars were used as vertical reinforcement in the specimens. Smooth W1.7 bars (11 mm<sup>2</sup> average area) were used as horizontal reinforcement and hooked at the end to accommodate the outermost vertical reinforcement. Using the 0.2% offset, the average idealized yield strength of the D4 and D7 bars was equal to 478 MPa (COV 0.99%) and 484 MPa (COV 4.15%), respectively, whereas, the W1.7 steel bars had an average yield strength of 270 MPa (COV 2.33%). The two different wall cross-sections are shown in Figure 2.1(b).

### **2.3.2 TEST SETUP**

The blast test bunker was constructed using six HSS sections, 102 x 152 x 12 mm, welded together to provide support for the test wall when subjected to the blast loads. The reaction supports for the C127 x 4.8 steel channels were provided by two 50.8 mm diameter cylindrical solid steel sections, which were welded to the middle of both the top and bottom HSS sections, resulting in simply supported boundary conditions. Six additional HSS 102 x 102 x 12 mm sections were welded across the back of the test bunker in order to provide support for the instrumentation support frame. To prevent the blast wave engulfing phenomenon (Baker et al. 1983), the bunker was encased by 6.4 mm thick steel plates to create a closed box configuration. In addition, steel wing walls and steel parapet (shown in Figure 2.2(a)) were utilized to minimize the blast wave clearing effect, which is a common phenomenon that can result in significant variations of the pressure and impulse applied to the specimen (Baker et al. 1983).

The Pentex-D explosive material used has a TNT equivalence ranging from 1.2 to 1.5 (Orica, 2013), as such, a conservative factor value of 1.2 is assumed throughout this study. The charge sizes used reflect those of potential DBTs that an at-risk flexural wall could be exposed

to. The DBTs are based on the Hopkinson-Cranz (Smith and Hetherington, 1994) cube root scaling method for the scaled distance,  $Z$  in  $m/kg^{1/3}$ , shown in Eq.(1.5) to compare threat levels.

### 2.3.3 INSTRUMENTATION

Three Displacement Potentiometers (DPs) (model Penny+Giles SLS190-300 (Penny+Giles, 2012)) with a maximum stroke of 300 mm were installed on the rear face of each wall to record the horizontal displacements. The first, DP1, was located at the center-line of the wall at its mid-height (i.e. 500 mm above the base of the wall - 8<sup>th</sup> course), the second, DP2, at the center-line of the wall at 750 mm above the base of the wall (11<sup>th</sup> course), and the third, DP3, at 750 mm from the base of the wall, 250 mm from the wall edge (11<sup>th</sup> course). These DPs were placed at three locations shown in Figure 2.2(c) and (d). Three piezoelectric pressure transducers (models ICP 113A21 (PCB, 1997) and Pizotron 211B2 (Kistler, 2012)), shown in Figure 2.2(d), were mounted to the exterior of the test bunkers to record the reflected pressure profile. were mounted to the exterior of the test bunkers to record the reflected pressure. Two of the three exterior pressure transducers were placed on either side of the wall at its mid-height (i.e. 500 mm above the wall base). The final exterior pressure transducer was placed 250 mm above the wall (i.e. at a height of 1,250 mm from the wall base). An additional transducer was placed inside the test bunker, and was used to measure any possible internal pressure variation. All pressure and displacement data was simultaneously recorded at a 1 MHz sampling rate.

### 2.3.4 TEST MATRIX

The six walls were divided into two groups, based on the reinforcement ratio (Low and High) as indicated in Figure 2.1(b), and labeled based on the charge weight (6 for the blast containing 6 kg of equivalent TNT, 12 for the blast containing 12 kg of equivalent TNT, and 30

for the blast containing 30 kg of equivalent TNT). Each of the six walls was subjected to a single blast load, varying the charge mass while keeping the standoff distance constant. The three different charge masses selected (6 kg, 12 kg, and 30 kg of equivalent TNT), resulted in scaled distances of 2.75, 2.18, and 1.61  $m/kg^{1/3}$ , respectively. These scaled distances were selected to represent different design basis threats (DBT), which would impose varying damage levels on the walls.

*Group I* consisted of walls that were fully grouted and reinforced with a single D4 bar in every grouted cell (i.e. 65 mm spacing). *Group II* consisted of fully grouted walls, reinforced with a single D7 bar in every cell (i.e. at 65 mm). Both sets of walls were constructed with a single W1.7 bar at every course as horizontal reinforcement. The reinforcing layout is shown in Figure 2.1(b). By varying the vertical reinforcing ratios, their effects on the wall performance under different DBT can be quantified.

### 2.3.5 CRACK PATTERNS

#### 2.3.5.1 GROUP I

Wall WML6 was subjected to a 6 kg charge weight blast which resulted in a full-width bed joint crack at the 9<sup>th</sup> course and a partial width bed joint crack was observed at the 10<sup>th</sup> course of the wall rear face. The loaded face of the wall did not experience any damage. The post-blast damage is shown in Figure 2.3(a) for the rear face of the wall, and Figure 2.3(b) for the loaded face of the wall.

Wall WML12 was subjected to a 12 kg blast, and damage was observed, along with a permanent deflection at the mid-span of the wall. At the rear face of the wall, bed joint cracks were found between the 5<sup>th</sup> and 14<sup>th</sup> courses and slight spalling was noted at the loaded face of

the wall. The post blast damage of the rear and loaded face of the wall is shown in Figure 2.3(b) and Figure 2.3(d) respectively.

Wall WML30, exposed to a 30 kg blast, suffered the highest level of damage within the experimental program, as the wall fractured in half at the bed joint of the 9<sup>th</sup> course. At the rear face of the wall extensive bed joint cracks developed between the 3<sup>rd</sup> course and the 13<sup>th</sup> course with most of the cracks extending across the entire width of the wall. Multiple head joint cracks were also observed throughout the wall. The damage to the loaded face of the wall was primarily in the form of full-width bed joint cracks at each of the 8<sup>th</sup> to 11<sup>th</sup> courses. With the splitting of the wall, steel fracture through bar necking was clearly evident. The wall damage is shown in Figure 2.3(e) for the rear face and Figure 2.3(f) for the loaded face.

#### 2.3.5.2 GROUP II

Wall WMH6 was the first of this group to be tested under the 6 kg charge weight, and caused neither visible cracking damage nor recorded permanent deformation. The wall is included in Figure 2.3(g) and Figure 2.3(h) for completeness.

Wall WMH12 was subjected to a 12 kg blast and little blast-induced damage was observed. It was found that the rear face of the wall experienced full-width bed joint cracks shown in Figure 2.3(i). Following the explosion the observed residual cracks were hairline cracks. Given the lack of damage, the loaded face is shown for completeness in Figure 2.3(j).

Wall WMH30 was tested at a blast load of 30 kg. Following the blast, it was noted that the damage was in the form of full-width bed joint cracks extending on the rear face of the wall, as well, vertical cracks were also observed with the longest of these cracks extending from the 6<sup>th</sup> to the 11<sup>th</sup> course while additional vertical cracks extended through a single course. Mortar spalling was observed at the rear face of the wall, as the bond between the mortar and the concrete blocks

was lost. At the loaded face of the wall, full width bed joint cracks were observed, and along with these cracks, spalling of the faceshells occurred which revealed the vertical reinforcement of the wall. The observed blast-induced damage for the rear face of the wall is shown in Figure 2.3(k). The observed post-blast damage for the loaded face of the wall is shown in Figure 2.3(l).

## 2.4 ANALYSIS OF TEST RESULTS

### 2.4.1 *PRESSURE PROFILES*

The reflected shock wave pressure profiles, which were recorded by the pressure transducers mounted on the frame, are shown in Figure 2.4 and further detail into typical pressure profiles is found in Section 1.5.2. Due to ringing of the pressure gauges as a result of vibration generated by the blast, difficulties arose when attempting to quantify the blast wave characteristics, such as the peak pressure, the impulse and the positive phase duration, from the experimental data. Therefore, the pressure data was fitted using the Modified Friedlander equation, given by Eq.(1.4), through a least squares regression analysis. The comparison between the experimentally-fitted values and the theoretically calculated results for the pressure and impulse are shown in Table 2.2. To determine the theoretical reflected peak pressure and total specific impulse values of the blast wave, ConWep (Hyde, 1993) was used. A ratio between the values for the pressure,  $P_{experimental}/P_{theoretical}$ , and total impulse,  $I_{experimental}/I_{theoretical}$ , is taken to determine the consistency between the experimentally fitted results and theoretical values. The average of these values are found to be 0.97 (COV of 7.4%) and 1.01 (COV of 9.9%), respectively, which indicates good agreement between the experimental blast measurements and the values predicted using ConWep.

#### 2.4.2 DISPLACEMENT HISTORIES

The recorded displacement response occurring at the 8<sup>th</sup> and 11<sup>th</sup> courses of the walls is presented in Figure 2.5 and shown in Table 2.3 Positive values indicate displacements away from the blast source while negative values indicate displacement towards the blast source. Displacement potentiometers DP2 and DP3 provided consistent results across all tests, which supports the assumption that the walls acted in one-way bending. Additionally, based on beam theory, the  $\frac{3}{4}$  height deformation of the wall should be equal to approximately 72% of the deformation of the mid-height deformation. Overall, this was found to be in agreement with the displacements measured by the DPs.

For *Group I* walls, negligible damage was sustained by wall WML6, which is realized by the recorded peak displacement of 15.6 mm. At the increased charge mass of 12kg, wall WML12 experienced a peak displacement of 37 mm while undergoing residual permanent displacement. Due to the substantial damage sustained to wall WML30, the displacement response measured by the DPs is not considered meaningful and is not considered in this study.

For the *Group II* walls, WMH6, and WMH12, did not undergo significant deformations during their respective tests, experiencing similar peak displacement values of 14.6 mm and 18.1 mm, respectively, which was accompanied by minimal damage during the blast tests. As such, these deformations were also close to the walls' elastic response limit. Wall WMH30 underwent large level of plastic deformations, as the wall reached a peak deformation of 50.8 mm. As the concrete at the loaded face of the wall crushed, additional cracks developed at the wall's rear face, causing additional deformations, which in turn resulted in additional crushing.

### 2.4.3 SIMPLIFIED SINGLE DEGREE OF FREEDOM MODEL

In order to evaluate the capabilities of predicting the experimental wall response using simplified single degree of freedom (SDOF) models, the current study adopted the following assumptions for simplification: strain rate effects were ignored; an equivalent triangular pressure profile is utilized based on the values of positive phase duration and peak positive pressure generated by the Modified Friedlander fit; prior to the onset of damage, the gross moment of inertia is used and at the onset of damage, the effective wall moments of inertia were evaluated as the average of the that of the cracked and gross wall cross sections following the procedure suggested by Biggs (1964) and UFC-3-340-02 (USDOD, 2008). The goal of this model is to solve the equation of motion, given in Eq. (1.32) to capture the peak deformation as the key wall damage indicator.

In this equation,  $K_{LM}$  represents the load-mass transformation factor developed in Biggs (1964),  $m_t$  is the mass of the wall,  $k_t$  is the wall stiffness,  $F_t$  is the applied blast force,  $\ddot{\Delta}(t)$  is the wall mid span acceleration, and  $\Delta(t)$  is the wall mid-span deflection. These three parameters must be established in order to solve the dynamic equation of motion. The first of these parameters, mass  $m_t$ , and is evaluated in Eq. (2.1) for a simply supported wall with uniformly distributed mass,  $m$  along the length,  $L$  in meters.

$$m_t = mL \quad (2.1)$$

The second parameter established is the resistance,  $k_t$ , of the wall which is dependent on the elastic modulus,  $E$ , of the masonry prisms and the moment of inertia,  $I_{av}$ , equal to the average between the gross and cracked section moment of inertia, in addition to the aforementioned length. The wall stiffness is given by Eq. (2.2)

$$k_t = \frac{384EI_{av}}{5L^3} \quad (2.2)$$

Finally, the forcing function,  $F(t)$ , is defined by an assumed triangle pressure profile based on the blast parameters developed in the modified Friedlander fit. The conversion from an idealized blast pressure profile, shown in Figure 2.6(a) to a triangular blast pressure profile is shown in Figure 2.6(b), and is represented in Eq.(2.3)

$$F(t) = \begin{cases} P_{\max} \left(1 - \frac{t}{t_d}\right), & t < t_d \\ 0, & t \geq t_d \end{cases} \quad (2.3)$$

where  $P_{\max}$  is the peak pressure as evaluated in the modified Friedlander fit.

The values from Eq.(2.1), (2.2), and (2.3) are inserted into Eq.(1.32) to become Eq.(2.4)

$$K_{LM}(mL)\ddot{\Delta}(t) + \left(\frac{384EI}{5L^3}\right)[\Delta(t)] = \begin{cases} P_{MAX} \left(1 - \frac{t}{t_d}\right), & t < t_d \\ 0, & t > t_d \end{cases} \quad (2.4)$$

The  $K_{LM}$  factor for this simplified model is taken as the value derived from Biggs (1964) for that of a simply supported beam with uniformly distributed load undergoing perfectly elastic deformation, and is equal to 0.78 (Biggs, 1964).

#### **2.4.4 SINGLE DEGREE OF FREEDOM MODEL DISPLACEMENT PREDICTIONS**

Applying the SDOF model described above, theoretical displacement profiles of the walls were calculated and are shown in Figure 2.7. As can be inferred from Table 2.3, the SDOF model gives a better representation of the peak deflection for the specimens subjected to a lower charge weight. As the charge weight increases, the error between the experimental and theoretical results increases with the exception of Wall WMH30. It is postulated that this is

partially attributed to using the averaged cracked moment of inertia and the gross moment of inertia values for the entire displacement profile for walls which experienced cracking.

When the model is used to predict the response of *Group I* walls, a large variation is found between the experimental and predicted wall responses. Based on the wall damage described previously, wall WML6 encountered slight cracking as little damage was observed; experiencing an experimental peak deflection of 15.6 mm, while a theoretical displacement of 17.3 mm is generated through the model, which results in an 11% error. With damage on both of the faces of the wall, Wall WML12 deflected a peak of 37.0 mm during testing. Using the model outlined, a displacement of 28.8 mm is predicted, which results in an error of -28%. Wall WML30 fractured in half during the experimental program. As such, no peak deflection was recorded for this wall. However, the model predicted that the wall would have deflected 56.8 mm, which, based on the damage received during testing, underestimates the actual deflection of the wall.

For wall WMH6, due to the lack of observed damage during the experimental program, the gross moment of inertia is used to determine the peak displacement response of the wall. As a result of this substitution, the model was able to more accurately predict the peak displacement, as the theoretical peak value of 13.6 mm compared well with the experimentally recorded value of 14.6 mm, which indicates a -7% error, as the theoretical value is under predicts the experimental value. A comparison between these values is shown in Figure 2.7(a). Wall WMH12 experienced minor damage due to the 12 kg charge, as it only had a single bed joint crack at the rear face of the wall and as such the average of the gross and cracked sectional moments of inertia was used which yielded a 33% overestimation of the response of the wall, with the theoretical displacement response predicted to be 27.0 mm compared to the experimentally

recorded value of 18.1 mm (see Figure 2.7(b)). The 33% error between the theoretical prediction and experimental results shows the sensitivity of the stiffness in the model. Wall WMH30, exposed to the 30 kg charge weight, resulted in the closest model prediction to the experimental value based on error. A predicted peak deflection of 53.3 mm is compared favourably to the experimental value of 51 mm, which resulted in an error of approximately 5%. The comparison between the experimental results and theoretical predictions for Wall WMH30 is shown in Figure 2.7(e).

Overall, the SDOF model provided reasonable predictions for the experimental wall peak displacements. Nevertheless, because of its simplified assumptions regarding the moment of inertia and loading profile approximations, it is suggested that such SDOF be used mainly for preliminary design/screening purposes to determine an expected range of peak deflections of flexural masonry walls.

#### **2.4.5 QUALITATIVE AND QUANTITATIVE DAMAGE STATES**

In ASCE 59-11 and CSA S850-12, quantitative deflection and rotational response limits are imposed on structural components to be designed for blast. In addition, both the ASCE 59-11 and the CSA S850-12, identify qualitative response limits that are dependent on the level of damage incurred following an explosive event. The latter response limits are categorized to create a standardized method of classifying the different component damage states, ranging from “Superficial Damage” to “Hazardous Damage”. For the quantitative analysis, to be classified under “Superficial Damage”, the wall must experience no plastic deformations, as the  $\mu_{\Delta}$  (displacement ductility, equal to  $\Delta_{max}/\Delta_{el}$ ) must not be greater than 1. The classifications of “Moderate Damage”, “Heavy Damage” and “Hazardous Damage” require the support rotation to not exceed 2, 8, and 15 degrees, respectively. For the qualitative analysis on the other hand, to be

classified under “Superficial Damage”, visible permanent damage must not be likely; for the “Moderate Damage” classification, permanent damage may be visible, but easily repairable and the damage performed to the component is likely to not cause failure; to be classified under “Heavy Damage”, the component must undergo significant damage which is irreparable, but not likely to cause failure of the individual component; and finally, the “Hazardous Damage” classification requires the failure of the individual component.

Surpassing the “Hazardous Damage” response limit indicates complete component failure (CSA, 2012) and is classified as “Blowout” (CSA, 2012). The damage limits are then converted into building levels of protection (LOP) as a function of the role that the structural component (e.g. wall) serves in the building gravity load resisting system (CSA, 2012). To compare and categorize the walls into the varying damage limits outlined in CSA S850-12 and ASCE 59-11 based on the end wall rotation, both codes suggest (chord) support rotations, which assumes a plastic hinge is immediately formed, as the indication of different damage states. The experimental support (chord) rotations of the walls are shown in Figure 2.8, while the SDOF predicted support (chord) rotations are shown in Table 2.3.

The response limits experienced by *Group I* walls provide the largest variation of the response limits amongst walls tested during the experimental program. During the field testing, Wall WML6 experienced a support rotation of 1.8 degrees with minor permanent damage recorded. Due to the minor permanent damage, this wall is classified under the “Moderate Damage” damage limit (CSA, 2012). For comparison, the SDOF model predicted a support rotation of 2 degrees, which was consistent with the experimental wall damage state although being at the boundary of the “Heavy Damage” response limit (CSA, 2012). Wall WML12 was subjected to a support end rotation of 4.2 degrees, which classifies the wall under the “Heavy

Damage” damage limit (CSA, 2012). By comparison, the model developed generates a support rotation of 3.3 degrees, which also classifies the wall under the “Heavy Damage” response limit (CSA, 2012). Although both the SDOF model and the experimental results classify the wall under the “Heavy Damage” response limit (CSA, 2012), there is an approximately 20% difference between the experimental and the predicted rotations. During the experimental testing, Wall WML30 was completely damaged under the blast load, essentially fracturing in half. Because of the failure, rotational data was not meaningful. With the wall subjected to this significant damage, this wall exceeded the “Hazardous Damage” damage limit (CSA, 2012), and the wall is classified to have “Blowout” damage. The simplified SDOF model however predicted a rotation of 6.5 degrees, which would classify this wall under the “Heavy Damage” response limit (CSA, 2012).

For the *Group II* walls, rotations are generated for both the experimental and theoretical results. Based on the experimentally recorded peak wall deflection, the support rotation of wall WMH6 is calculated to be 1.7 degrees. However, based on the lack of permanent deformation recorded, this wall is classified under the “Superficial Damage” damage limit (CSA, 2012). The model developed a support end rotation of 1.6 degrees for this wall, however the elastic limit of this wall was exceeded and therefore the wall is classified under the “Moderate Damage” damage limit (CSA, 2012). For wall WMH12, an experimental rotation of 2.1 degrees is calculated. This rotation classifies this wall under the “Heavy Damage” damage limit (CSA, 2012), albeit on the border of being under the “Moderate Damage” damage limit (CSA, 2012). The experimentally derived rotation is compared to that derived by the simplified model, which is equal to 3.1 degrees. Similarly to the experimental results, the model classifies wall WMH12 under the “Heavy Damage” damage limit (CSA, 2012), however, unlike the experimental results,

the classification fell within the mid-bounds of the “Heavy Damage” damage limit. Lastly, in the field it is found that wall WMH30 was subjected to a support rotation of 5.8 degrees, which is associated with the “Heavy Damage” damage limit (CSA, 2012). This damage limit is the same as that derived by the simplified model, as a rotation of 6.1 degrees is calculated.

#### **2.4.6 WALL DAMAGE STATE CONSEQUENCE ON OVERALL BUILDING LOP CLASSIFICATION**

Being secondary structural components, primarily designed to resist the typical out of plane loads (e.g. wind and seismic) that a structural system might be subjected to, the pre-defined LOP are not as stringent those defined for primary structural elements, and equivalent to those specified for non-structural members. To provide a “High” LOP, the wall must undergo the “Superficial” damage state. Similarly, to provide a “Medium” LOP, the wall must undergo the “Moderate” damage state. To provide the “Low” and “Very Low” LOPs, the wall must undergo damage which quantifies it under the “Heavy” and “Hazardous” damage states respectively. Based on these requirements for the LOP, the provided LOP by the walls based on the experimental and theoretical results is shown in Table 2.4.

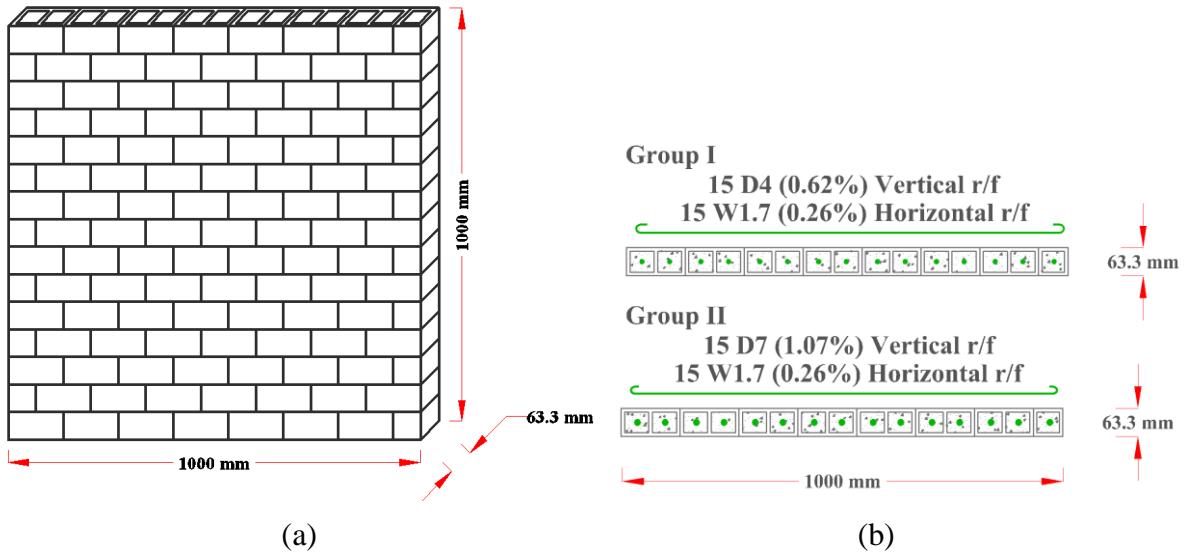
The comparison between the LOP, scaled distance ( $Z$ ), and reinforcement ratio (%) of the experimental data is shown in Figure 2.9. The amount of steel reinforcement heavily influences the LOP attained by the flexural wall at any given scaled distance. The LOP provided by the *Group I* walls decreased significantly as the scaled distance decreased, as the initial experimental observations classified this wall as providing “Medium” LOP for the lowest DBT. When the *Group I* wall was subjected to the highest DBT the wall did not provide any protection as it fractured in half, experiencing the “Blowout” damage state. The *Group II* walls generated the highest level of protection across all scaled distances due to the high reinforcement ratio.

Both the ASCE 59-11 and the CSA 850-12 share the same requirements for the damage states and the LOP provided. For both codes, structural elements which provide immediate occupancy and operational facility that is in full use are required to provide a “High” LOP, which corresponds to a damage limit of “Superficial Damage”. During this testing program, it was noted that only wall WMH6 achieved this damage state. Furthermore, to provide collapse prevention of the structural component, the “Very Low” LOP is required to be met, which corresponds to the “Hazardous Damage” damage state. During the testing program, there were no specimens that exceeded this damage state. This study has shown that the specimens can provide sufficient protection up to the “Heavy Damage” damage state for a DBT of up to  $Z=2.18\text{m/kg}^{1/3}$ . If additional detailing is performed, a DBT of up to  $Z=1.61\text{ m/kg}^{1/3}$  can safely be resisted while providing a sufficient LOP.

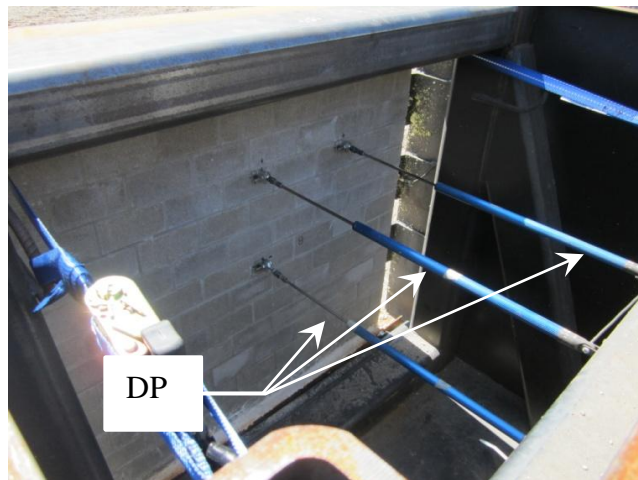
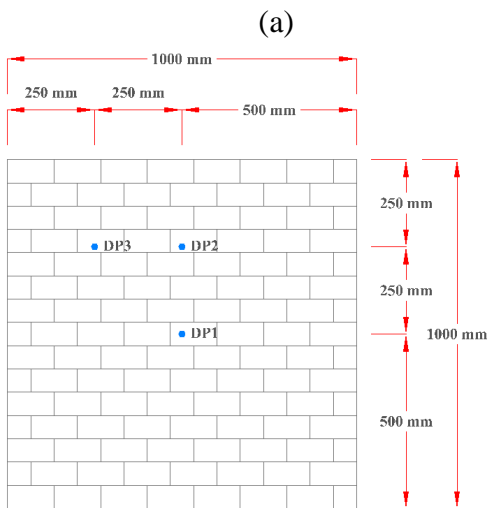
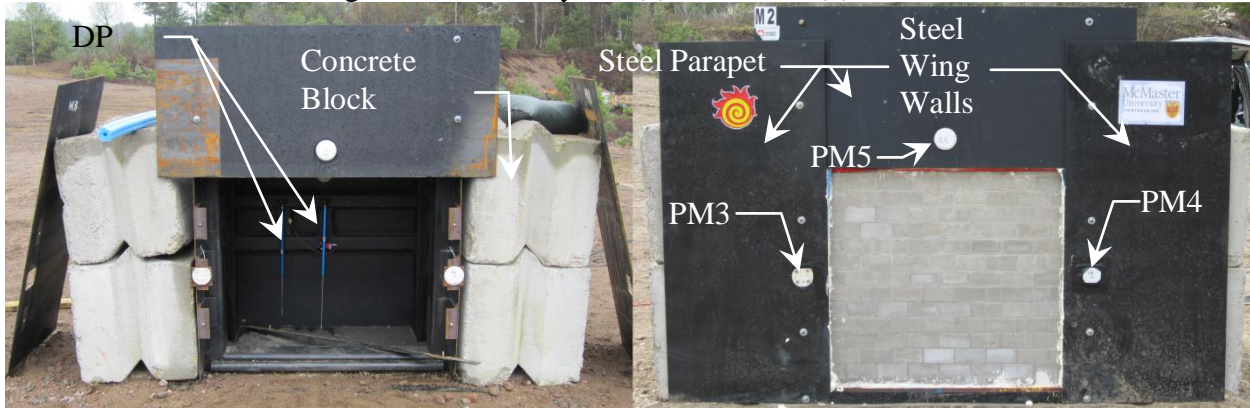
## **2.5 CONCLUSIONS**

The recent implementations of the standards for blast protection of buildings in Canada (CSA S850-12 “Design and Assessment of Buildings Subjected to Blast Load”) and USA (ASCE 59-11 “Blast Protection of Buildings”) have resulted in a situation where at-risk flexural masonry walls may be required to result in specific asset levels of protection (LOP). In this study, six third scale reinforced simply supported masonry walls were exposed to field blasts generated from three different design basis threat (DBT) levels to determine the displacement response and structural stability of varying reinforcing configurations. The study shows that, in general, the vertical steel reinforcement ratio has a major impact on the behavior of the flexure walls. Nevertheless, for the lowest DBT considered in the study, increasing the reinforcement ratio did not significantly alter the wall behavior. This was demonstrated through observing the wall damage states at the DBT corresponding to  $Z=2.75\text{ m/kg}^{1/3}$ . At this DBT, difference

between the deflection of wall WMH6 (14.57 mm deflection) and wall WML6 (15.55 mm) is fairly insignificant. Increasing the DBT however, causes the change in reinforcement ratio to significantly dictate the wall behavior, as seen in difference in deflection DBT of  $Z=2.18 \text{ m/kg}^{1/3}$  from 36.7 mm for Wall WML12 compared to 18.1 mm for Wall WMH12. The model used in this study was able to estimate the peak displacement of the walls when subjected to low DBT, with a relatively modest error in the range of -7% to 11%. As the DBT increased, the discrepancy between the predicted and measured the peak deflection values was found to increase.



(a) (b)  
Figure 2.1: Wall layout; (a) Elevation; (b) Plans



(c) (d)  
Figure 2.2: Experimental test setup; (a) Reaction frame pre-setup; (b) Reaction frame post-setup; (c) DP locations; (d) Interior instrumentation

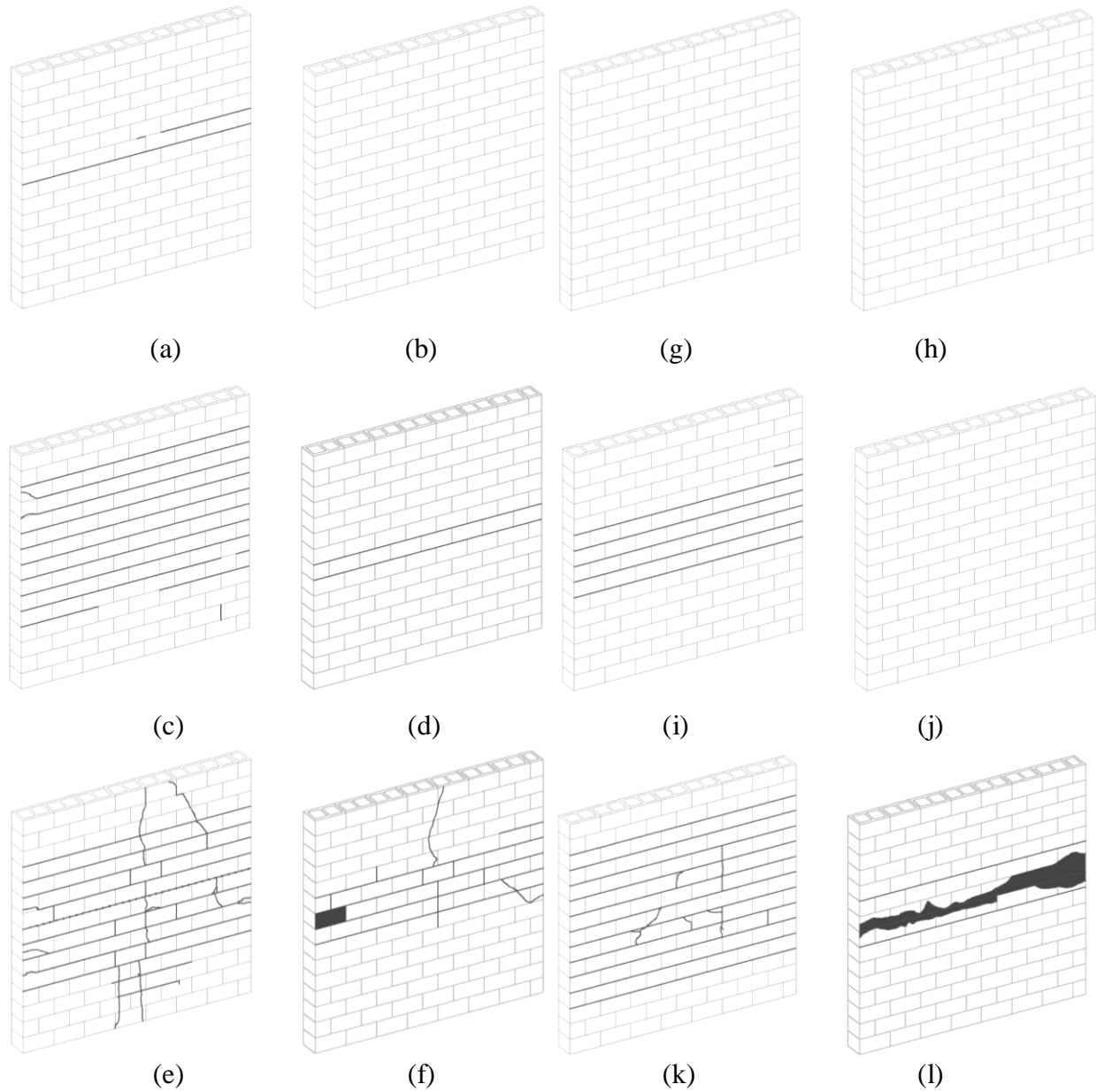
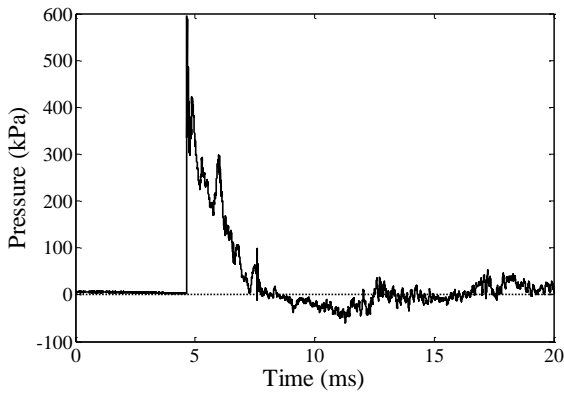
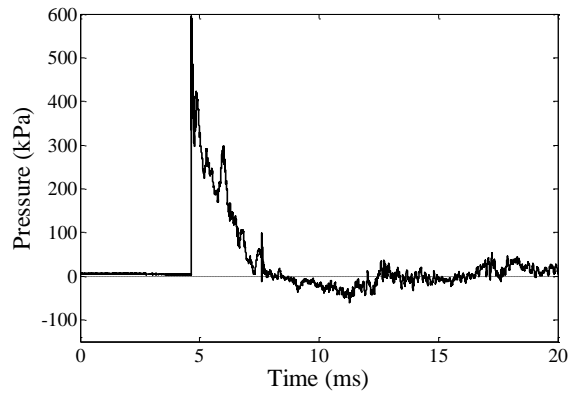


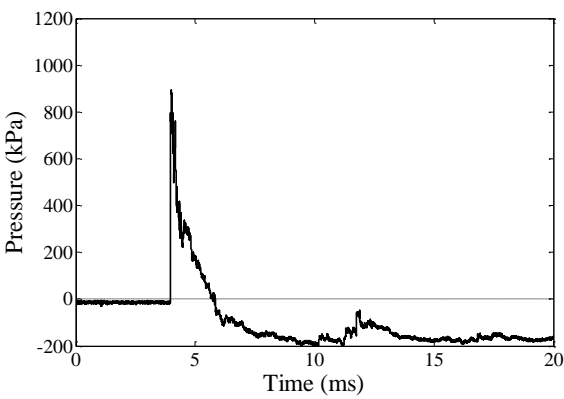
Figure 2.3: Observed post-blast damage; (a) Rear face of wall WML6; (b) Loaded face of wall WML6; (c) Rear face of wall WML12; (d) Loaded face of wall WML12; (e) Rear face of wall WML30; (f) Loaded face of wall WML30; (g) Rear face of wall WMH6; (h) Loaded face of wall WMH6; (i) Rear face of wall WMH12; (j) Loaded face of wall WMH12; (k) Rear face of wall WMH30; (l) Loaded face of wall WMH30;



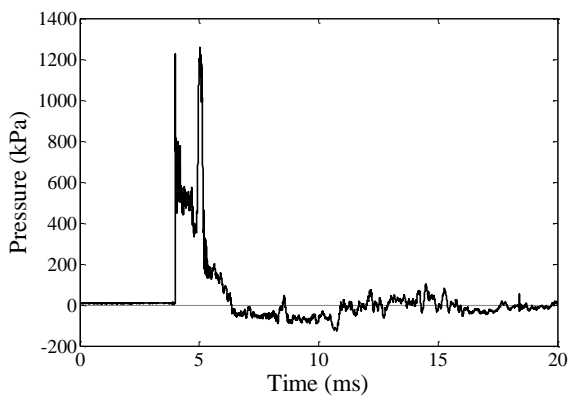
(a)



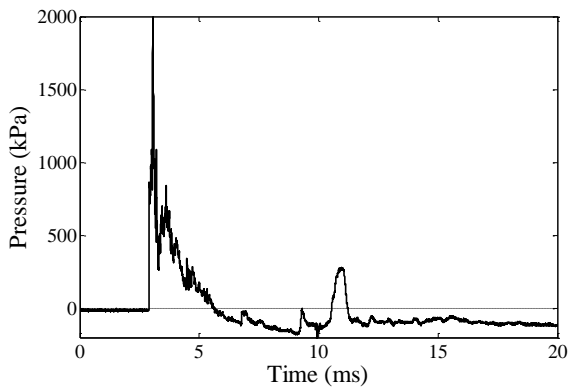
(d)



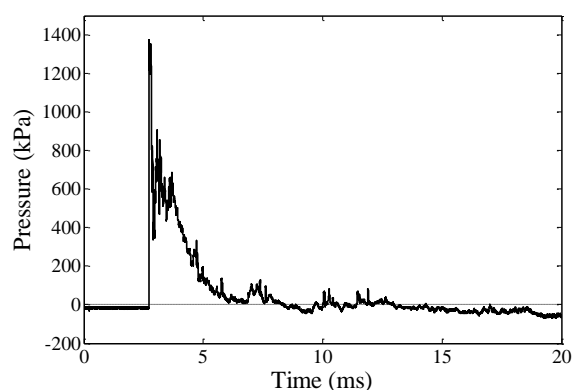
(b)



(e)



(c)



(f)

Figure 2.4: Experimental pressure profiles; (a) wall WML6; (b) wall WML12; (c) wall WML30; (d) wall WMH6; (e) wall WMH12; (f) wall WMH30;

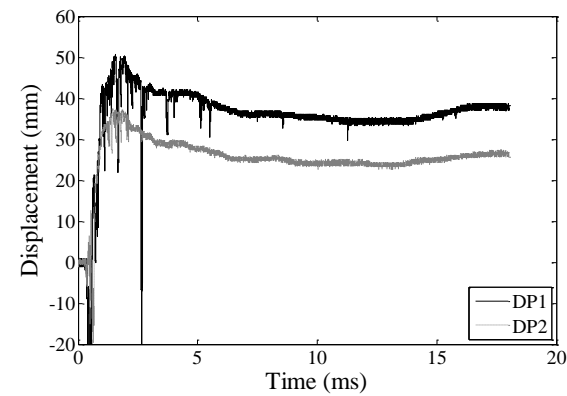
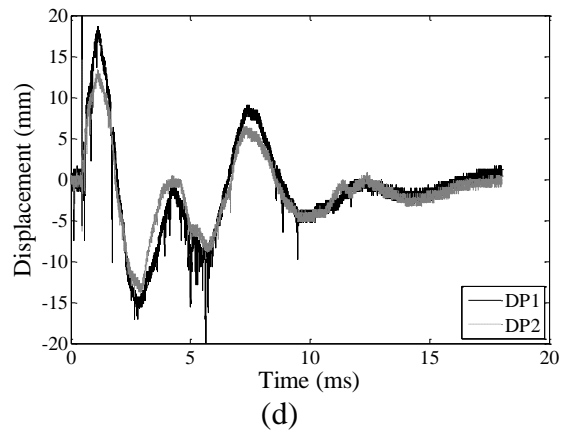
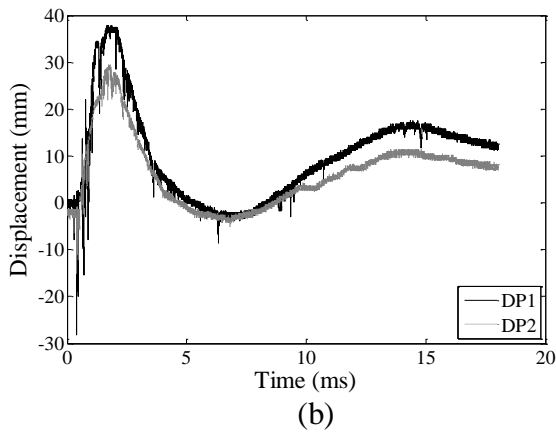
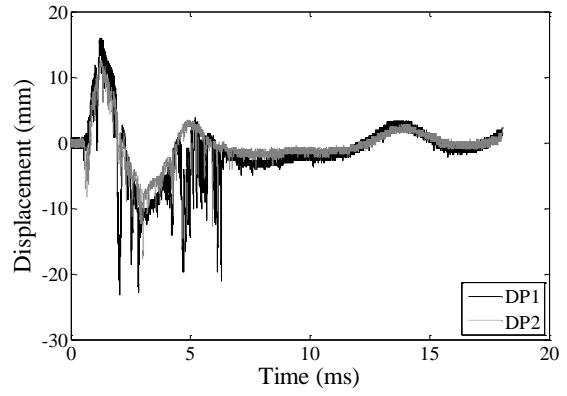
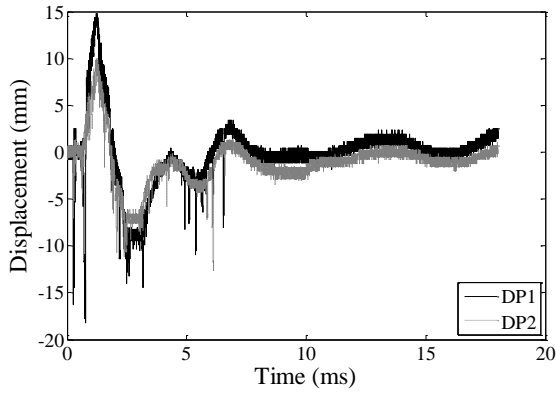


Figure 2.5: Displacement response at the 8th and 11th courses: (a) wall WML6; (b) wall WML12; (c) wall WMH6; (d) wall WMH12; (e) wall WMH30;

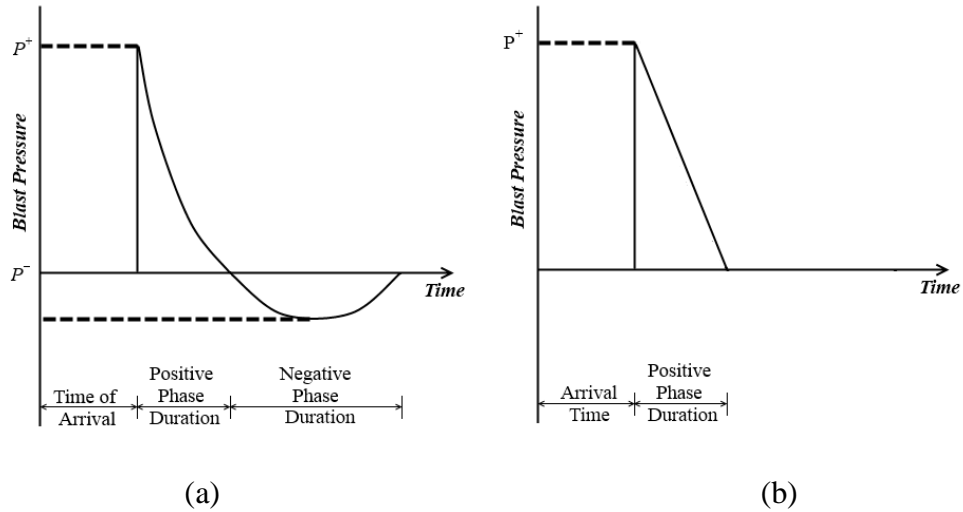
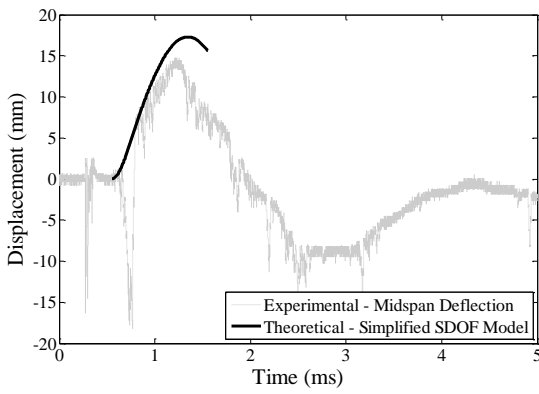
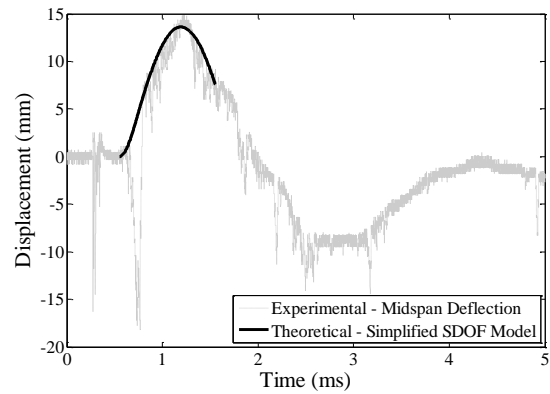


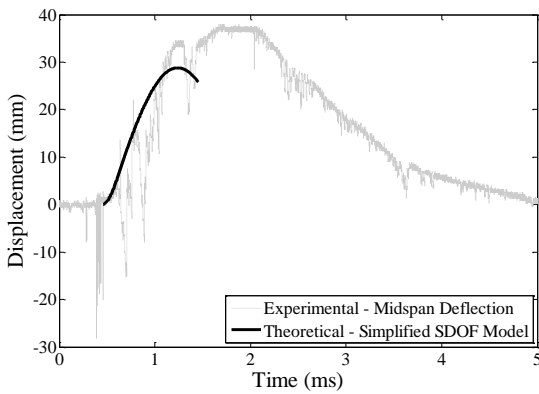
Figure 2.6: Experimental blast pressure; (a) Ideal pressure profile; (b) Triangular pressure profile



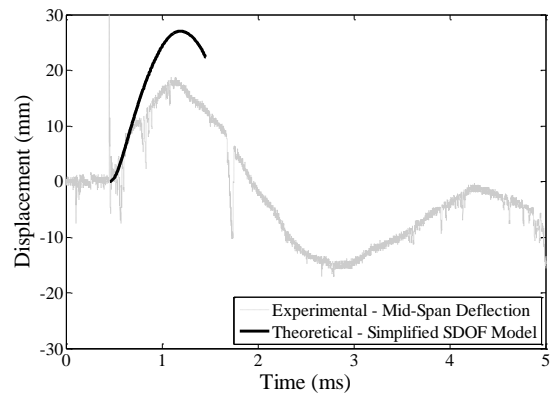
(a)



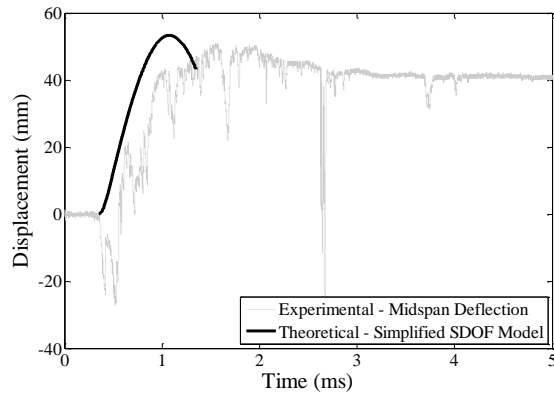
(c)



(b)



(d)



(e)

Figure 2.7: Experimental vs. theoretical deflection histories: (a) wall WML6; (b) wall WML12; (c) wall WMH6; (d) wall WMH12; (e) wall WMH30

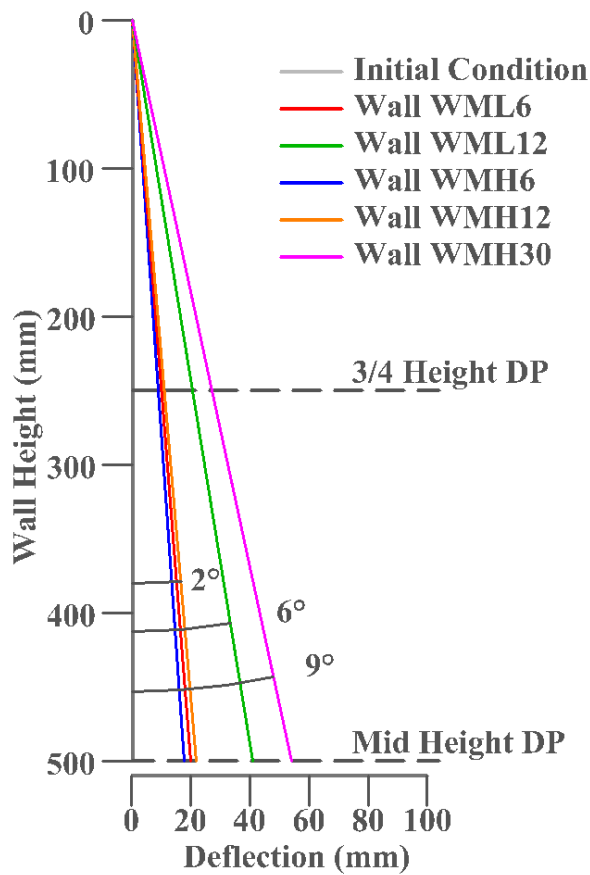


Figure 2.8: Upper segment wall deflection

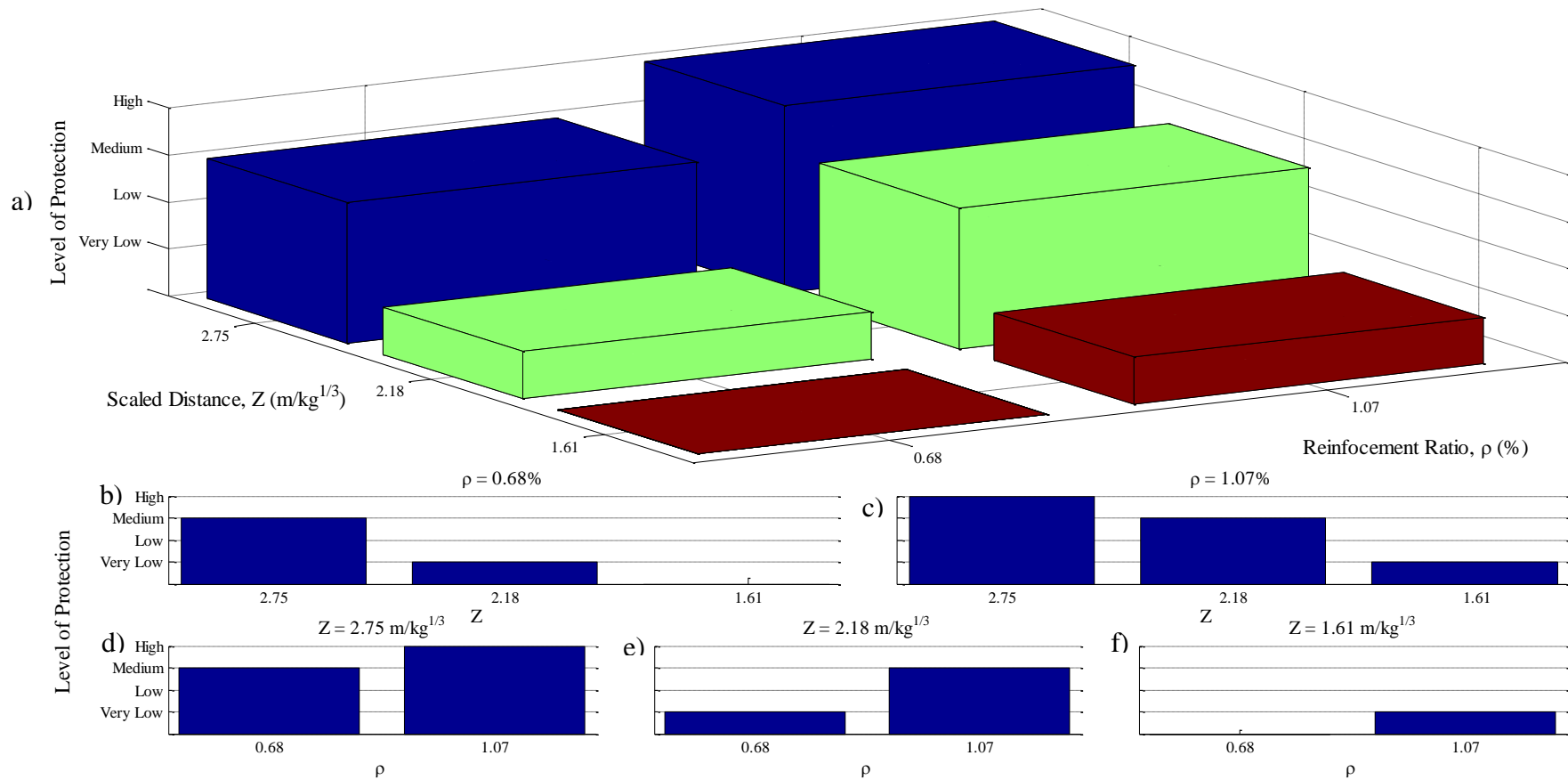


Figure 2.9 Effect of test matrix parameters on experimental damage state: a) Combined; b) Level of Protection provided by Group I ( $\rho = 0.68\%$ ); c) Level of Protection provided by Group II; d) Level of Protection at scaled distance =  $2.75 m/kg^{1/3}$ ; e) Level of Protection at scaled distance =  $2.18 m/kg^{1/3}$ ; f) Level of Protection at scaled distance =  $1.61 m/kg^{1/3}$ ;

Table 2.1: Test Matrix

Group	Wall	Grouting	Vertical Reinforcement		Horizontal Reinforcement		Stand-off Distance	Charge Weight (TNT eqv.)	Scaled Distance, Z (m/kg <sup>1/3</sup> )
			Number and Size	$\rho_v$	Number and Spacing	$\rho_h$			
I	WML6	Fully Grouted	15 D4 Bars (15 X 26mm <sup>2</sup> )	0.62%	15 W1.7 Bars every 63.3mm	0.26%	5m	6kg	2.75
	WML12						5m	12kg	2.18
	WML30						5m	30kg	1.61
II	WMH6	Fully Grouted	15 D7 Bars (15 X 45mm <sup>2</sup> )	1.07%	15 W1.7 Bars every 63.3mm	0.26%	5m	6kg	2.75
	WMH12						5m	12kg	2.18
	WMH30						5m	30kg	1.61

Table 2.2: Experimental vs. theoretical blast wave properties

Wall	Experimental/ConWep	
	P/P+	I/I+
WML6	0.96	1.03
WML12	1.06	0.90
WML30	0.86	1.07
WMH6	0.90	1.12
WMH12	0.93	1.07
WMH30	1.04	0.84
Average	0.97	1.01
COV	7.40%	9.90%

Table 2.3: Comparison of experimental and theoretical peak deflections

Wall Number	Experimental Deflection (mm)	Experimental Rotation (degrees)	Theoretical Deflection (mm)	Theoretical Rotation (degrees)	Percent Error
WML6	15.55	1.78	17.30	1.99	11%
WML12	36.99	4.24	28.80	3.30	-22%
WML30	FRACTURE	N/A	56.83	6.49	N/A
WMH6	14.57	1.67	13.62	1.56	-7%
WMH12	18.05	2.07	27.02	3.10	50%
WMH30	50.82	5.81	53.33	6.09	5%

Table 2.4: Level of protection provided by structural walls

Wall Number	Experimental Damage State	Experimental LOP	Theoretical Damage State	Theoretical LOP
WML6	Moderate	Low	Moderate	Low
WML12	Heavy	Very Low	Heavy	Very Low
WML30	Blowout	None	Heavy	Very Low
WMH6	Superficial	High	Moderate	Low
WMH12	Moderate	Low	Heavy	Very Low
WMH30	Heavy	Very Low	Heavy	Very Low

## CHAPTER 3 - DYNAMIC ANALYSIS OF ONE-WAY REINFORCED CONCRETE BLOCK FLEXURAL WALLS

### 3.1 ABSTRACT

In this study, an advanced single degree of freedom (SDOF) model is used to quantify the mid-span deflection of reinforced masonry flexural walls (RMFWs) that accounts for nonlinear behavior of the constituent materials, with particular attention to strain rate effects. Additionally, pressure-impulse ( $P-I$ ) diagrams are developed to assess the level of protection provided by the flexural walls. It is shown that the proposed SDOF model provides a reasonably accurate approximation of the overall structural response and values for the fundamental period of vibration. The  $P-I$  diagrams indicate that flexural walls similar to those investigated in this study can provide adequate levels of protection for low magnitude blast loads (low design basis threats, DBT); however, for blast loads characterized by high peak pressure and specific impulse (high DBT), specific detailing and strengthening methods (post-installed anchors, CFRP, etc.) should be undertaken to ensure that the flexural walls are capable of withstanding such specified loads without significant loss of load bearing capacity.

**KEYWORDS:** nonlinear SDOF model, blast load, strain rate, pressure-impulse

### 3.2 INTRODUCTION

Traditionally, masonry flexural walls have been designed for loading situations arising from wind pressures or out-of-plane seismic action. This wall type has rarely been detailed for extreme out-of-plane loading conditions. The ability of masonry flexural walls to withstand severe blast loads while preventing progressive collapse is a topic that has not been previously covered under the design codes in Canada. With the recent publication of the CSA S850-12

(CSA, 2012) and the ASCE 59-11 (ASCE, 2011), the blast protection of buildings and the occupants' safety are placed at the forefront. However, both standards are still in the early stages of their development and thus require further refinements in order to address the problem of blast resistant design.

Urgessa and Maji (2010) and Abou-Zeid et al. (2010) demonstrated the blast resistance of flexural concrete block walls when specific response mechanisms are engaged (e.g. arching). Additionally, when hardening approaches are undertaken, a considerable increase in flexural resistance can be achieved (Urgessa and Maji, 2010). However, these studies did not focus on structural components constructed by using standard techniques, such as grouting and reinforcement by plain steel bars.

The study by Baylot et al. (2005) demonstrated the resistance of masonry flexural panels with several levels of reinforcement ratios and grouting, and their investigation focused on the velocity response of the test specimens rather than deflections. The experimental setup developed by Baylot et al. directly inspired the setup described in Section 2.3.2 for the purpose of the current study.

Experimental work was also performed by Razaqpur et al. (2007) on GFRP strengthened reinforced concrete panels, which had dimensions and strengths comparable to the specimens described herein; although the latter study did not include dynamic analysis, it was instrumental in selecting the scaled distances necessary to achieve a significant level of damage to the specimens investigated in the current study.

Finally, a nonlinear dynamic analysis by Campidelli et al. (2013) was performed on reinforced concrete beam-columns subjected to blast overpressure and axial load simulated by external pre-stressing tendons. In the following discussion, the model developed for the dynamic

analysis of the test specimens is adapted from Campidelli et al. (2013), which originally accounted for P-Delta effects in axially loaded members (Timoshenko and Gere, 2009).

The aim of this paper is to develop practical and simple tools for the design and assessment of reinforced masonry flexural walls (RMFWs) when extreme out-of-plane loading is applied. This goal is achieved via the use of a single degree of freedom model, which accounts for strain rate effects, and the development of strain rate dependent pressure-impulse ( $P-I$ ) diagrams.  $P-I$  diagrams are generally viewed as a simple tool for the preliminary design of blast loaded structures, and in the following discussion they are employed to determine whether the analyzed masonry walls meet minimum design requirements (i.e. levels of protection) established by modern safety standards. The single degree of freedom model used in this study was developed by Campidelli et al. (2013), and has been adapted to account for the properties of fully grouted masonry assemblages.

### **3.3 SUMMARY OF EXPERIMENTAL PROGRAM**

This section includes a brief summary of the experimental program carried out in support of the current study; a more comprehensive description of the test setup, specimens, instrumentation, and material properties can be found in Section 2.3.1. The test specimens discussed in the following sections are part of a larger testing program. The stand-off distance was held constant at 5 m for all tests, while the charge weight ranged from a minimum of 5 kg to a maximum of 25 kg of Pentex D – 454 cast boosters (Orica, 2013), which feature an equivalent TNT–mass factor ranging from 1.0 to 1.5 (Dusenberry 2010). To simplify the calculations, in the following analysis a TNT–mass factor equal to 1.2 is consistently assumed as a generally well accepted first approximation (CERL, 2013).

The test specimens included six third-scale fully grouted concrete block walls organized in two groups, featuring with varying longitudinal reinforcement. *Group I* walls were reinforced with 15 longitudinal D4 steel bars (area = 26 mm<sup>2</sup>) and 15 W1.7 horizontal ties; these walls are given the designation WML (masonry walls with Low reinforcement ratio). *Group II* walls were reinforced with 15 longitudinal D7 reinforcing bars and 15 W1.7 horizontal ties; given the High reinforcement ratio, these walls are designated as WMH. In addition, to indicate the explosive charge (in kg of TNT) each specimen was exposed to, a number is added at the end of each designation. For instance, WMH6 denotes the wall in *Group II* (High reinforcement ratio) exposed to an explosive charge equivalent to 6 kg of TNT. Similarly, WMH12 represents a wall in *Group II* exposed to the overpressure resulting from 12 kg of TNT.

The test setup described in Section 2.3 was used to provide simply supported boundary conditions and house the instrumentation used to record the displacement and pressure histories. Three pressure transducers (models ICP 113A21 (PCB, 1997) and Pizotron 211B2 (Kistler, 2012)) were installed on the exterior of the reaction frame to measure the reflected pressure, while one transducer was placed inside the test cubicle to measure the internal pressure. Three displacement potentiometers (DPs), Penny+Giles model SLS190-300 (Penny+Giles 2012), were mounted inside the frame to measure the wall deflections at the mid-height and three quarter height. The data was recorded and sampled with a time interval of one microsecond.

### 3.3.1 MATERIAL MODELS

The stress-strain relationship of the masonry in compression, obtained from standard prism tests, was modeled by using the Thorenfeldt material model (Collins and Mitchell, 2001),

$$\frac{f_{mc}}{f'_{mc}} = \frac{n \left( \frac{\varepsilon_{mc}}{\varepsilon'_{mc}} \right)}{\left( n-1 + \frac{\varepsilon_{mc}}{\varepsilon'_{mc}} \right)^{nk}} \quad (3.1)$$

wherein  $f_{mc}$  is the compressive stress, in MPa, of the masonry prism corresponding to the strain  $\varepsilon_{mc}$ ,  $f'_{mc}$  is the average peak compressive strength at the strain of  $\varepsilon'_{mc}$ , and both  $n$  and  $k$  are fitting parameters obtained from curve fitting of the test data. When adapting the same model for the tensile strength of the prism assembly, Eq. (3.1) is modified by replacing the compressive strength with the modulus of rupture:

$$\frac{f_{mt}}{f'_{mt}} = \frac{n \left( \frac{\varepsilon_{mt}}{\varepsilon'_{mt}} \right)}{\left( n-1 + \frac{\varepsilon_{mt}}{\varepsilon'_{mt}} \right)^{nk}} \quad (3.2)$$

where  $f'_{mt}$  is the modulus of rupture, which, as recommended by Park and Pauley (1975) for concrete, is taken as  $0.62\sqrt{f'_{mc}}$  at the strain  $\varepsilon'_{mt}$ . Furthermore, as no data concerning the tensile strength of the masonry prisms are available, it is assumed that both the secant modulus at peak stress and the factor  $n$  are the same as those obtained from compression tests, acting similar to concrete. Therefore, the strain  $\varepsilon'_{mt}$  is calculated by dividing the modulus of rupture by the secant elastic modulus.

The stress-strain relationship for the steel reinforcement was obtained from tensile tests and was approximated by a bilinear function with the elastic limit occurring at the average yield strength and yield strain. For detailed information concerning the materials properties, the reader is referred to Section 2.3.1.

### 3.4 **LOAD-DEFORMATION ANALYSIS**

To predict the response of a flexural wall under blast loading, its resistance function, which describes the wall resistance to static loading, needs to be determined (USDOD, 2008). This resistance function will be calculated using three different approximations, namely, a linear elastic model, a bilinear (elastic-plastic) model, and a nonlinear model. The development of the resistance function is a two step process:

- Development of the moment-curvature relationship
- Load-deflection analysis

In the following sections, the moment-curvature relationship and the corresponding load-deflection analysis are obtained for each wall group.

#### 3.4.1 ***MOMENT-CURVATURE ANALYSIS***

The moment-curvature relationship is obtained by discretizing the cross-section into several layers (fibres) of constant depth and parallel to the cross-section width. Next, a curvature value is assumed and strain compatibility is applied to determine the strain at each layer; the resulting stress distribution is subsequently calculated from the stress-strain relationship. Using the stress distribution, the depth of the neutral axis is determined by trial and error. Finally, the moment resistance associated with the assumed curvature value is found by integrating the product of the layer average stress and the lever arm with respect to the neutral axis position from each individual layer. This procedure is repeated for several curvature values and is based on the material stress-strain relationships reported in Section 2.3.1.

The typical moment-curvature diagram generated by the model in this study is shown in Figure 3.2 with several transition points displayed on it. The first transition point corresponds to

the attainment of the concrete tensile strength at the extreme tension fibre. After this point, the moment of inertia begins to transition from value associated with the gross section to the value associated with the cracked section. The second transition point marks the yielding of the steel reinforcement, which, given the aspect ratio of the cross-section, generally occurs around the peak moment resistance, and it is followed by a gradual decrease in the moment resistance until failure. The final transition point shown in Figure 3.2 marks the failure of concrete in compression, when the section begins to crush and there is little residual resistance in the section.

Figure 3.3 shows the comparison between the moment-curvature diagrams generated for the two groups of test specimens. Both groups provided the same rate of increase of the moment resistance before first cracking. The specimens in *Group II* feature the highest reinforcement ratio as well as the highest moment resistance.

It is noted that the walls in *Group II* exhibit lack of ductility at the cross-sectional level, as yielding of the steel reinforcement is approximately concurrent with the peak moment resistance, as shown in Figure 2. Following the development of the moment-curvature diagrams, the curvature ductility,  $\mu_\phi$ , is calculated as shown in Eq.(3.3)

$$\mu_\phi = \frac{\phi_u}{\phi_y} \quad (3.3)$$

where  $\phi_u$  is the curvature at the ultimate condition, and  $\phi_y$  is the yield curvature.

Figure 3.3 shows a moderate amount of ductility associated with the walls in *Group I*, which is confirmed by the calculated curvature ductility ratio, equal to  $\mu_\phi = 1.21$ . The moment-curvature diagram for the *Group I* walls initially increases with a rate associated with the gross moment of inertia. Following the local peak and valley, the moment resistance of the section increases at a decreasing rate that is associated with the cracked moment of inertia until the

section reaches the peak moment resistance. Upon reaching this peak, the moment resistance decreases at an increasing rate as the curvature of the section increases. The local peak noted occurs as the concrete of the masonry blocks begins to fail in tension at the extreme fibre. The global peak of the moment-curvature diagram corresponds to the yielding of the steel reinforcement, undergoing strain hardening. The decreasing of the moment-curvature diagram corresponds to the increase of strain hardening of steel, and eventually the compressive failure of the concrete. While the ductility ratio does not affect the peak response of the specimens, their overall response is significantly affected by it. To further examine the status of the specimen reinforcement, calculations to determine the  $c/d$  ratio were performed according to CSA S304.1 (2004) to determine whether the reinforcement ratio was above or below that of the balanced condition. The  $c/d$  ratio calculated for this wall group was found to be 0.42, compared to the balanced condition of 0.59, showing the under-reinforcement of the section.

Finally, *Group II* walls feature  $\mu_\phi = 0.61$  and  $c/d = 0.73 > 0.59$ , which qualifies them as over-reinforced

### 3.4.2 FORCE-DISPLACEMENT ANALYSIS

The relationship between moment and curvature is the basis for developing the load-deflection curve, which is determined by integrating the curvature produced by the given load distribution. The deflection curve  $\Delta(x)$  is calculated by numerical integration of the following equation by Campidelli et al. (2013) for simply supported boundary conditions:

$$\Delta(x) = \int_0^x \left( \int_0^s \kappa(r) dr \right) ds - \frac{x}{L} \int_0^L \left( \int_0^s \kappa(r) dr \right) ds \quad (3.4)$$

where  $\kappa$  is the curvature of the wall,  $x$  is the distance from the support along the wall span, and  $L$  is the span length.

A comparison of resistance functions from the bilinear and nonlinear models is shown in Figure 3.4. The bilinear model is defined by the stiffness,  $K$ , and the peak resistance,  $R_{\max}$ . The peak resistance is defined as (Biggs, 1964)

$$R_{\max} = \frac{8M_{\max}}{L} \quad (3.5)$$

where  $M_{\max}$  is the peak moment resistance, and  $L$  is the span of the specimen. The stiffness is defined as (Biggs, 1964)

$$K = \frac{384}{5} \frac{EI_{av}}{L^3} \quad (3.6)$$

where, for mere convenience,  $E$  is assumed to be the concrete tangent modulus at zero strain, and  $I_{av}$  is the moment of inertia. The bilinear model assumes the average weighted moment of inertia given in Eq.(3.7)

$$I_{av} = 0.75I_{cr} + 0.25I_g \quad (3.7)$$

which provides an estimate of the wall deflection less biased than the arithmetic mean recommended by ASCE (2008). The elastic limit  $\Delta_e$  in the bilinear model is calculated as  $\Delta_e = R_{\max} / K_{av}$ , and for displacements  $\Delta \geq \Delta_e$  a constant resistance is assumed.

The maximum resistance defined in Eq (3.5) is also assumed in the nonlinear model. However, in this model the stiffness is governed by the inertia of the gross section until the modulus of rupture is attained; afterwards a tension stiffening model is assumed, which captures the gradual transition to a fully cracked cross-section. It is noted that the peak resistance attained by the specimens occurs at a curvature approximately equal to the point at which the steel reinforcement yields. This shows an overall lack of ductility across the wall specimens. On the other hand, the test data show a flexural behavior characterized by significant ductility, which

points to a shortcoming in the adopted model. To correct for the variance noted, the nonlinear model assumes a constant resistance after its peak is attained, as shown in Figure 3.4

### 3.4.3 DEFORMED SHAPE

The deformed shape of the member is evaluated by normalizing the deflection curve by its peak value. For simply supported boundary conditions and uniformly distributed load, the peak deflection occurs at mid-span. For a bilinear model, the deformed shape  $\varphi(x)$  adopted in the elastic range is given in Biggs (1964) as that in Eq.(3.8):

$$\varphi(x) = \frac{16}{5L^2} (xL^3 - 2Lx^3 + x^4), \quad 0 \leq x \leq L \quad (3.8)$$

When the specimen enters the plastic range, which is associated with the plateau of the resistance function, the deformed shape is assumed to be a bilinear symmetric function (Biggs, 1964):

$$\varphi(x) = \begin{cases} \frac{2x}{L} & 0 \leq x \leq \frac{L}{2} \\ 1 - \frac{2x}{L} & \frac{L}{2} \leq x \leq L \end{cases} \quad (3.9)$$

The nonlinear model is able to capture the gradual transition from an elastic system, as described by Eq.(3.8), to a system experiencing an increasing level of damage (e.g. concrete cracking, reinforcement yielding, and concrete crushing). In the limit, the deformed shape of the member approaches the function described by Eq.(3.9). For the *Group I* walls, the evolution of the deformed shape is shown in Figure 3.1.

### **3.4.4 EXPERIMENTAL STATIC TESTING**

As outlined in Section 2.3, one specimen from each group was tested under static conditions to measure the maximum resistance. Table 3.1 shows a comparison between measured and peak resistance. With the testing of the *Group I* wall, the test results obtained were skewed due to technical difficulties encountered during the testing. As such, the experimental results from this test are removed from this study. The peak resistance of *Group II* test wall measured 60.9 kN, which is in reasonable agreement with the theoretical value of 53.3 kN as an error of 14.3% is noted.

## **3.5 DYNAMIC ANALYSIS**

### **3.5.1 SINGLE DEGREE OF FREEDOM MODEL**

A large body of knowledge (e.g. Baker et al., 1983; Biggs, 1964; Smith and Hetherington, 1994; USDOD, 2008) has extensively documented the use of single degree of freedom models (SDOFs) to determine the dynamic response of a structural member in terms of a single parameter, e.g. the displacement of its mid-span. While this analysis, in its most widely subscribed forms, has clear limitations, such as the complete disregard for higher modes of vibrations and the inability to model structural systems with multiple structural components, the simplicity of its implementation makes it an ideal tool for end-users not well versed with dynamic modeling. Another advantage of SDOF modeling is the modest computational effort that it requires.

In order to implement an SDOF model, a number of properties of the actual structural member must be determined, including the type of failure the member is likely to experience, the applied loading history and distribution, and the corresponding deformed shape. In particular, the

selection of the proper deformed shape leads to the proper transformation factors to be used for dynamic analysis. For a fully nonlinear resistance function, the transformation factors associated with the test specimens are presented in Section 3.5.5. For a bilinear resistance function, the associated transformation factors are well known from the literature (Baker et al., 1983; Biggs, 1964; Smith and Hetherington, 1994) and are typically based on the deformed shape of a member under static, uniformly distributed load or associated with the fundamental mode of vibration. As pointed out by Biggs (1964), the selection of the deformed shape has negligible effect on the deflection history. However, owing to the dismissal of higher modes of vibration, both the bending moment and shear distributions are usually poorly predicted (Biggs, 1964).

The motion of an SDOF system is described by the following equation:

$$K_{LM}m'\ddot{\Delta}(t) + R(\Delta(t)) = F(t) \quad (3.10)$$

where  $m'$  is the mass of the actual member,  $R$  is its resistance function,  $K_{LM}$  is the load-mass transformation factor,  $\ddot{\Delta}(t)$  is the acceleration,  $\Delta(t)$  is the displacement at the time  $t$ , and  $F(t)$  is the forcing function resulting from the blast overpressure and the specimen tributary area. A suitable way of solving Eq.(3.10) is by local piecewise linear representation of the resistance and forcing functions found in Campidelli et al. (2013).

Substituting the local values for the resistance and forcing functions in the equation of motion, a local representation of the equation motion is obtained:

$$K_{LM}m'\ddot{\Delta} + R_{0,i} + k_i(\Delta - \Delta_{0,i}) = F_{0,i} + F_{1,i}(t - t_i) \quad (3.11)$$

which allows for a simple closed form solution in terms of the displacement  $\Delta$ . For all positive values of  $k$  the solution to Eq. (3.11) is given as (Campidelli et al., 2013)

$$\Delta(t) = \Delta_{0,i} + \frac{F_{0,i} - R_{0,i}}{k_i} + \frac{F_{1,i}}{k_i}(t - t_i) - \frac{F_{0,i} - R_{0,i}}{k_i} \cos[\omega(t - t_i)] + \frac{1}{\omega} \left( \dot{\Delta}_{0,i} - \frac{F_{1,i}}{k_i} \right) \sin[\omega(t - t_i)] \quad (3.12)$$

wherein  $\dot{\Delta}_{0,i}$  is the initial velocity of the specimen and  $\omega_i$  is the  $i$ -th circular frequency defined as

$\omega_i = \sqrt{k_i / K_{LM,i} m'}$ . When the stiffness  $k$  is equal to zero, the displacement function is given by

Eq.(3.13) instead (Campidelli et al, 2013):

$$\Delta(t) = \Delta_{0,i} + \Delta_{0,i}(t - t_i) + \frac{F_{0,i} - R_{0,i}}{2K_{LM,i} m'} (t - t_{0,i})^2 + \frac{F_{1,i}}{2K_{LM,i} m'} (t - t_i)^3 \quad (3.13).$$

### 3.5.2 STRAIN RATE DEPENDANT CONSTITUTIVE LAWS FOR MATERIALS

A number of studies have been performed on the response of materials when subjected to loading causing high rates of strain. In this study, the focus is limited to the problem of finding the so-called dynamic increase factor (DIF), defined as the dynamic to static strength ratio for the given material under uniaxial state of stress. Studies addressing this phenomenon include Malvar and Ross (1998), Malvar (1998), and CEB (1990). On this basis, the behavior of the masonry prisms is modeled as that of a reinforced concrete member, in accordance with the following assumptions:

- The initial tangent modulus of elasticity (elastic modulus at zero strain) remains constant regardless of the rate of strain. This is considered to be a reasonable approximation, and is supported by several strain rate dependant models including those proposed by Ngo et al. (2003) for concrete in compression, which shows a negligible change in the initial tangent modulus for the relatively small rates of strain calculated in the current study, i.e. strain rates generally not greater than  $10 \text{ s}^{-1}$ .

- The strain at peak stress is increased by the same DIF used to enhance the material strength; as a consequence, the secant modulus at peak stress is also unaffected by the rate of strain.
- The DIF formulation adopted for concrete in compression is from the Comité Euro-International du Béton (CEB, 1990), while the DIF for concrete in tension is from Malvar and Ross (1998).
- The factor  $n$  (see Eq. (3.1)) for the prisms in compression is determined from curve fitting of the test data; as no tests were performed on the prisms in tension, the same value for  $n$  (see Eq.(3.2)) is assumed for the tensile behavior of the prisms.
- For the steel reinforcement, the DIF formulation by Malvar (1998) is adopted.

### 3.5.3 STRAIN RATE DEPENDENT RESISTANCE FUNCTIONS

Given the effect of the strain rate on the specimen material properties, modified moment-curvature diagrams and resistance functions were developed. The methodology followed to obtain these functions consists in assuming a single average value of the curvature rate for each blast scenario. This average value is calculated via trial and error procedure, by finding the actual variation of the curvature rate in time and along the specimen span and then matching the resulting average with the value assumed at the beginning of each SDOF analysis run. Once an adequate average curvature rate is established, the strain rate distribution is found throughout the member; then, the stress distribution is determined on the basis of the assumed stress-strain-strain rate models described earlier; finally, the moment-curvature diagram and resistance function are recalculated by integrating the new stress distribution.

Figure 3.7(a) shows the effect of the rate of strain on the bilinear resistance function of specimen WML12. As the figure shows, the stiffness of the system does not change with the

increase in the strain rate, as both the displacement at the elastic limit and the peak resistance increase by the same factor. The strain rate dependent nonlinear resistance function associated with the same specimen is depicted in Figure 3.7(b). The cracking moment experiences a 130% increase, while the displacement range between the first and second transition points shortens and the peak resistance of the nonlinear curve occurs at a smaller displacement.

Figure 3.8 displays the difference, in terms of resistance function, between the two models used throughout this study (bilinear and nonlinear) and the model assumed by the software SBEDS (USACE, 2008). For this study, SBEDS was used to calculate the response of a system which features a bilinear resistance function whose elastic stiffness is based on the average cross-sectional moment of inertia, as recommended by USDOD (2008). Moreover, strain rate effects are accounted for in SBEDS by assuming fixed values of the DIFs, which in this case have been chosen in accordance with the values recommended in ASCE (2011). It is noted that SBEDS predicts the lowest estimate for the peak resistance, which may be ascribed to the well known conservatism of the adopted DIFs. Also, the stiffness associated with the nonlinear model is closely approximated by SBEDS up to SBEDS' elastic limit. Beyond this limit value the SBEDS estimated values of stiffness and resistance are found to be lower.

#### **3.5.4 THEORETICAL PRESSURE PROFILE**

Two methods are commonly used to represent the pressure profile generated by the detonation of explosives, provided that the blast wavefront parameters are known. The first method, usually suited for design purposes, consists in assuming a linearly decaying pressure history, as first proposed by Baker (1973).

To provide a more accurate representation, the modified Friedlander equation was proposed by Baker et al. (1983). The modified Friedlander equation was developed to better

describe the positive pressure phase, i.e. the time during which the blast pressure exceeds the atmospheric pressure, by accounting for the exponential rate of decay of the overpressure at the shock wavefront via the introduction of a decay coefficient  $\gamma$ . Three key wavefront parameters are used in this equation to fully describe the positive pressure phase, namely, the peak positive pressure,  $P_{\max}$ , the positive phase duration,  $t_d$ , and the decay coefficient,  $\gamma$ . From these three parameters another key metric, the positive specific impulse,  $I$ , can be extracted. The last parameter is determined from the other three as the area delimited by the pressure-time function, the pressure baseline (the ambient pressure), and the times  $t_a$  and  $t_a + t_d$ , where  $t_a$  denotes the time of arrival of the shock wavefront.

### 3.5.5 LOAD-MASS TRANSFORMATION FACTORS

The conversion of an actual structural member into an equivalent SDOF system is achieved by using the so-called transformation factors, which are generated by equating the kinetic energy of the two systems as well as the work done by the applied load (Biggs 1964).

For a simply supported boundary conditions and uniformly distributed load, the principle of kinetic energy equivalency leads to the mass factor in Eq. (3.14)

$$K_M = \frac{1}{L} \int \phi^2(x) dx \quad (3.14)$$

Similarly, the load factor is obtained by equating the work done in the two systems. The result is given in Eq.(3.15).

$$K_L = \frac{1}{L} \int \phi(x) dx \quad (3.15)$$

It is also convenient to define a load-mass factor as the ratio  $K_{LM} = K_M / K_L$ , which is utilized in the equation of motion for the system. For the bilinear model, the  $K_{LM}$  values calculated by

Biggs (1964) are adopted, i.e.  $K_{LM} = 0.78$  in the elastic range and  $K_{LM} = 0.66$  in the plastic range, as shown in Figure 3.9. Conversely, in the nonlinear model the  $K_{LM}$  factor is a continuous function of the displacement, obtained by numerical integration of the deformed shape. However, after the peak resistance is attained, the nonlinear model does not yield predictions concerning the flexural behavior of the member. Therefore, the assumption is made of a sudden decrease of  $K_{LM}$  to its lower bound (0.66), as shown in Figure 3.9.

### 3.5.6 RESULTS FROM DYNAMIC ANALYSIS

#### 3.5.6.1 DYNAMIC REACTIONS

It is of interest to determine the dynamic reactions  $V_0$  generated by the specimens because flexural panels similar to the ones tested are often connected to or supported by members whose overall design is dependent on the value of  $V_0$ . To determine these reactions, the equilibrium of the section under dynamic loading must be considered, which takes into account the inertia force,  $IF(t)$ , calculated on the basis of the deformed shape of the specimen. The result of the integration process is shown in Eq. (3.16)

$$IF(t) = m' L K_L \ddot{\Delta}(t) \quad (3.16)$$

in which  $m'$  indicates the mass per unit length. The dynamic reaction of the specimen is determined by the nonlinear model as follows

$$V_0(t) = \frac{F(t) - IF(t)}{2} \quad (3.17)$$

and by combining Eqs. (3.16) and (3.17), the dynamic reaction becomes

$$V_0(t) = \frac{F(t) - m' K_L \ddot{\Delta}(t)}{2} \quad (3.18)$$

Figure 3.10 shows a comparison between dynamic reaction histories obtained from the bilinear model, the nonlinear model, and SBEDS. It can be observed that the SBED model predicts the highest peak reaction value. A summary of the peak dynamic reactions is also included in Table 3.2.

### **3.6 EXPERIMENTAL DATA VERSUS THEORETICAL PREDICTIONS**

#### ***3.6.1 BLAST WAVEFRONT PARAMETERS AND PRESSURE PROFILES***

The peak pressure, positive phase duration, and decay coefficient are extracted from the measured pressure histories by fitting the modified Friedlander curve to the pressure data. After establishing these three parameters, the positive impulse is determined from the area delimited by the pressure profile.

The peak pressure and specific impulse predicted by the Kingery and Bulmash (1984) model (K-B model) are compared in Table 3.3 with the experimental values measured during the blast testing. The error (*err*) in the predictions, in percentage points, is calculated as

$$err = \left( 1 - \frac{X_{test}}{X_{model}} \right) \cdot 100 \quad (3.19)$$

in which *X* may indicate any of the parameters investigated in this study (e.g. peak pressure, specific impulse, etc.). As shown in Table 3.3, provides a reasonably close estimate of the wavefront parameters: for instance, the error associated with the peak pressure ranges from a minimum of -32.5% to a maximum of -14.6%. This model also leads to an average error (bias) of -21.4% and an associated standard deviation of 6.8%, which shows a significant systematic error component but a relatively small random error (small scatter). Conversely, for the specific impulse, the error ranges from a minimum of -3.3% to a maximum of 26.9%. In this case the

data shows a smaller bias equal to 7.9%, but a standard deviation as high as 16.4%, caused by larger scatter in the data points

In summary, Table 3.3 demonstrates that peak pressure is often underestimated by the K-B model while the specific impulse is often overestimated. It is noted that accurate and reliable measurement of the blast overpressure can be quite challenging. There are additional challenges associated with the interpretation of the data, which may be caused by or related to the presence of multiple candidates for the baseline, which indicates the ambient pressure, as well as the type of fitting methodology employed. Lastly, difficulties may arise from the lack of objective criteria for the rejection of corrupted pressure data.

### **3.6.2 DISPLACEMENT HISTORIES**

Table 3.4 shows the experimental results and theoretical predictions obtained for the peak displacement of each wall. It is noted that wall WML30 suffered catastrophic failure manifested by fracture of the specimen body in two halves, therefore the associated peak displacement, as measured by the DPs, is not regarded as a meaningful value. With the exception of two outliers (walls WMH12, WMH30), the cross examination of the test data versus model predictions support the conclusion that amongst the three SDOF models the nonlinear model provides the best agreements with the measurements. For low charge weights, the linear model provides reasonably accurate predictions for the peak response, as shown in Figure 3.11 and Table 3.4: the error, calculated from the test/model displacement ratio as  $(1 - \text{test}/\text{model})$ , is quantified in the measures of -9.1% for wall WMH6. As expected, the linear model performs poorly in the case of large charge weights (12 and 30 kg), as shown in Figure 3.11 for wall WML30; for these scenarios, the error is found ranging from -55.5% to 13.4%. The estimates for walls WMH12 and WMH30 from the bilinear and nonlinear models deviate significantly from the experimental

results (bilinear model error = 41.4% and 53.7% for walls WMH12 and WMH30, respectively, and nonlinear model error = 43.9% and 53.4%, respectively), which may be ascribed either to inaccurate field measurements or to the inability of the two models to account for the material behavior. The linear model for these two walls provides a better estimate due to the lack of overall damage experienced during the testing, which lead to a value for stiffness more closely associated to that of the gross moment of inertia as compared to the value associated with the cracked moment of inertia.

As far as the displacement values generated by SBEDS are concerned, it is observed that only one prediction is associated with an error not greater than 15%; furthermore, the model consistently overestimated the peak displacement of all walls, with the exception of specimen WMH6, and SBEDS generated displacement histories were observed to be similar to those obtained from the bilinear model. The similarities between the results of two models are the result of the same bilinear shape of the assumed resistance function, while the discrepancies are due to different DIFs and elastic stiffness values adopted in the calculations.

### **3.7 PRESSURE-IMPULSE DIAGRAMS**

#### ***3.7.1 DEVELOPMENT OF PRESSURE-IMPULSE DIAGRAMS***

A detailed recapitulation of pressure-impulse ( $P-I$ ) diagrams (or iso-damage curves) can be found in Section 1.5.10, however the properties most salient to this study are discussed in the following section.

A  $P-I$  diagram is constructed by determining the combinations of pressure and impulse which would cause a structural element to attain a pre-determined response limit (Smith and Hetherington, 1994), and typically four response limits are selected to draw the  $P-I$  diagrams of

reinforced masonry walls (CSA, 2012). The lowest response limit is associated with the upper bound of the damage state designated as “Superficial Damage”. This limit is quantified by the ductility ratio  $\mu_{\Delta} = \Delta_u / \Delta_y = 1$ . The second response limit is associated with the upper bound of “Moderate Damage” and is characterized by a peak support rotation of 2 degrees as well as plastic deformation (past the elastic limit  $y_e$ ). The third response limit quantifies the upper bound of “Heavy Damage” and is set equal to a peak support rotation of 8 degrees. Finally, the last response limit is associated with the upper bound of “Hazardous Failure” and consists in a peak support rotation of 15 degrees. For walls exceeding the 15 degrees peak support rotation, “Blowout” is expected to occur. This damage state occurs when the blast load completely overwhelms the wall, with catastrophic consequences (CSA, 2012).

### 3.7.2 ASSESSMENT OF DAMAGE STATE

Given the response limits (ductility ratio and support rotation) associated with the iso-damage curves, by plotting in the  $P-I$  space the values of peak pressure and specific impulse reported in Table 3.3 the level of damage of each test specimen can be visually gauged. For the tests that did not produce clear pressure records, data from Smith et al. (2014) were adopted, as their experimental setup was nominally identical – in terms of charge mass, standoff distance, and angle of incidence – to the one described in this study. In the following discussion, the combinations of reflected pressure and impulse from Smith et al. (2014) are designated as “PN”, while those obtained by the author are labeled “PM”.

The  $P-I$  diagrams are developed by using three different methods. The diagrams in Figure 3.12 are obtained from the bilinear model used in this study and do not account for strain rate effects. The same model is used in Figure 3.13, but in this case strain rate effects are considered

by assuming an enhanced maximum resistance calculated on the basis of the average curvature rate estimated from the field test conditions. Lastly, in Figure 3.14, a nonlinear model is used, which estimates the average curvature rate and subsequent resistance enhancement for each pressure-impulse combination.

### 3.7.2.1 BILINEAR MODEL – NEGLECTED STRAIN RATE EFFECTS

Sample *P-I* diagrams generated by this model can be found in Figure 3.12(a) and (b), which represent the post-blast conditions of walls WML6 and WMH6. Both walls are classified as undergoing “Heavy Damage”, while leaning toward the “Moderate Damage” damage state. A summary of the damage states and levels of protections from this model by the walls in this study is shown in Table 3.5, while further investigation into the *P-I* diagrams obtained through this model can be found in Appendix A.

### 3.7.2.2 BILINEAR MODEL – STRAIN RATE EFFECTS INCLUDED

By applying the bilinear model while taking into account the strain rate effects, the *P-I* diagrams shown in Figure 3.13 are developed for test walls WML6 and WMH6. A summary of the damage states and levels of protection of the walls used in this study is found in Table 3.5 while the *P-I* diagrams for all walls obtained through this model are found in Appendix B. For specimen WML6, the *P-I* diagrams shown in Figure 3.13(a) indicate “Heavy Damage” state, leaning toward “Moderate Damage”. Based on the *P-I* diagrams associated with specimen WMH6 in Figure 3.13(b), this wall falls within the “Moderate Damage” category; however, the measured pressure and impulse values are close to the upper bound of this damage state, which marks the transition to “Heavy Damage”.

### 3.7.2.3 NONLINEAR MODEL

*P-I* diagrams for walls WML6 and WMH6 developed using the nonlinear model and accounting for strain rate effects are shown in Figure 3.14. A summary of the results obtained through the development of *P-I* diagrams for all walls is found in Table 3.5, while the *P-I* diagrams for all walls obtained by this model can be found in Appendix C.

Shown in Figure 3.14(a) is the *P-I* diagram for wall WML6. The combination of pressure-impulse from the K-B model indicates a damage assessment classified as “Moderate Damage”, with a strong tendency towards “Heavy Damage” state. This tendency is confirmed by the field measurements, which indicate “Heavy Damage” state, leaning toward moderate.

The *P-I* diagrams for wall WMH6, shown in Figure 3.14(b), suggest two potential classifications for the wall damage. On the basis of the K-B model, the wall should experience “Moderate Damage”. However, the experimental pressure profile indicates that the wall should suffer “Heavy Damage”.

### 3.7.2.4 COMPARISON BETWEEN MODELS

In general, from cross-comparison of *P-I* diagrams from different models it is observed that ignoring strain rate effects produces a noticeable downward and leftward shift of the iso-damage curves for a fixed response limit. This phenomenon can be ascribed to the enhanced strength of materials under high rates of strain, which produces an overall increased resistance function describing the wall dynamic behavior. In addition, it is observed that the damage states and corresponding levels of protection calculated for the test specimens on the basis of the *P-I* diagrams compare favourably to the values observed during the testing regime.

From the *P-I* diagrams shown, it is clear that ignoring strain rate effects result in an overestimation of the post-blast damage of several walls. For instance, walls WMH6, WMH12,

and WML6 are all expected to experience “Heavy Damage” when the rate of strain is not considered; yet, during the experimental program these walls suffered damage ranging from “Superficial” to “Moderate”. In addition, by ignoring the strain rate effect, wall WMH30 is expected to fall under the “Blowout” damage state, but “Heavy Damage” was inferred from the post-blast conditions.

Given the differences between the adopted SDOF models, it is concluded that strain rate effects can have significant impact on the structural response, while increasing the computational effort from bilinear to nonlinear does not significantly alter the predicted response. The asymptotes associated with the  $P-I$  diagrams generated by the bilinear model, not accounting for strain rate, are significantly higher than those predicted when accounting for the rate of strain. Further decrease in the predicted level of damage is noted when the nonlinear model is used. In the bilinear model neglecting the rate of strain, the onset of plastic deformation occurs when the support rotation attains 0.54, and 0.64 degrees for *Group I*, and *Group II*, respectively. When accounting for strain rate effects, the support rotation increases significantly, ranging from 0.72 to 0.75 degrees for *Group I*, and from 0.93 to 0.99 degrees for *Group II*; similar results are found when using the nonlinear model.

It is demonstrated in Figure 3.15(a) that there is relatively minor difference between the iso-damage curves of the different models at a lower response limit, as there is only a moderate shift toward the origin when the rate of strain is accounted for. This minor difference occurs because the combinations of pressure and impulse associated with this response limit do not induce significant strain rate effects in the specimens, as these combinations correspond to relatively high scaled-distance values. A drastic difference between iso-damage curves from different models can be appreciated in Figure 3.15(b), which is obtained for the highest response

limit and shows that the associated combinations of pressure and impulse induce very significant strain rate effects.

### 3.8 CONCLUSIONS

The effectiveness of modeling the dynamic behavior of two groups of reinforced masonry flexural walls (RMFWs) subjected to blast loading is investigated in this study. Three single degree of freedom (SDOF) models, generated from resistance functions, which take into account the geometric and material properties, are developed to analyze the effect of different design basis threats (DBTs) on the dynamic response of the specimens described in this study. The output from each model is compared to the values recorded during testing to validate the ability of the model to predict the expected peak displacement and behavior of the RMFWs. Following the model validation, pressure-impulse ( $P-I$ ) diagrams are generated to predict the damage limits achieved by the wall groups at each of the selected DBTs. Given the results presented in this study, the following recommendations are made:

- The recommendation by USDOD (2008) regarding the average moment of inertia may be replaced, for assessment purposes, with a weighted average given by using 25% of the gross section moment of inertia and 75% of the cracked moment of inertia, in order to predict deflections with a bilinear SDOF model. This indication, however, need be confirmed by theoretical and/or numerical investigations, before a general recommendation can be made.
- In strain-rate dependent models, the effect of the curvature rate governs the overall response of the wall in comparison to the effect of the rate of change of the neutral axis.

- The difference between *P-I* diagrams generated using a bilinear or nonlinear model is minor, as modest differences in the impulsive and pressure asymptotes are noted.
- Strain rate effects have significant impact on the determination of the iso–damage curves. When developing *P-I* diagrams, the effect of the strain rate on the structural response of the member should be accounted for.

From the comparison of the experimental and theoretical results, significant discrepancies are found in the displacement response of the masonry flexural panels, which underscores the difficulties of processing the data obtained from testing using live ordinances. In addition, while the software SBEDS is typically used to calculate the response of a structural member for design purposes, it is shown that SBEDS does not necessarily provide the most conservative estimates for the peak response. Therefore reasonable caution should be taken when using this program to determine the response of a structural member exposed to blast pressure.

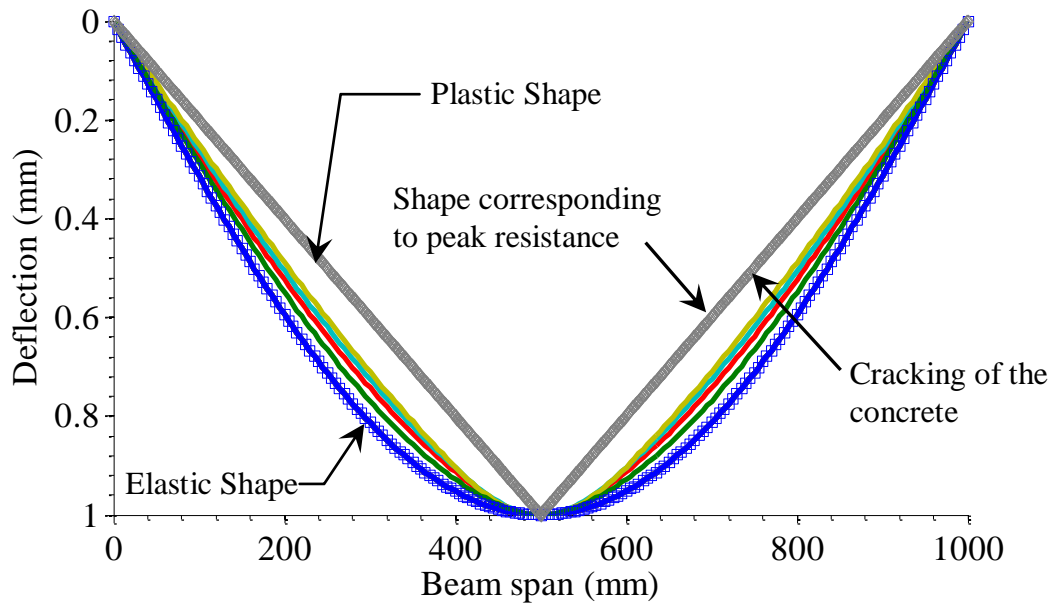


Figure 3.1: Typical evolution of the deformed shape (specimen WML12)

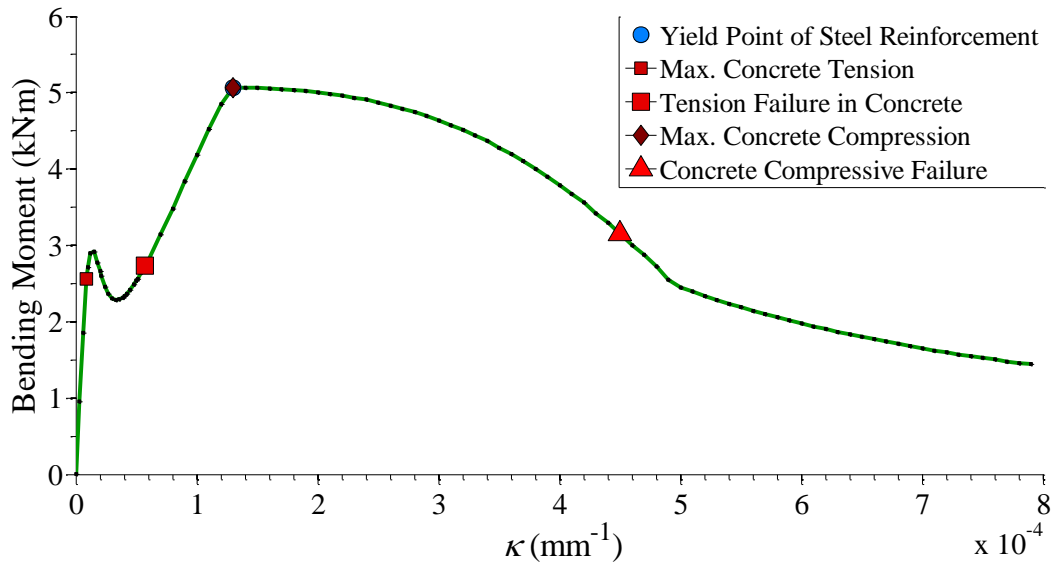


Figure 3.2: Moment-curvature diagram (Group I wall)

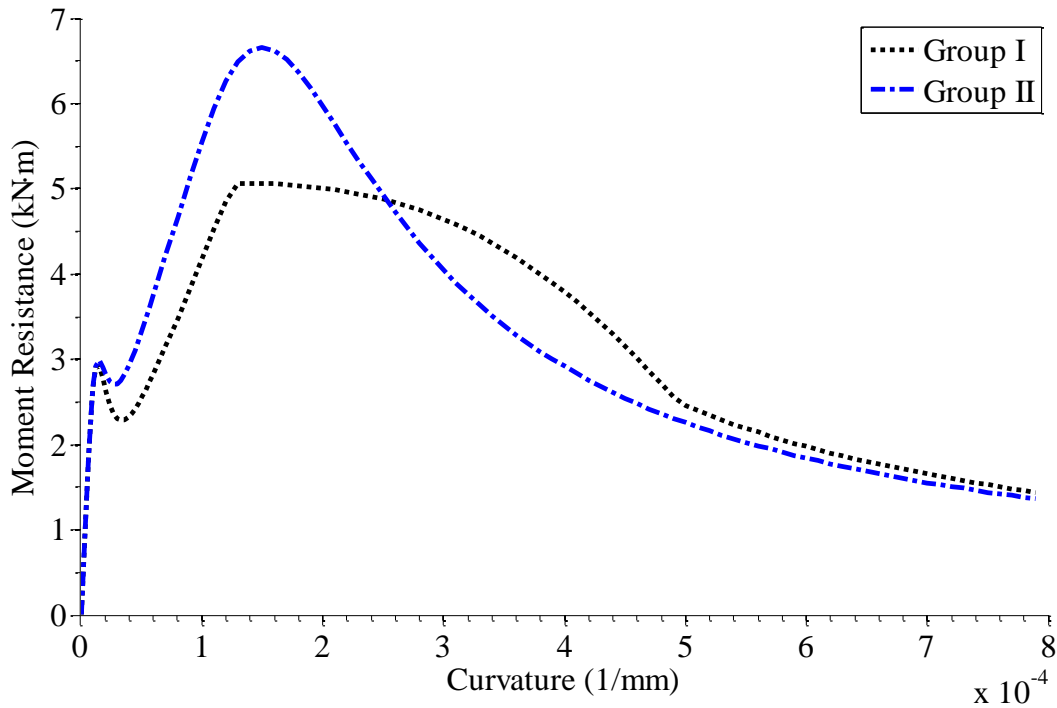


Figure 3.3: Comparison between moment-curvature diagrams associated with different wall groups

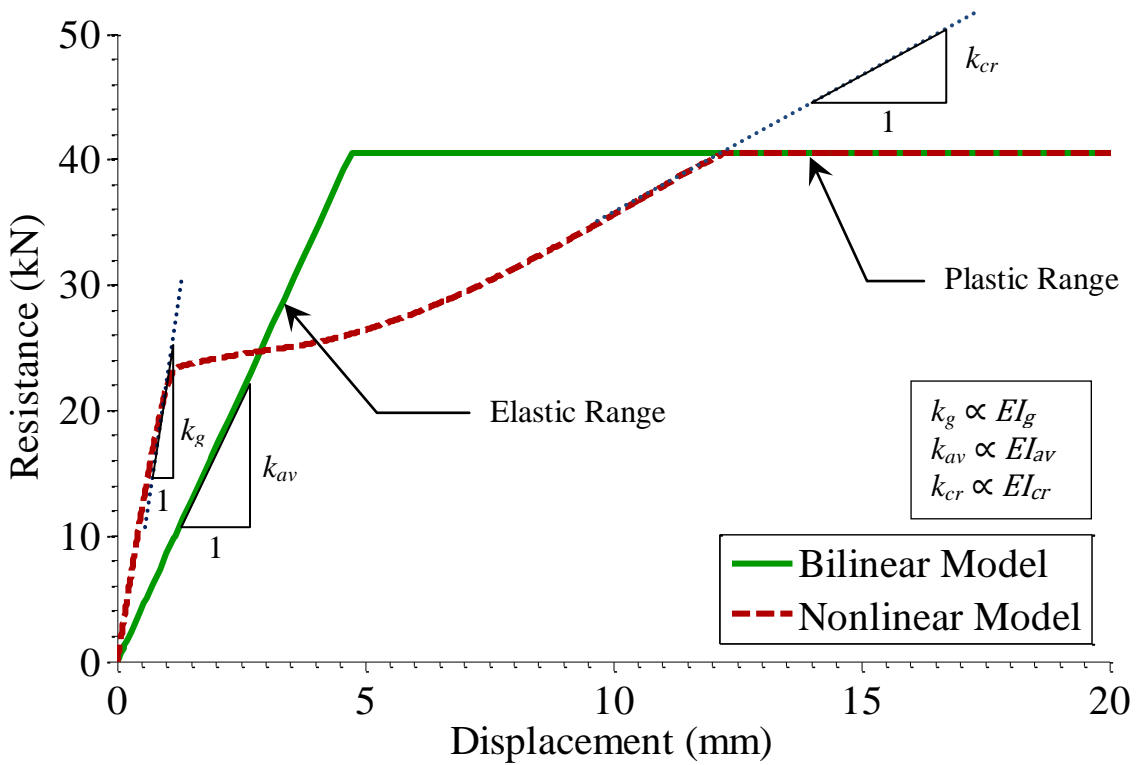


Figure 3.4: Bilinear vs. nonlinear resistance function (Group I walls)

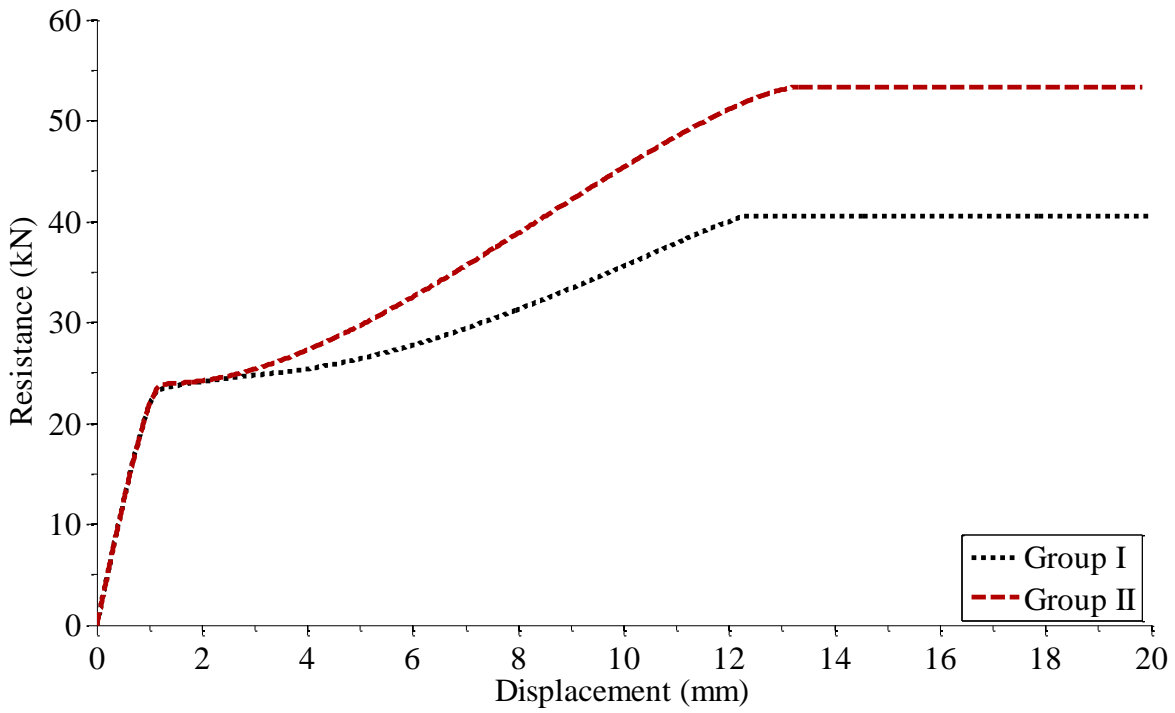


Figure 3.5: Comparison of resistance functions

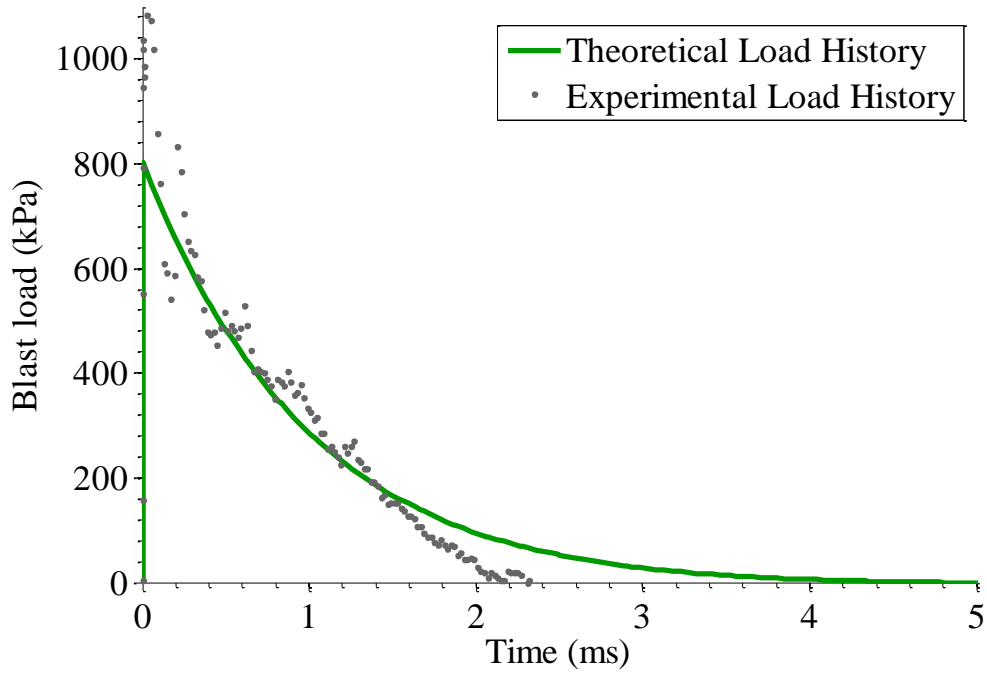
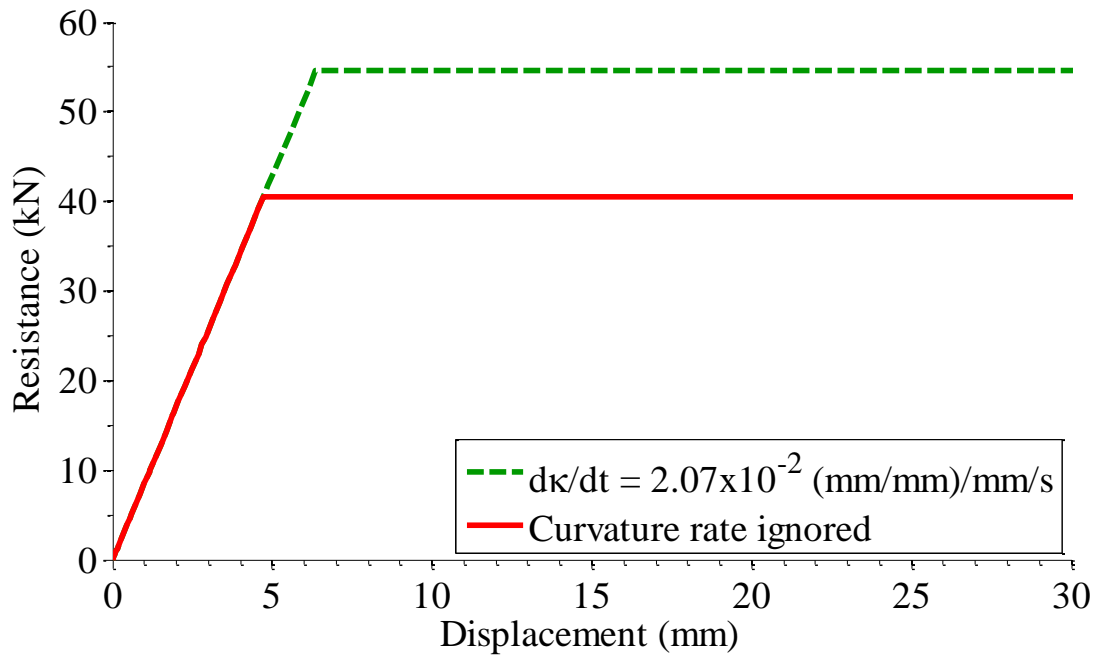
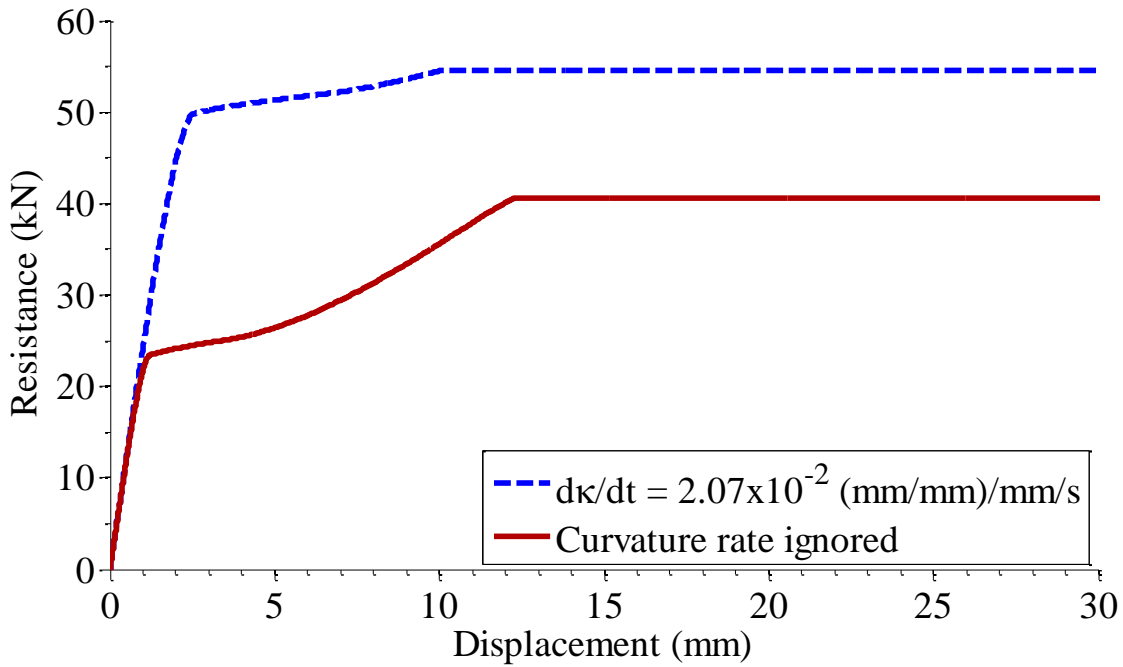


Figure 3.6: Pressure histories experienced by specimen WML12



(a)



(b)

Figure 3.7: Effect of strain rate on bilinear resistance function; (a) bilinear model resistance function; (b) nonlinear model resistance function (specimen WML12)

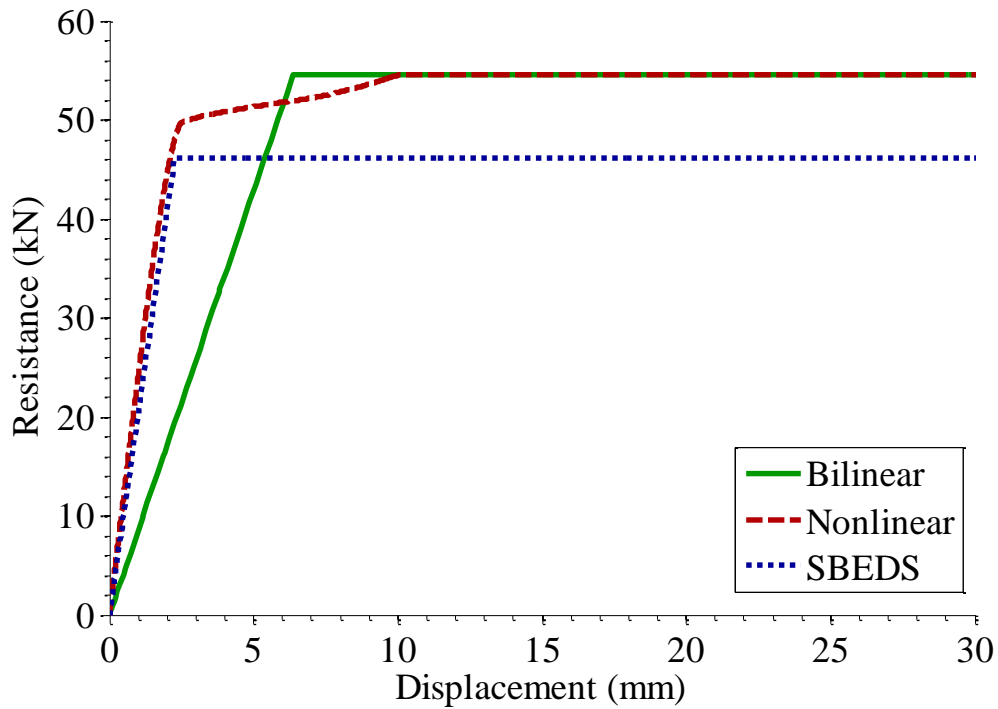


Figure 3.8: Comparison between different strain rate dependent resistance functions describing the behaviour of specimen WML12; bilinear model, nonlinear model, and SBEDS software (DIFs in SBEDS are assumed from USDOD (2008))

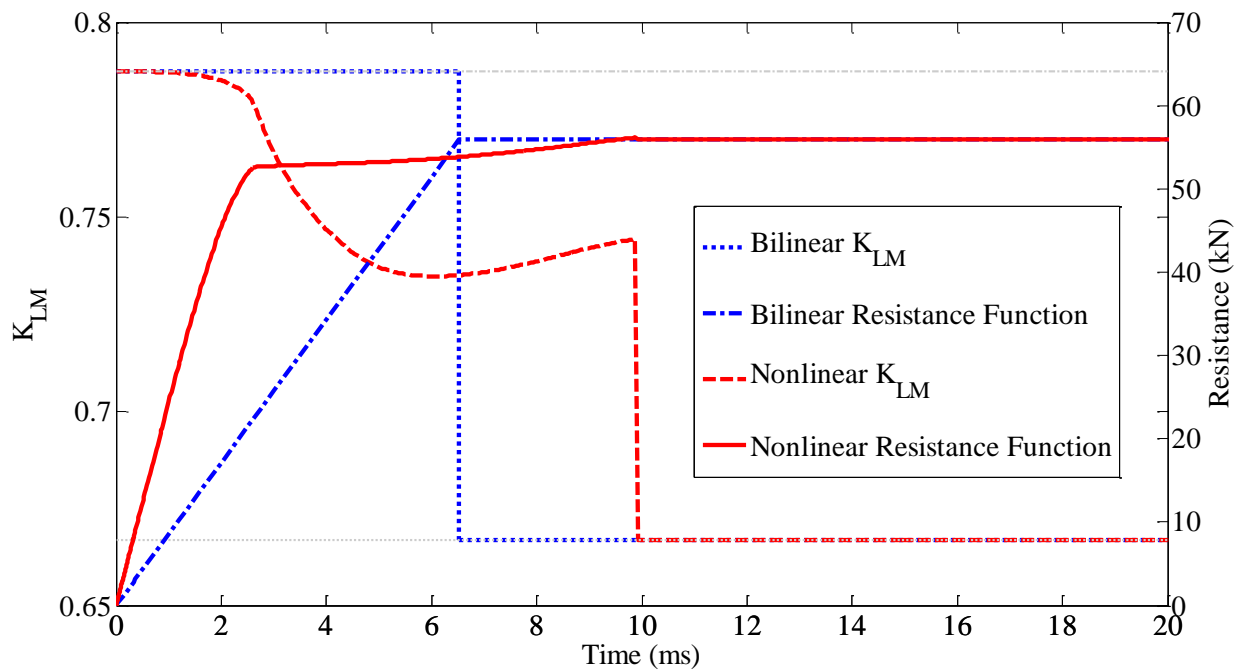


Figure 3.9: Variation of the load-mass factor (specimen WML12)

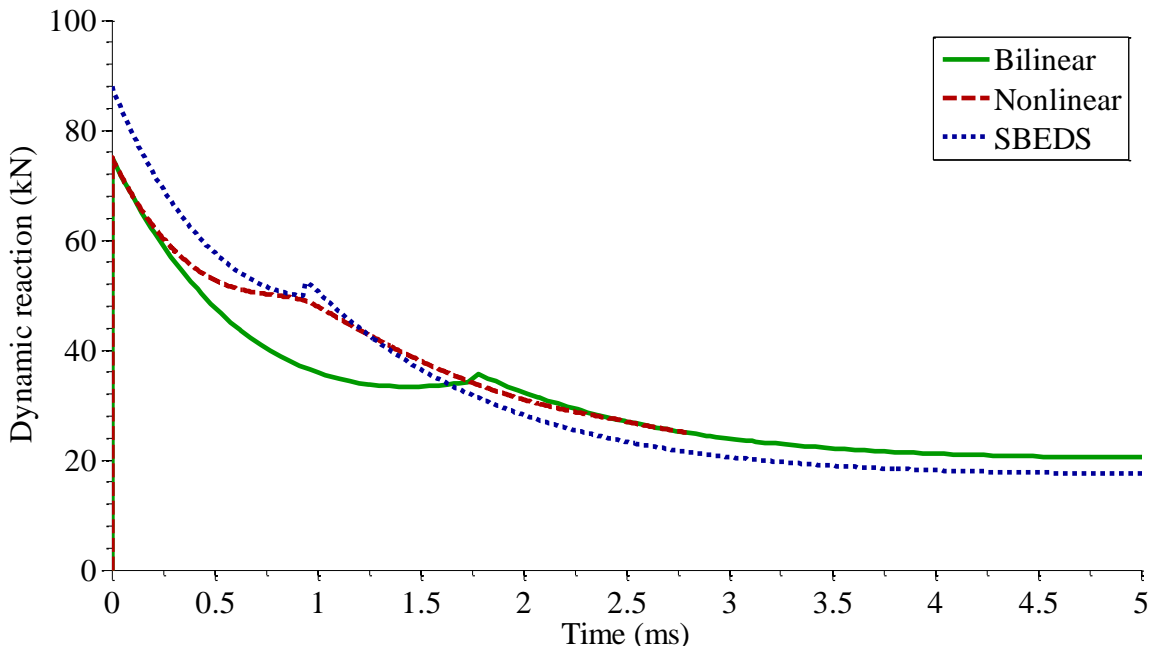


Figure 3.10: Dynamic reaction history calculated for specimen WML12

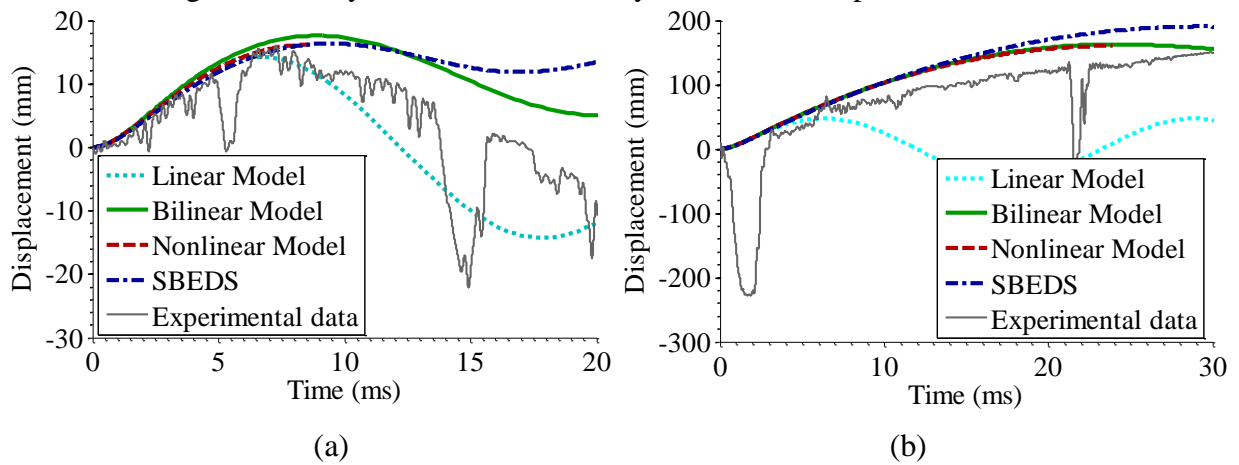


Figure 3.11: Comparison of displacement histories obtained from test data and four different dynamic models; (a) specimen WML6; (b) specimen WML30

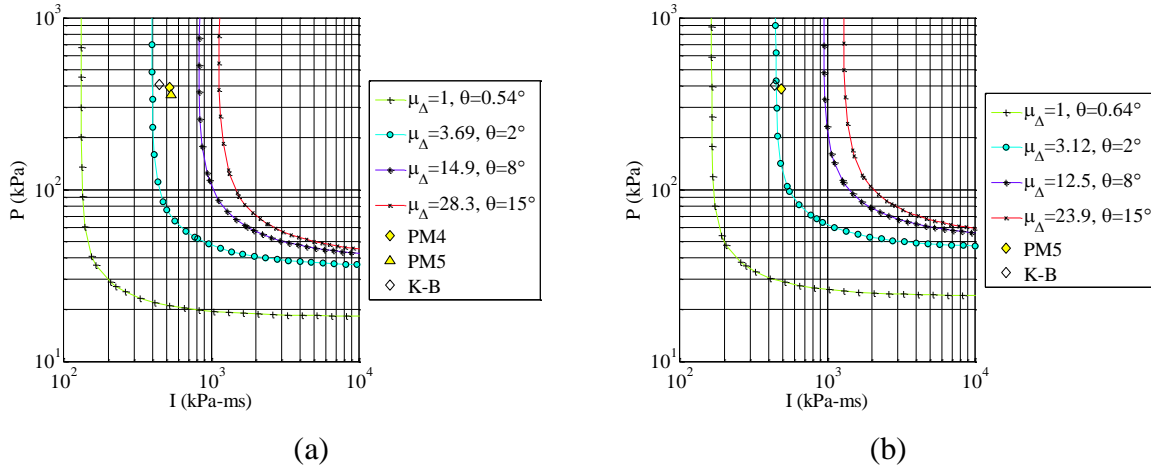


Figure 3.12: Pressure-impulse diagrams derived from bilinear model without strain rate effects; (a) specimen WML6; (b) specimen WMH6

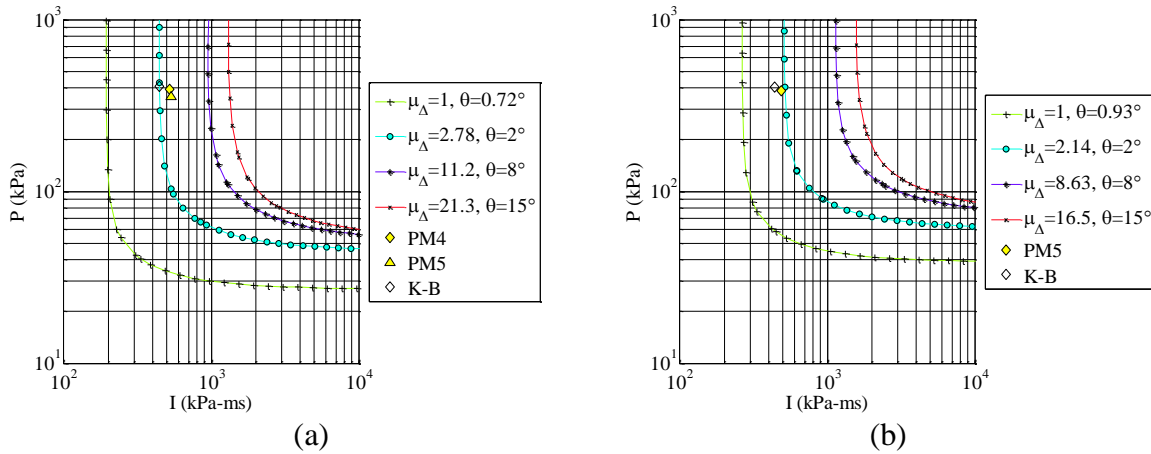


Figure 3.13: Pressure-impulse diagrams derived from bilinear model including strain rate effects; (a) specimen WML6; (b) specimen WMH6

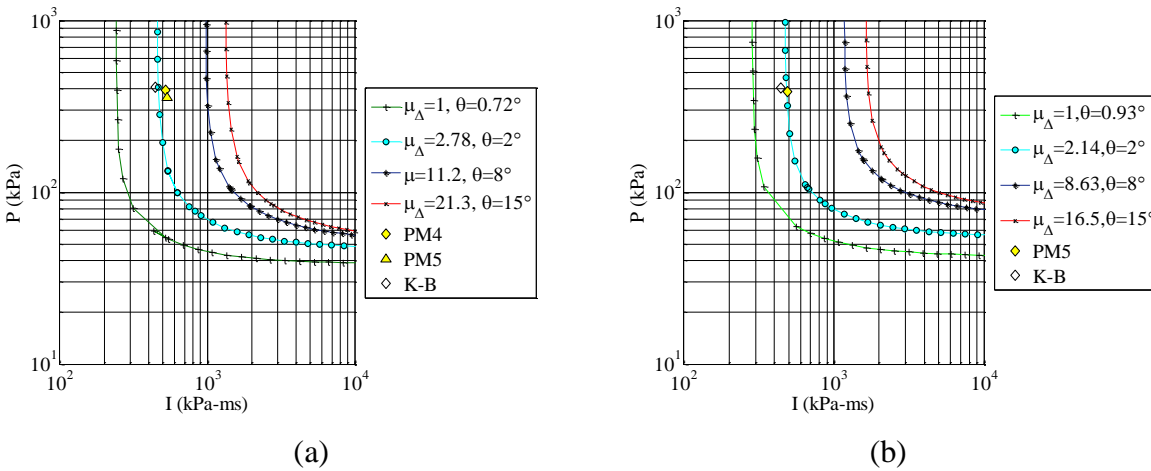
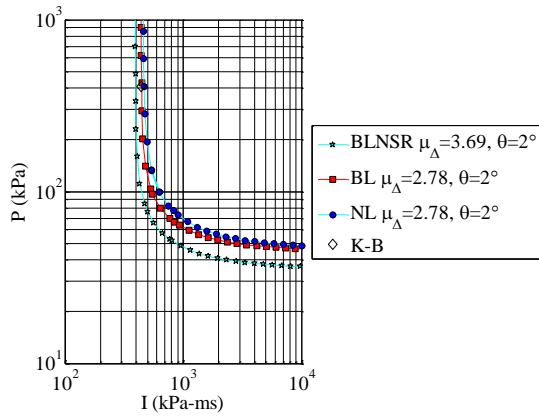
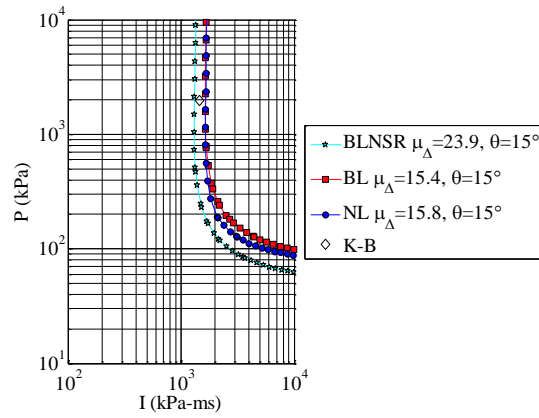


Figure 3.14: Pressure-impulse diagrams derived from nonlinear model including strain rate effects; (a) specimen WML6; (b) specimen WMH6



(a)



(b)

Figure 3.15: Iso-damage curves from bilinear neglecting strain rate (BLNSR), bilinear including strain rate (BL), and nonlinear (NL) models; (a) “Heavy” response limit for specimen WML6; (b) “Blowout” response limit for specimen WMH30

Table 3.1: Comparison of static test results with theoretical predictions

Wall Group	Peak Resistance (kN)	
	Experimental	Theoretical
Group I	Test Failure	40.5
Group II	60.9	53.3

Table 3.2: Peak dynamic reaction predicted by different models

Wall Designation	Bilinear Dynamic Reaction (kN)	Nonlinear Dynamic Reaction (kN)	SBEDS Dynamic Reaction (kN)
WML6	39.1	39.3	45.8
WML12	74.9	75.0	87.9
WML30	192.8	192.9	223.9
WMH6	39.1	39.1	45.8
WMH12	74.9	75.0	87.9
WMH30	192.8	192.9	223.9

Table 3.3: Comparison of peak pressure and specific impulse obtained from test data and the K-B model

Wall Designation	Experimental Results		K-B Model Values		Error (%)	
	<i>P</i> (kPa)	<i>I</i> (kPa-ms)	<i>P</i> (kPa)	<i>I</i> (kPa-ms)	<i>P</i>	<i>I</i>
WML6	498.2	465.7	417.8	450.8	-19.2%	3.3%
WML12	918.5	868.6	801.7	748.1	-14.6%	-16.1%
WML30	2549.1	1274.3	2063.1	1480.5	-23.6%	13.9%
WMH6	479.8	465.7	417.8	450.8	-14.8%	-3.3%
WMH12	1062.6	575.5	801.7	748.1	-32.5%	23.1%
WMH30	2554.9	1082.6	2063.1	1480.5	-23.8%	26.9%
				Average	-21.4%	7.9%
				Std. Dev.	6.8%	16.4%

Table 3.4: Comparison of experimental and theoretical peak displacements

Wall Designation	Experimental $\Delta$ (mm)	Theoretical $\Delta$ (mm)					Error (%)				
		Linear	Bilinear	Nonlinear	SBEDS	Biggs (1964)	Linear	Bilinear	Nonlinear	SBEDS	Biggs (1964)
WML6	15.6	14.3	17.6	16.2	16.4	17.5	-9.1%	11.4%	3.7%	4.9%	10.8%
WML12	37.0	23.8	43.1	41.0	44.3	52.4	-55.5%	14.2%	9.8%	16.5%	29.4%
WML30	Not Recorded	47.3	162.7	160.2	190.4	106.7	N/A	N/A	N/A	N/A	N/A
WMH6	15.6	13.5	14.2	15.5	11.4	9.7	-15.6%	-9.8%	-0.6%	-36.8%	-61.1%
WMH12	18.1	22.5	30.9	32.3	29.4	18.9	19.6%	41.4%	43.9%	38.4%	4.3%
WMH30	50.8	44.8	109.8	108.9	124.6	54.9	13.4%	53.7%	53.4%	59.2%	7.5%

Table 3.5: Summary of Damage States and Level of Protection provided across selected models

Wall Designation	Experimental		Bilinear (neglected strain rate effects)		Bilinear (strain rate effects included)		Nonlinear	
	Damage State	LOP	Damage State	LOP	Damage State	LOP	Damage State	LOP
WML6	Moderate	Medium	Heavy	Low	Heavy	Low	Moderate	Medium
WML12	Heavy	Very Low	Heavy	Low	Heavy	Low	Heavy	Low
WML30	Blowout	None	Blowout	None	Blowout	None	Blowout	None
WMH6	Superficial	High	Heavy	Low	Moderate	Medium	Moderate	Medium
WMH12	Moderate	Medium	Heavy	Low	Heavy	Low	Heavy	Low
WMH30	Heavy	Very Low	Hazardous	Very Low	Hazardous	Very Low	Hazardous	Very Low

## CHAPTER 4 - SUMMARY, CONCLUSIONS AND FUTURE WORK

### 4.1 SUMMARY

Six third scale flexural masonry panels were subjected to design basis threats (DBT) of different magnitudes resulting from the surface detonation of a number of explosive charges of different mass. The wall deflection was measured by using DPs to determine the structural response at key nodes along the height of each flexural panel. The wavefront parameters extracted from the pressure data were compared to the values obtained from the K-B model. To account for strain rate effects on the specimen response caused by high speed dynamic loading, a curvature rate is calculated based on the blast parameters and incorporated into the strengths of the materials to determine the response of the specimens.

The predictions obtained from single degree of freedom (SDOF) modeling were validated against the experimental results. As no failure modes other than that associated with flexural behaviour were observed in the test specimens, SDOF modeling was deemed sufficiently accurate and no other numerical techniques were attempted such as multi-degree of freedom system (MDOF) or finite element modeling (FEM).

The adopted models included bilinear and nonlinear resistance functions, the former obtained by conventional means, well documented in the literature (e.g. USDOD 2008), while the latter obtained from a fiber model used to discretized the wall cross-section in a number of layers. Strains and stresses were evaluated at each fiber and the wall resistance function was subsequently determined by numerical integration of the stress distribution.

After corroborating the SDOF model results with test data, *P-I* diagrams were developed to help quantify the damage that similar wall may experience under a wide range of blast scenarios.

## 4.2 CONCLUSIONS

Based on the research project presented herein, the following conclusions can be drawn:

1. The K–B model is capable of predicting with reasonable accuracy the fitted peak blast pressures and the positive specific impulse with errors of -3% and 1% for the peak pressure and specific impulse, respectively, which corresponds to coefficients of variation of 7.4% and 9.0%.
2. Increasing the reinforcement ratio is found to be beneficial with regard to augmenting the level of protection provided by walls.
3. The observed post-blast damage of the walls in this study increases as the DBT increases, decreasing the level of protection provided as higher damage limits are achieved. By increasing the reinforcement ratio, the observed post-blast damage at each of the DBT decreases.
4. The SDOF model developed by Biggs (1964) provides a preliminary estimate for the mid-span deflection of the flexural walls. This approach shows a somewhat poor accuracy in predicting the mid-span deflection of walls experiencing superficial damage – characterized by a maximum bending moment exceeding by a small margin the moment at first cracking – as well as severe damage (hazardous).
5. The qualitative analysis of the post-blast damage aligns with the quantitative analysis of the support chord rotations at all DBT ( $Z=2.75 \text{ m/kg}^{1/3}$ ,  $Z=2.18 \text{ m/kg}^{1/3}$ ,  $Z=1.61 \text{ m/kg}^{1/3}$ ) used in this study.
6. The design software SBEDS may underestimate for the wall flexural response, thus caution is advised when using the program and more accurate calculations are recommended for finalizing the reinforcement detailing.

7. The linear, bilinear, and nonlinear models, as well as SBEDS, all manifest shortcomings of sorts in predicting the structural response of flexural walls. The linear model provides the closest predictions for the wall group which displays the highest theoretical moment resistance (Group II) while providing inferior predictions for the wall group which shows the highest theoretical ductility (Group I). In comparison, the bilinear and nonlinear models provide good predictions for the Group I walls, while showing an overestimation of the peak deflections of the Group II walls. Similar to the bilinear and nonlinear models, SBEDS provides reasonable predictions for the Group I walls, but poor predictions for the Group II walls.
8. The equation from Biggs (1964) for calculating the peak displacement of a SDOF model subjected to impulsive loading shows reasonable accuracy. However, it greatly underestimates the mid-span deflections of low DBT used in this study.
9. The nonlinear behaviour of the test flexural panels can have a very significant impact on their structural response. By neglecting the strain rate effects or the reduction in stiffness caused by cracking of the concrete, an overly conservative estimate of the mid-span deflection is typically obtained.
10. In most cases, the  $P-I$  diagrams developed by the bilinear and nonlinear models in this study correctly predict the post-blast damage states observed in the test specimens when accounting for the effect of strain rate.
11. The development of Pressure-Impulse ( $P-I$ ) diagrams provide a simple quantification of the level of protection (LOP) of flexural walls based on predefined response limits. Given the combinations of pressure and impulse measured and predicted for each blast scenario, all

test walls met the design requirements specified by modern standards (ASCE, 2011 and CSA, 2012), with the exception of wall WML30.

12. Strain rate effects significantly alter the impulsive and pressure asymptotes associated with each *P-I* diagram. Furthermore a strain rate induced increase in the rotations before the onset of plastic deformation is noted, ranging from 30% to 40%.
13. *P-I* diagrams based on bilinear and nonlinear models show very limited discrepancies, which do not seem to warrant the greater computation effort required by the nonlinear model.

#### **4.3 RECOMMENDATIONS FOR FUTURE WORK**

The research presented herein includes the results from experimental tests of flexural masonry panels subjected to blast loading resulting from the detonation of several explosive charge weights. These test results can be used by designers, researchers, and consultants to aid the analysis and design flexural walls with greater resistance to blast loading. It is also acknowledged that much remains to be done in order to develop a full understanding of the phenomena involved in the response of masonry structures to blast. Future work may address the following issues:

1. The current tests focused on third-scale, one-way, simply-supported, reinforced masonry flexural panels. Future research should focus on different boundary conditions and different wall configurations. Additionally, a range of scaled distances should be adopted, varying either the stand-off distance or charge weight in order to investigate the effect of different loading conditions.
2. The current experimental program did not include the measurement of the rate of strain, neither in the concrete blocks nor in the reinforcing bars. Future research should attempt to

obtain reliable measurements of this sort, to improve the models currently used for determining the strength of materials under high strain rates.

3. The adopted test setup resulted in near-impulsive-driven structural response, i.e. a load duration much shorter than the specimens natural period of vibration. Future research should focus on other response regimes as well, including dynamic and quasi-static (peak pressure controlled) regimes.
4. Axial load should be included as an independent variable in future studies, in order to investigate the dynamic response of load bearing masonry walls subjected to both axial and out-of-plane blast loading.
5. The effect of blast loading on masonry walls with brick veneer should be investigated. Studies should cover different boundary conditions and wall configurations.

## CHAPTER 5 - REFERENCES

- Abedini, M., Mutalib, A.A., Baharom, S., Hao, H. (2013). “Reliability Analysis of P-I Diagram Formula for RC Column Subjected to Blast Load,” *International Journal of Civil Science and Engineering*, Vol. 7, No. 8, 2013.
- Abou Zeid B. (2010). “Experimental and Analytical Strategies to Assess and Improve the Dynamic Response of Unreinforced Concrete Masonry Walls under Blast Loading”, McMaster University, Ontario.
- Abou-Zeid, B.M., El-Dakhkhni, W., Razaqpur, A.G., and Foo, S. (2011). “Response of Arching Unreinforced Concrete Masonry Walls to Blast Loading.” *J. Str. Eng.*, 137(10), 1205-1214.
- ASCE (2011). ASCE-59-11: Blast Protection of Buildings. American Society of Civil Engineers (ASCE), Reston, VA, USA.
- ATBLAST. (2007). A computer software by Protective Glazing Council. Applied Research Associates (ARA), Inc., USA.
- Baker, WE (1973). *Explosions in Air*. University of Texas Press, Austin, Texas, USA.
- Baker WE, Cox PA, Westine PS, Kulesz JJ and Strehlow RA (1983). *Explosion Hazards and Evaluation*. Elsevier Scientific Publishing Company Inc., New York, NY.
- Baylot, J., Bullock, B., Slawson, T., Woodson, S. (2005). Blast Response of Lightly Attached Concrete Masonry Unit Walls. *J. Struct. Eng.*, 131(8), 1186-1193.
- Biggs JM (1964). *Introduction to Structural Dynamics*. McGraw-Hill, New York, NY, USA.
- Bentz EC and Collins MP, 2000. RESPONSE-2000 Reinforced Concrete Sectional Analysis. University of Toronto.
- Bertero, V.V., Rea, D., Mahin, S., and Atalay, M.B. 1973. Rate of loading effects on uncracked and repaired reinforced concrete members. In *Proceedings of the 5th World Conference on Earthquake Engineering*, Rome, 25-29 June 1973. Earthquake Engineering Research Laboratory, Pasadena, CA, Vol. II, pp. 1461–1470. Available from [http://www.iitk.ac.in/nicee/wcee/fifth\\_conf\\_Rome](http://www.iitk.ac.in/nicee/wcee/fifth_conf_Rome). [accessed 17 April 2014].
- Browning, R.S., Hoemann, J.M., Davidson, J.S. (2011). Large-Deflection Response of Fully Grouted Reinforced Masonry Walls to Static and Dynamic Out-of-Plane Pressure. American Concrete Institute.
- Campidelli M, Razaqpur AG and Foo S (2013). Reliability-Based Load Factors for Blast Design. *Canadian Journal of Civil Engineering*, 40(5): 461–474. Permalink: <http://dx.doi.org/10.1139/cjce-2011-0411>.

- Campidelli M., Razaqpur AJ, Foo S (2013). Assessment of Civilian Structures for Military Applications. Magazine of Concrete Research. Institution of Civil Engineers. Permalink: <http://dx.doi.org/10.1680/macr.13.00122>
- Canadian Standards Association (CSA). (2012). Design and Assessment of Buildings Subjected to Blast Loads. CSA 850-12, Mississauga, Ontario, Canada.
- Canadian Standards Association (CSA). (2004). Design of Masonry Structures. CSA S304.1-04, Mississauga, Ontario, Canada.
- Carney, P. and Myers, J.J. (2005). Out-of-Plane Static and Blast Resistant Capacity of Unreinforced Masonry Wall Connections Strengthened with Fiber Reinforced Polymers. Center for Infrastructure Engineering Studies, University of Missouri-Rolla, Rolla, MO.
- Chopra, A.K. (2012), Dynamics of Structures. Fourth Edition. Prentice Hall Inc., New Jersey, USA.
- Collins MP and Mitchell D. 2001. Prestressed Concrete Structures, Prentice-Hall Inc.
- Comité Euro-International du Béton, 1990. CEB-FIP Model Code 1990, Redwood Books, Trowbridge, Wiltshire, UK.
- Dusenberry DO (2010). Handbook for blast resistant design of buildings. John Wiley & Sons Inc., Hoboken, NJ.
- Henrych, J. (1979). The dynamics of explosion and its use. Elsevier Scientific Publishing Company, New York, USA.
- Hrynyk, T. and Myers, J. (2008). Out-of-Plane Behavior of URM Arching Walls with Modern Blast Retrofits: Experimental Results and Analytical Model. J. Struct. Eng., 134(10), 1589–1597.
- Hyde DW (1990). Conventional weapons effect (CONWEP). Application of TM5-855-1. US Army Engineer Waterways Experiment Station, Vicksburg, USA.
- Jacques, E. (2011). Blast Retrofit of Reinforced Concrete Walls and Slabs.” University of Ottawa, Canada.
- Jones, N. (1988). Structural impact. Cambridge University Press, Cambridge; New York.
- Kingery CN and Bulmash G (1984). Airblast Parameters from TNT Spherical Air Burst and Hemispherical Surface Burst. Report ARBRL-TR-02555. US Army Research and Development Center – Ballistic Research Laboratory (BRL), Aberdeen Proving Ground, Aberdeen, MD.
- Kinney, G. F. and Graham, K. J. (1985), “Explosive shocks in air,” Springer-Verlag, New York, USA.

- Kistler (2012). Piezotron® miniature, high sensitivity, voltage output pressure sensors, type 211B. Kistler Instrument Corp., Amherst, NY. Available from [http://www.intertechnology.com/Kistler/pdfs/Pressure\\_Model\\_211B.pdf](http://www.intertechnology.com/Kistler/pdfs/Pressure_Model_211B.pdf) [accessed 21 Mar 2014].
- Malvar LJ. 1998. Review of Static and Dynamic Properties of Steel Reinforcing Bars, *ACI Materials Journal*, V95, 5, pp. 609-616.
- Malvar, L. J., Crawford, J.E. (1998). Dynamic Increase Factors for Steel Reinforcing Bars. Twenty-Eighth DDESB Seminar, August 1998, Orlando, FL. Port Hueneme, CA:Department of Defence Explosives Safety Seminar.
- Malvar LJ, and Ross CA (1995). Review of Strain Rate Effects for Concrete in Tension, *ACI Materials Journal*, V95, 6, pp. 735-739.
- Malvar, L. J., Crawford, J.E. (1998). Dynamic Increase Factors for Concrete. Twenty-Eighth DDESB Seminar, August 1998, Orlando, FL. Port Hueneme, CA:Department of Defence Explosives Safety Seminar.
- Mays, G.C., and Smith, P.D. (1995). Blast effects on buildings: Design of buildings to optimize resistance to blast loading. Thomas Telford, London.
- Myers, John J, Belarbi, Abdeldjelil, El-Domiaty, and Khaled A. (2004) Blast Resistance of FRP Retrofitted Un-Reinforced Masonry (URM) Walls with and without Arching Action. *TMS J.*, 22(1), 9-26.
- Nalagotla, J. K.R. (2013), Pressure-Impulse Diagrams using Finite Element Analysis for Reinforced Concrete Slabs Subjected to Blast Loading. University of Missouri-Kansas City, United States.
- Ngo TD, Mendis PA, Teo D and Kusuma G (2003). Behavior of high-strength concrete columns subjected to blast loading. In *Advances in Structures: Proceedings of the International Conference ASSCCA 2003*, Sydney, Australia (Hancock GJ, Bradford MA, Wilkinson TJ, Uy B and Rasmussen KJR (eds)). Swets & Zeitlinger BV, Lisse, the Netherlands, vol. 2, pp. 1057–1062. See [http://books.google.ca/books?id!4IpFwi995cZkC&source!4gbs\\_navlinks\\_s](http://books.google.ca/books?id!4IpFwi995cZkC&source!4gbs_navlinks_s) [accessed 03/19/2014]
- Orica (2013). Pentex™ D cast boosters technical data sheet. Orica Hong Kong Ltd, Kowloon, Hong Kong. Available from [http://www.oricaminingservices.com/us/en/product/products\\_and\\_services/initiating\\_systems/pentex\\_d\\_cast\\_boosters/1160](http://www.oricaminingservices.com/us/en/product/products_and_services/initiating_systems/pentex_d_cast_boosters/1160) [accessed 3 Dec 2013].
- PCB (1997). ICP pressure sensor specifications, model No. 113A21. PCB Piezotronics, Inc., Depew, NY. Available from <http://www.thermofisher.com.au> [accessed 18 Dec 2013].
- Razaqpur, A. G., Tolba, A., and Contestabile, E. (2007). "Blast loading response of reinforced concrete panels reinforced with externally bonded GFRP laminates." *Composites Part B: Engineering*, 38(5-6), 535-546.

- Rong, H. and Li, B. (2008). Deformation-Controlled Design of Reinforced Concrete Flexural Members Subjected to Blast Loadings. *J. Struct. Eng.*, 134(10), 1598–1610.
- Ross, C.A., Tedesco, J.W., Kuennen, S.T. (1995). Effects of Strain Rate on Concrete Strength. *ACI Materials Journal*, Vol. 92, No. 1, January-February 1995, pp. 37-47.
- Silva, P. and Lu, B. (2009). Blast Resistance Capacity of Reinforced Concrete Slabs. *J. Struct. Eng.*, 135(6), 708–716.
- Smith, Nicholas L. (2014). Response of Two-Way Reinforced Masonry Infill Walls under Blast Loading. *Open Access Dissertations and Theses*. Paper 8925.
- Smith PD and Hetherington JG (1994). Blast and Ballistic Loading of Structures. Butterworth-Heinemann Ltd, Oxford, UK.
- Shi, Y., Hao H., and Li, Z. X. (2008). Numerical derivation of pressure-impulse diagrams for prediction of RC column damage to blast loads. *International Journal of Impact Engineering* 35(11). 1213-1227.
- Takeda, J. and Tachikawa, H. (1971). Deformation and fracture of concrete subjected to dynamic loading. In *Proceedings of the International Conference on Mechanical Behaviour of Materials*, Kyoto, Japan, 15-20 August 1971. Society of Materials Science, Kyoto, Vol. 4, pp. 267–277.
- Urgessa, G. and Maji, A. (2010). Dynamic Response of Retrofitted Masonry Walls for Blast Loading. *J. Eng. Mech.*, 136(7), 858–864.
- USDOD (2008). Unified Facilities Criteria. Structures to Resist the Effects of Accidental Explosions. Document No. UFC 3-340-02. US Department of Defense (USDOD), Washington, DC. Available from [http://www.wbdg.org/ccb/DOD/UFC/ufc\\_3\\_340\\_02.pdf](http://www.wbdg.org/ccb/DOD/UFC/ufc_3_340_02.pdf) [accessed 14 July 2013].
- USACE (2008). Users Guide for the Single-Degree-of-Freedom Blast Effect Design Spreadsheet (SBEDS). United States Army Corps of Engineers (USACE) Protective Design Center, Omaha, NE. Available from <https://pdc.usace.army.mil/software/sbeds> [accessed 10 March 14]
- Wei, X. and Stewart, M. (2010). Model validation and parametric study on the blast response of unreinforced brick masonry walls. *J. Impact Eng.*, 37(11), 1150-1159.
- Williams, G. and Williamson, E. (2011). Response of Reinforced Concrete Bridge Columns Subjected to Blast Loads. *J. Struct. Eng.* 137, SPECIAL ISSUE: Commemorating 10 Years of Research since 9/11, 903–913.
- Zadeh, R.R. (2011). Pressure-Impulse Diagrams using Finite Element Analysis for Reinforced Concrete Columns Subjected to Blast Loading. University of Missouri-Kansas City, USA.

**Appendix A: P-I DIAGRAMS DEVELOPED USING THE BILINEAR MODEL AND IGNORING STRAIN**

**RATE EFFECTS**

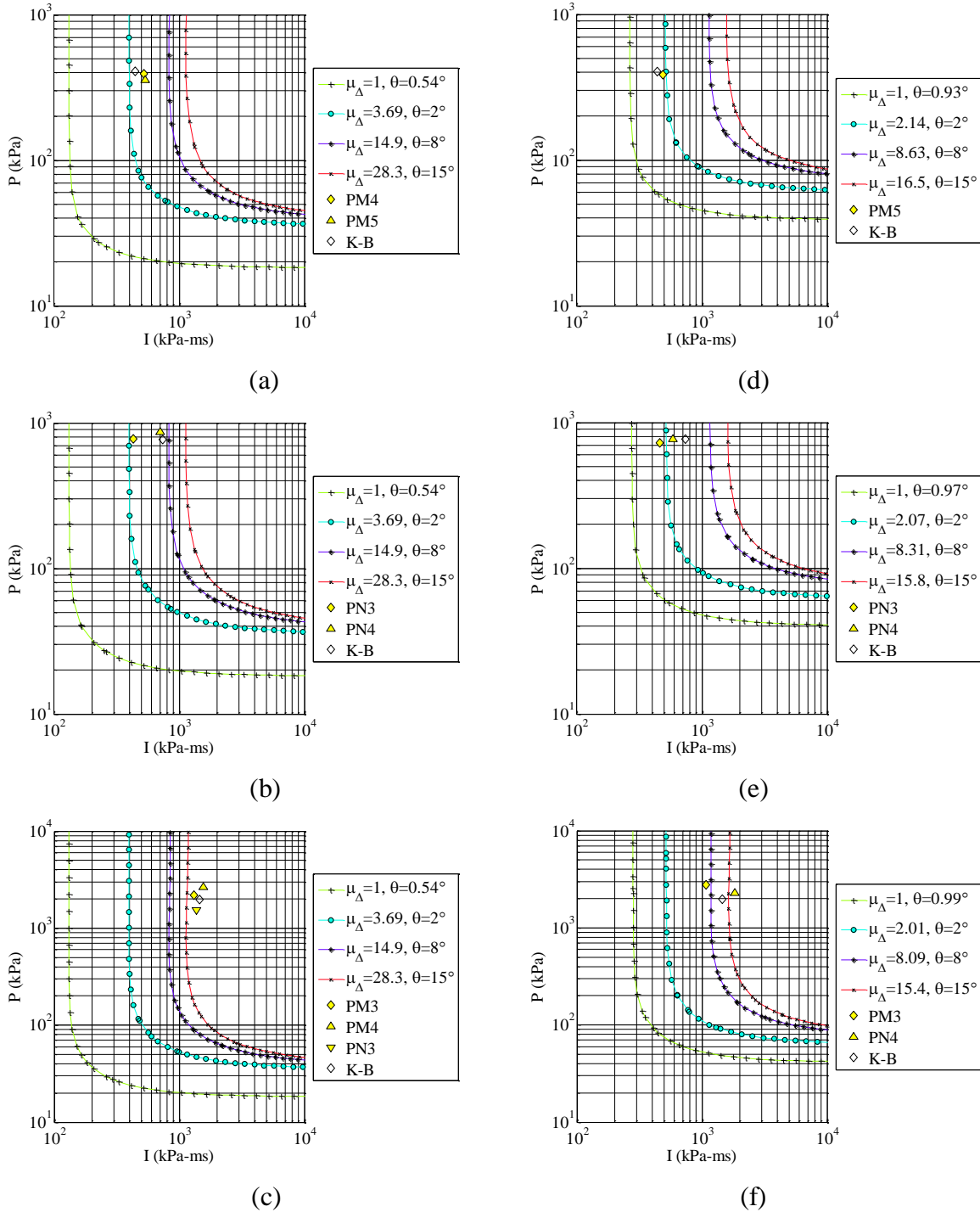


Figure A.1: Pressure-impulse diagrams derived from bilinear model neglecting strain rate effects; (a) specimen WML6; (b) specimen WML12; (c) specimen WML30; (d) specimen WMH6; (e) specimen WMH12; (f) specimen WMH30;

**Appendix B: P-I DIAGRAMS DEVELOPED USING THE BILINEAR MODEL AND ACCOUNTING FOR**

**STRAIN RATE EFFECTS**

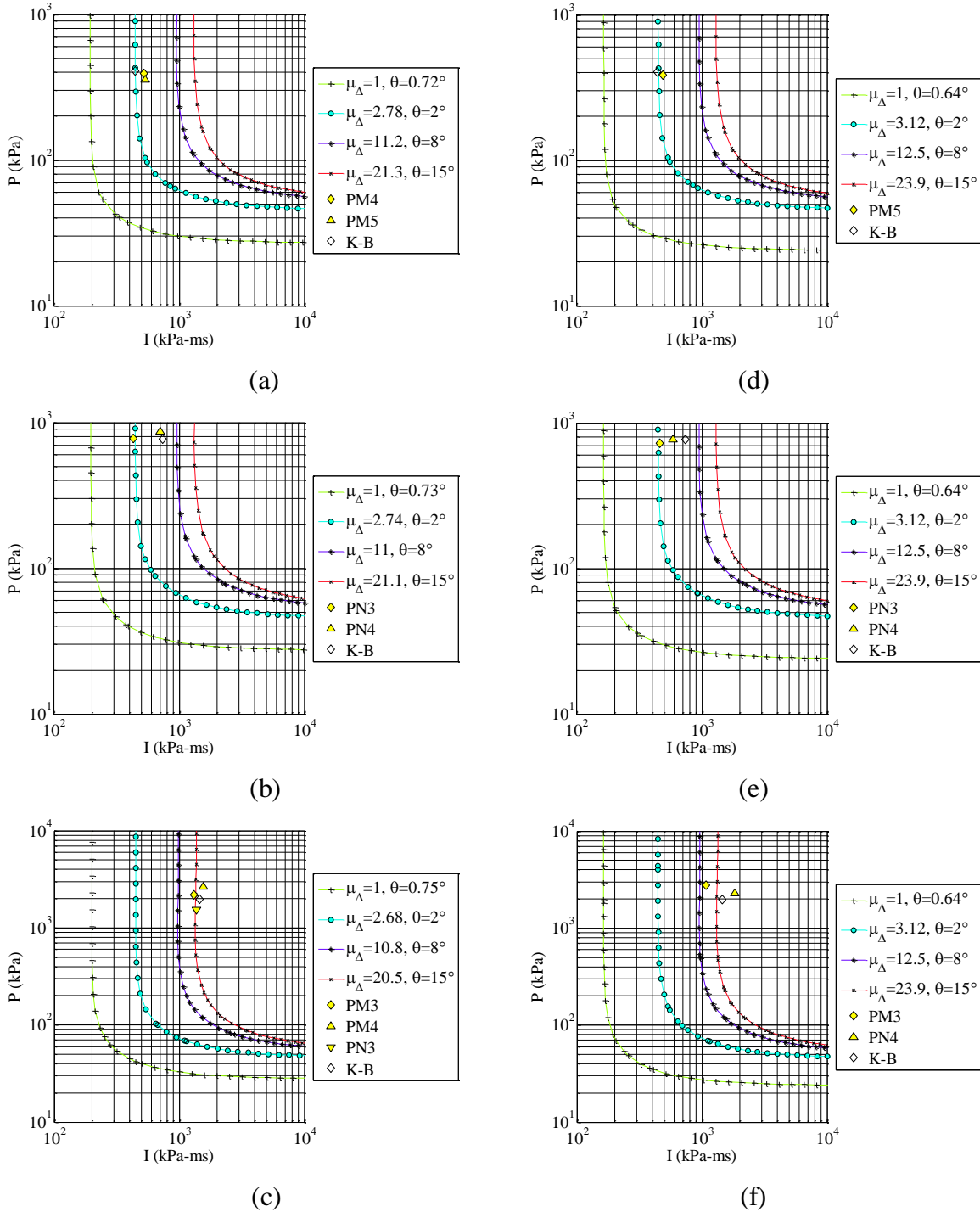


Figure B.1: Pressure-impulse diagrams derived from bilinear model including strain rate effects; (a) specimen WML6; (b) specimen WML12; (c) specimen WML30; (d) specimen WMH6; (e) specimen WMH12; (f) specimen WMH30;

Appendix C: P-I DIAGRAMS DEVELOPED USING THE NONLINEAR MODEL

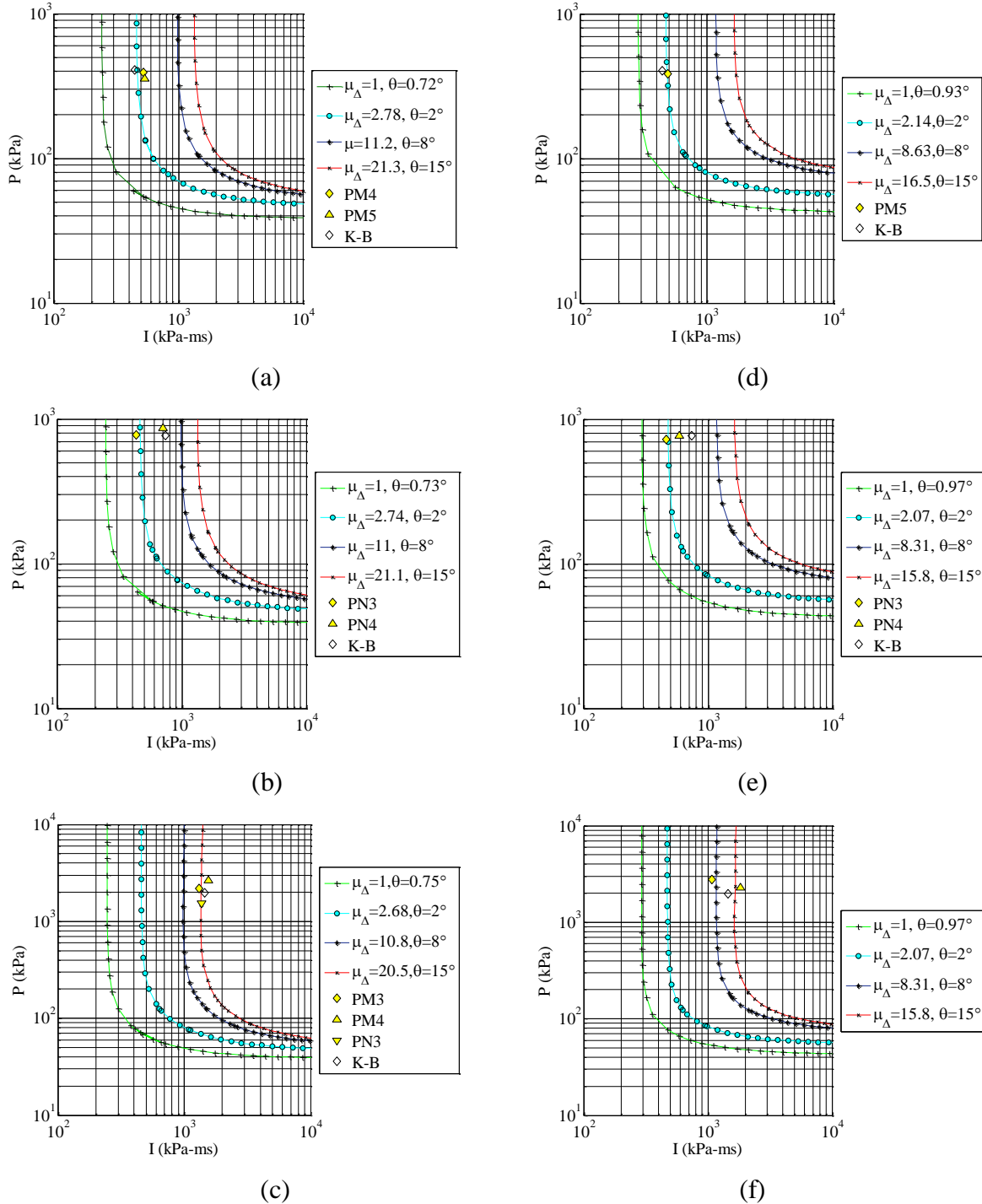


Figure C.1: Pressure-impulse diagrams derived from nonlinear model; (a) specimen WML6; (b) specimen WML12; (c) specimen WML30; (d) specimen WMH6; (e) specimen WMH12; (f) specimen WMH30;